

6. Weld Metal Inclusion Effects

6.1 Inclusion Formation

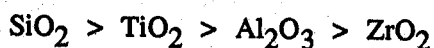
The majority of welding processes involve the melting of the base plate in conjunction with a filler wire and flux, either as a coating on the electrode or as a core of the same e.g. manual metal arc, MMA; alternatively the arc may be contained by a flux layer e.g. submerged arc, SA. The high energy conditions prevailing between the electrode tip and the workpiece generate a plasma state whose temperature can approach 20000K and in which both filler and flux are vapourised and broken down into their constituent elements. The elements are then transferred from electrode to weldpool by three main routes, fig. 6.1:

- (i) As ions through the plasma.
- (ii) As droplets around the periphery of the plasma.
- (iii) As (large) droplets from the tip, which survive the short interval during which they drop through the plasma.

In addition some of the elements are lost to the atmosphere.

Process variables have a strong effect on arc stability, extent and mode of transfer ^(153,198). Therefore, although the flux is made up of oxide powders, these are not generally transferred through the arc as that compound but rather as the constituent elements. Pieces of electrode that do survive unchanged would generally have been very large pieces of electrode coating which detached due to poor binding and cause severe decreases in weld toughness ⁽¹⁹⁹⁾. The molten weldpool ($T \approx 2600^{\circ}\text{C}$) therefore contains these alloying elements (Ti, Al, Si, Mn etc) from the coating and a large oxygen content, as the solubility of O in liquid iron is high (the solubility is 0.22-0.29wt% at the melting point of iron ^(200,201), rising to 0.33 at 1700°C ⁽²⁰²⁾). The oxygen is taken up from the atmosphere or from the shielding gas, which often contains CO_2 to improve arc stability. This advantage must be weighed against increases in oxygen content, immediately below the arc levels of up to 5000ppm are deposited with substantial amounts being removed by recombination with deoxidants during cooling ⁽²⁰³⁾ and loss of elements through vapourisation. The presence of easily reduced oxides, such as SiO_2 , in the flux causes the weldmetal to contain a higher oxygen level, as more is absorbed from the flux ⁽²⁰⁴⁻²⁰⁶⁾. Increased use of constituents such as CaO , Al_2O_3 and CaF_2 reduces the oxygen content in the weld from these more basic fluxes, although oxygen potential and basicity are not necessarily related ^(205,207). These fluxes can readily decrease [O] down to $\approx 200\text{ppm}$, but need the addition of strong deoxidising agents such as aluminium to achieve lower levels. The concept of oxygen potential, with regard to oxygen transfer, was first proposed by Eagar ⁽²⁰⁸⁾, whereby transfer is achieved by formation of volatile sub-oxides. From the thermal decomposition of pure oxides, oxygen partial pressures and hence

oxygen potentials can be found. This gives an oxygen transfer series decreasing in the order



In submerged arc welding, transfer of oxygen can occur through the formation of FeO by decomposition of the oxides in the flux and the amount of FeO transferred to the weld metal increases with decreasing free energy of formation of the flux oxides, so that MnO, SiO₂ and Cr₂O₃ give greater weld oxidation ⁽²⁰⁹⁾. However, in many cases up to 90% FeO can segregate to the slag layer and so not all the oxygen is retained in the weld metal. In acidic fluxes, i.e. high silica content, transfer can also take place via SiO ⁽²¹⁰⁾.

The solubility of O in Fe decreases with decreasing temperature showing a dramatic change upon solidification (at 1345°C the solubility of O in γ-iron is reported to be 0.003-0.007wt%⁽²¹¹⁾, even as low as 0.001wt%⁽²⁰²⁾, decreasing with temperature), whilst at the same time the driving force for alloy oxide formation increases. The net effect is the formation of oxide particles ahead of the solid/liquid interface; those forming at higher temperature tend to be strong oxide formers e.g. Al, Si and Ti, which are thought to nucleate "homogeneously" in the melt ⁽²¹²⁾. This behaviour can be predicted by reference to an Ellingham diagram (fig. 6.2)¹; the strongest oxide formers appear lower on the diagram. These would be expected to form at lower oxygen activities assuming the activity of the metal was similar. Silicates would be expected to form at much lower temperatures than the oxides and Cochrane proposed that these formed during the freezing range of the metal in the enriched interdendritic spaces and may need to nucleate on fragments of the initial high temperature oxides. This would result in particles being aligned in the interdendritic spaces as in fig. 6.3. The resulting inclusion population is determined by the time available for separation and growth of the inclusions, the oxides generally being larger (> 1 μm) than the silicates as the time during which they grow is longer. However, as the oxides form in the melt, density flow and turbulence in the weldpool cause some particles to rise up to be removed into the surface slag layer, others may be swept forward and be remelted. Density flow arises from differences in the density between particles, liquid metal and different compositions of liquid, as these separate flow currents are established, which sweep the particles along with them. Separation is not complete as some particles are trapped by the advancing solid and it is these that form the oxide inclusion population. Stokes' law, i.e. the flotation and separation through buoyancy effects, does not hold for weld metal inclusions, because insufficient time is available and flow effects are stronger ⁽²¹³⁾, for which two regions have been proposed, fig. 6.4. The weld pool consists of a 'hot' region with very turbulent flow from which particles are rapidly removed and a 'cold' region towards the edge of the pool, which is much less turbulent allowing more particles to be trapped by the advancing solid. This goes some way to explaining why the oxygen content of the deposited weld metal is greater than that predicted by equilibrium thermodynamics, applied down to the solidification temperature ⁽²⁰³⁾. In addition to the generally spherical oxides,

¹ The Ellingham diagram being a plot of the standard free energy of formation of an oxide for the consumption of one mole of oxygen versus temperature.

high temperature inclusions can also be faceted high melting point carbides and nitrides, such as TiN. The interaction of the solid/liquid interface with the inclusions brings about segregation of the solid deoxidation products in a similar manner to alloy segregation. The advancing interface can exert a force upon the inclusions, as noted in casting ^(55,56), so that the latter are pushed out in front of the former. Some reports indicate no repulsive interaction ⁽²¹⁴⁾ or indeed an attractive one ⁽²¹⁵⁾, which would reduce the tendency to segregate. Other mechanisms can act, however, such as the Marangoni effect ⁽⁹⁾, which arises from variation of interfacial tension. The latter term is very solute sensitive, hence the solute segregation occurring at solidification boundaries during solid growth causes a gradient in concentration and interfacial tension resulting in convection towards the solidification boundaries. In addition, surface tension may cause inhomogeneous distribution of oxide particles. The largest inclusions will not be moved and so tend to be incorporated straight into the solid, but the smaller ones will be piled up against the interface and drift along the grain boundaries. The forces exerted by any flow processes upon inclusions are proportional to the area of contact, e.g. (radius)² for spherical inclusions, whereas the inertia of the particle is proportional to volume, e.g. (radius)³ for a spherical particle. Therefore the tendency to segregate would be expected to decrease as the volume/surface area ratio increases, for a spherical particle as radius increases. This analysis may be modified by buoyancy effects, although their long range action is not observed⁽⁶¹¹⁾. The later forming silicates tend to form an aligned series corresponding to a line of interdendritic spaces. Experimental verification of this segregation behaviour is difficult as the finally cooled weld will have suffered solid state transformations which destroy the initial solidification structure. By using solute sensitive etches e.g. Klemm I reagent the initial solidification boundaries can be delineated to reveal the correspondence between these and the inclusion population ⁽²¹⁶⁾. Variation of base plate and electrode composition (especially carbon) has been successfully used to vary the solidification mode (as either δ or γ) so that the segregation of inclusions can be better studied ⁽²¹⁶⁾. Again optical metallography reveals large spherical inclusions at solidification boundaries (fig. 6.5) although this may vary with the inclusion type, which is a function of electrode and base composition, heat input and shielding gases. During cooling of the solidified weld, further precipitation, often of sulphides can occur on the already present inclusion population. This has often been observed as a Cu_xS film enveloping oxide particles in low alloy welds, Evans ⁽¹⁰⁰⁾, noted that increases in [S] caused the Ti rich surface layer of inclusions to be replaced by a (Cu,Mn)S type film.

6.2 Variations in Inclusion Distribution and Composition

The very low solubility of oxygen in solid iron means that the oxygen content of a weld is accommodated as an alloy oxide population. Hence, as the oxygen content of a weld increases, so does the inclusion volume fraction. However, attempts to quantify changes in oxygen content with inclusion distributions have been unsuccessful, because the methods of increased deoxidification are through different flux compositions. This will cause a change in the nature of the oxides,

which will form at different temperatures and oxygen activities so that the volume fraction variation can be achieved through a change in the size of the oxide inclusions with different compositions. In addition, sulphur content will also contribute to the inclusion volume fraction through the presence of sulphides. An empirical relationship between inclusion volume fraction and O and S levels was developed by Widgery ⁽²¹⁷⁾:

$$\text{Inclusion content (vol.\%)} = 5.5 (\text{wt\% O} + \text{wt\% S}) \quad \text{.....(49)}$$

Other suggested equations are generally similar, although Saggese et al. ⁽²¹⁸⁾ found 4.2 to be a more applicable coefficient, but incomplete extraction of inclusions may explain this discrepancy. Franklin ⁽²¹⁹⁾ obtained a relationship

$$\text{Inclusion content (vol.\%)} = 5.0 (\text{wt\% O}) + 5.4 (\text{wt\% S} - 0.003\%) \quad \text{.....(50)}$$

which agrees well with Widgery's.

These formulae do not give any indication of the number of inclusions or their size, spacing, shape or dominant composition, all of which may have important effects upon the microstructure and mechanical properties of the weld. It is not possible to ascribe a single composition to an inclusion as they typically consist of more than one phase; instead the dominant phases should be identified. Hence, any study of weld inclusions should sample a statistically significant number of inclusions in order to ensure that the changes noted are representative of the bulk of the weldment. Also the heterogeneous nature may mean that one of the minor phases present is responsible for the effects noted; this makes experimental determination of the precise role of any inclusion phase very difficult. Certain general trends have been established though:

- (i) Inclusion content increases with increases in weld oxygen and sulphur levels.
- (ii) At low oxygen levels the inclusions are composed mainly of oxides of the strong oxide formers, notably Al, but as [O] increases these elements can be exhausted leading to the presence of oxides of Si and Ti. This is in line with Ellingham diagram based thermodynamic predictions. The subsequent formed oxides may deposit on preexisting Al_2O_3 particles to give rise to multiphase inclusions.
- (iii) Segregation of inclusions to solidification boundaries means that their spacing across a prior δ grain will be largely dependent on the cell width and so will be controlled by factors such as heat input, HAZ grain size and base plate texture. Silicate spacing is determined by interdendritic spacing and so is affected by growth rate and temperature gradient as outlined in chapter 2.

6.3 Effects of Inclusions on Mechanical Properties

The major mechanical properties of concern in welding are toughness in the upper and lower shelf regimes of the Charpy impact energy absorption curve. Both of these are heavily dependent on inclusion content. This may also affect the yield stress, but, because of the fast cooling rate, the weld metal generally has a high enough yield stress and so is underalloyed with respect to the baseplate to keep the yield stresses similar.

6.3.1 Upper Shelf Energy

The high temperature part of a Charpy transition curve is determined by the energy absorbed through the propagation of a crack by a "ductile" mechanism resulting in a dimpled fracture surface. Considerable work has been performed on the mechanism of this fracture process, e.g. see review 220, which is generally accepted to occur in three stages.

(i) Nucleation of internal cavities during plastic flow. This usually occurs on second phase particles such as oxides in Cu ⁽²²²⁾ or titanium carbonitrides in steel ⁽²²²⁻²²⁵⁾. If a range of particle sizes are present then the resulting fracture surface exhibits a distribution of dimple sizes ^(226,227) with larger particles nucleating voids at lower stresses and strains than smaller ones.

(ii) Cavity growth with continued deformation. This is a regime of stable void growth either by plastic flow of the matrix material around the void nucleating inclusion or by a mixture of plastic flow and voiding around smaller second phase particles. Wholly plastic growth of voids leads to the preservation of a spherical/ellipsoidal shape ⁽²²⁸⁾, whereas tear like cracks are more typical if repeated void nucleation takes place ^(221,227).

(iii) Coalescence of cavities to give complete rupture. This final stage - the linkage of voids - has several proposed mechanisms, each of which can be observed under different stress and strain conditions. Cottrell ⁽²²⁹⁾ suggested a mechanism involving necking down or 'slipping off' of the intervoid matrix down to zero cross-sectional area, although secondary void formation in intense intervoid shear bands ^(221,230), crack formation and propagation ⁽²³¹⁾ and catastrophic normal rupture above a critical void size ⁽²²³⁾ can also take place.

The energy absorbed to failure is then determined by the total strain to failure, which is the sum of the strains induced by each of the three stages. It is in the nucleation stage that inclusions have a great effect, in one of two ways:

(i) Due to differences in thermal expansivity between the weldmetal and inclusion, thermal stresses act across the metal/ceramic interface and complement the applied stresses until interface decohesion becomes viable (fig. 6.6). This is determined by an energy balance between strain energy released by decohesion and surface energy created. By considering the energy changes for single and twin polar voiding the variation of stress and inclusion radius can be determined (fig. 6.7) with larger inclusions voiding at lower stresses than smaller ones. Hence, the large size of oxide inclusions and their large expansivity difference with steel give rise to ready voiding. The strain involved in nucleation, and so energy absorbed, is reduced as the number of inclusions increases, as their average size increases and as the interface bonding is reduced. All of these factors are controlled by electrode and shielding gas compositions.

In addition, a sufficiently high local stress state must also be established at the interface to cause decohering ⁽²²³⁾.

(ii) If the steel/inclusion interface is strong, then decohering is difficult so that the brittle inclusion can crack under stress, to leave two parts that move apart giving a void, which then acts in a similar way to the decohered voids above (fig. 6.8).

The generally weak interface for weld metal/oxide inclusions compared to the fracture stress of the particle means that (i) is far more prevalent than (ii), which would be expected at higher stresses. However, few studies have been instigated into the strength of weld inclusion/metal interfaces, although work on metal/ceramic bonding may reveal some typical values. For instance, the bond strength in uniaxial tension for stainless steel/ Al_2O_3 bonded with an Al interlayer is 41.5MPa ⁽²³³⁾ compared with weld metal yield stresses of \approx 400MPa or greater.

Once nucleated, the void remains under stress and extends around the inclusion and then extends, changing its shape, to an ellipsoid centred on the inclusion (fig. 6.9). This change can be modelled by multiple dislocation motion ⁽²²⁴⁻²²⁶⁾ under the action of the triaxial stress state around the void with varying degrees of complexity and success. The ellipsoid has maximum stress states at the sharp radius ends and once the length (tip to tip) of the void reaches the mean inclusion separation then 45° shear bands can be established which allow internal necking by slip of intervoid material, fig. 6.10. Growth of the void is defined up to the point of slip along 45° planes and will absorb energy related to strain $\epsilon(\alpha \text{ spacing})$. The final energy absorbed and strain (ϵ_c) is due to coalescence of the voids through their lateral growth.

Therefore any increase in the size or reduction in spacing of inclusions - often achieved by increase in [O] and hence inclusion content - will reduce the upper shelf toughness. This suggests that high toughness welds require a minimum of oxide (or other) inclusions, especially large ones.

6.3.2 Lower Shelf Energy

As temperature decreases, thermal activation is reduced so that dislocation motion becomes more difficult (σ_y increases). Thus, instead of a crack being blunted by plastic flow at the tip, this remains sharp so that the stress intensity is high. It will eventually become energetically favourable to extend a crack by a cleavage burst rather than by void nucleation and growth. As the cleavage crack extends then a situation is reached when the crack becomes self-propagating resulting in catastrophic fast fracture of the component. This is the case where:

$$\text{Strain energy released} = \text{Surface energy required} + \text{any plastic flow (slight)}$$

The structure is 'safe' until a defect reaches the critical size a^* .

The role of inclusions in this mechanism is again in the nucleation stage where they have been identified as initiating defects in cleavage facets ^(107,237). Again, a greater fraction of large inclusions initiate cleavage cracks more readily so that less energy is absorbed in extending it to a^* when it becomes self-propagating. In addition, there is an interaction with microstructure, in that an inclusion in allotriomorphic α or Widmanstätten α is far more deleterious than one in α_{acic} . This is due to the much larger grain size in the former phases which allow a cleavage crack to develop to a much greater length before being arrested by a grain boundary (fig. 2.33). By contrast, the interlocking network of α_{acic} plates have a high density of non-parallel grain boundaries which arrest or divert a developing crack. The energy required to restart the crack or in extending its pathlength then ensures a higher toughness in the low temperature regime. Therefore a decrease in inclusion population should lead to an increase in lower shelf energy

absorption especially if the remaining inclusion content is contained within α_{acic} rather than allotriomorphic α or Widmanstätten α . However, an α_{acic} microstructure is necessary to provide maximum toughness and requires inclusions for nucleation intragranularly, hence a certain inclusion population is a necessary evil.

6.4 Effects of Inclusions upon Phase Transformations

6.4.1 Solidification

Although oxides are formed in the melt ahead of the solid/liquid interface, little evidence exists of solidification occurring upon deoxidation products. Inclusions can affect solidification by acting as heterogeneous nucleation sites for the solid phase, as in casting inoculants. However, in welding, inclusions would be in competition with the melted back HAZ where epitaxy between baseplate and solidified weld leads to growth without nucleation and a very small activation barrier for growth initiation. Under the solidification conditions prevalent during welding, this process is preferable to inclusion nucleation. Further into the weldpool, temperature rises so that the oxides do not form or, if swept in, tend to remelt as the solubility of oxygen in iron again rises. In welds exhibiting a transition in solidification structure from columnar to equiaxed (chapter 2) then no details are available of any increased nucleation on deoxidation products or whether there is a change in their proportions due to:

(i) Increased segregation increasing the driving force for their exsolution ahead of the solid/liquid interface.

(ii) Reduced time for growth due to the very high cooling rates employed.

Due to subsequent solid state transformations and rapid growth rate it is difficult to ascribe an initial very large δ or γ grain to any of the inclusions it may contain, as these could have been trapped by the advancing interface. It is also unclear to what extent the inclusions hinder the motion of this interface although the driving force is so high that the effect would be small, the inclusions being swept towards solidification boundaries or trapped in the solid.

6.4.2 Delta to Austenite Transformation

If a weld solidifies initially as delta ferrite (δ), as most low carbon steel weld deposits do, then on continued cooling it will transform to austenite (γ). This phase will nucleate at prior δ grain boundaries as these are the most favourable sites. This situation was analysed by Barritte⁽⁵⁷⁾, who considered the critical free energy for nucleation of both faceted and unfaceted spherical nuclei on inclusions as a function of inclusion radius (fig. 6.11). This indicated that grain boundaries were found to be energetically more favourable sites for nucleation than inclusions *for the same driving force* irrespective of inclusion radius. Inclusion nucleation is, therefore, only expected after the exhaustion of the available δ grain boundaries. Whether or not the inclusions exert a pinning effect on the δ/γ interface gives conflicting results. As deposited γ grain size has been observed to vary with oxygen content^(238,239) decreasing from 100 μm (100 ppm) to 70 μm (500

ppm) and 150 μ m (250 ppm) to 60 μ m (680ppm). However, Bhadeshia et al. ⁽⁶⁶⁾ noted no variation in γ grain size in submerged arc welds containing 120 and 420 ppm [O], which they explained as being due to the continuous cooling of the specimen. If an inclusion exerts a force upon an advancing δ/γ interface, this will initially be an acceleration as interaction between the particle and the interface increases the line of contact and reduces the total area of particle and δ/γ interface in the system, fig. 6.12. The reduction of total 'surface' area leads to a reduction in surface energies and hence provides the attractive force. A metastable equilibrium is eventually reached, where this reduction of 'surface' area is maximised, the exact position being determined also by strain energy and anisotropy in the adjacent phases; if these are neglected the equilibrium position is across the centre of the particle, fig. 6.12b. Subsequent movement of the interface experiences a retarding force. Bhadeshia's results were obtained from C-Mn-Si SAW deposits, whereas the others were carried out upon HSLA baseplate, which contained significant quantities of Nb, Ti and V. Dilution of these elements into the weld may give precipitation and grain boundary pinning during continuous cooling, as in thermomechanical processing of microalloying steels. This problem has been analysed by Zener and Smith ⁽²⁴⁰⁾ and, by considering surface tensions at the interface, the drag is found to be:

$$f = 2 \pi r \sigma \sin\theta \cos\theta \quad \text{.....(51)}$$

f =drag force

σ =interface energy (=surface tension)

r =particle radius

θ =contact angle of interface with particle which is maximised at $\theta=45^\circ$ so that:

$$f_{\max} = \pi r \sigma \quad \text{.....(52)}$$

This was devised for precipitate systems and is modified by the r^3 variation with volume, so that, for a given volume fraction, a finer dispersion of particles gives greater pinning. As temperature rises, then coarsening and dissolution of particles occurs and the particles become less efficient pinning sites. The latter point does not occur with weld inclusions as they generally undergo few changes in the solid range of the steel, but the range of sizes will give a range of drag effects. More importantly, the pinning occurs during continuous cooling and involves an interface between two phases rather than a grain boundary, so that, as temperature decreases, the driving force for boundary motion increases continuously and should eventually overcome the inclusion drag. Refinement of austenite grain size would only occur if separate nucleation events occurred during the period in which the interface was arrested, which, considering the heat flow and temperature conditions prevailing, is unlikely.

Use of Zener's limiting size eqn:

$$D_1 = \text{Limiting Grain Size} = 2 d_{cr} / 3 f_v \quad \dots(53)$$

d_{cr} =critical inclusion size above which grain growth not restrained

f_v =inclusion volume fraction

by Liu & Olson ⁽²⁴¹⁾ gave values of D_1 of 0.27-0.51 μm , values which did not correspond with the oxygen content or inclusion volume fraction. Instead small γ grain size was found in welds with a high number of small particles which were concentrated at the boundaries (Table VI.1). Further analysis of their results reveals that widely varying inclusion contents gave the same γ grain size, consistent with the results of Bhadeshia et al. Thus the prediction of γ grain size is fraught with difficulties and no reliable theory exists at present.

6.4.3 The Decomposition of Austenite

The 'oxygen effect' has stimulated a lot of work since it was first observed by Ito & Nakanishi ⁽⁶³⁾, who noted that weld metal toughness peaked at around 300ppm oxygen, but decreased at both higher and lower oxygen contents. This was associated with a variation in the solidified weld metal microstructure and prompted the Welding Institute ⁽²⁴²⁾ to propose three oxygen regimes.

(i) Low oxygen ($\leq 200\text{ppm}$): microstructure consists of lath-like structures described as Widmanstätten α or upper bainite.

(ii) Medium oxygen ($\approx 300\text{ppm}$): the toughness maximum generally corresponds to the interlocking network of fine ferrite plates - acicular ferrite.

(iii) High oxygen ($\geq 600\text{ppm}$): the microstructure is dominated by higher temperature products such as allotriomorphic ferrite and Widmanstätten α side plates. Some intragranular high aspect ratio plates are also present.

These regimes were discussed using schematic CCT curves (fig 6.13), which suggest that increased oxygen content causes a decrease in hardenability and also has varying effects on the displacive products (Widmanstätten α and α_{acic}). These regimes are only general and can vary with welding process and alloy content as variations in oxygen content are not independent of variations in grain size or alloy content. This was revealed by Stout et al. ⁽²⁴³⁾, who reported a continual increase in toughness with decreasing oxygen content. This work was carried out on a 3wt% Ni steel weld and the inherent toughening behaviour of the Ni ensured that the upper shelf energy was sampled throughout. The effect of reducing [O] was therefore only to remove void nucleation sites and increase the mean inclusion spacing so that the mean strain to failure and hence energy absorbed increased.

The role of oxygen has centred upon two main problems:

(i) Does oxygen per se cause a decrease in hardenability, which would require its incorporation into a predictive program for weld metal CCT curves and microstructure?

(ii) What are the dominant mechanisms in the nucleation of acicular ferrite?

Concentrating initially on the effect of oxygen upon hardenability, Ito & Nakanishi ⁽⁶³⁾ stated that the γ - α transformation start temperature ($T_s^{\gamma-\alpha}$) appeared to increase at higher oxygen

levels, allowing more time for the development of allotriomorphic ferrite and hence leading to poorer toughness in Charpy impact testing, i.e. less energy absorbed to failure. This was taken further by Cochrane & Kirkwood ⁽²⁴⁴⁾, who based their theory on dilatometric studies of reheated weld specimens and extended it to account for enhanced sideplate (Widmanstätten α) formation at high [O]. The proposed mechanism is illustrated in fig. 6.14 and is based on the presence of a greater proportion of oxide particles on γ grain boundaries at higher oxygen levels, although this is not always the case as was shown in Table VI.1. The result of this higher inclusion population is to pin the boundaries and cause them to become wavy. Subsequent nucleation of ferrite was proposed to occur preferentially upon these oxide inclusions so raising the transformation start temperature. During growth a Kurdjumov-Sachs (K-S) type orientation relationship is adopted by the ferrite as is a side plate wedge morphology due to instabilities in the γ/α interface. Several criticisms were levelled at this proposal and the underlying dilatometric study.

(i) The central argument of the model is that pinning of the γ grain boundaries occurs by the oxide particles, but these welds, with varying [O], were given a constant re-austenitisation treatment. This would be expected to give a variation of γ grain size, although no grain size measurements were given. Hence, an increase in oxygen level could lead to a decrease in γ grain size and a subsequent decrease in hardenability. In this case, i.e. reheated weld metal, there is a finite constant driving force for grain boundary motion at the re-austenitising temperature and so pinning by oxide particles would occur. Later reports have indicated no variation in transformation start temperature with the same grain size ⁽⁵⁷⁾ or effects that could be accounted for by variation in grain boundary area ⁽²⁴⁵⁾.

(ii) This mechanism suggests that sideplates are the product of a diffusional transformation and are, in fact, allotriomorphic α . This is incorrect, as sideplates are Widmanstätten α and form by a diffusion controlled displacive transformation. The change from grain boundary allotriomorphs to Widmanstätten α sideplates does not result from interface instabilities, but from a change in transformation mechanism, which requires a separate nucleation event.

(iii) Watson ⁽¹¹³⁾ claimed that the effect of oxygen was on alloying levels, notably Mn, and this would explain varying results achieved with different flux types (alumina vs calcium silicate ⁽²⁴⁶⁾). Depletion of Mn around inclusions of the calcium silicate type would enhance nucleation of allotriomorphic ferrite, as claimed by Cochrane & Kirkwood ⁽²⁴⁴⁾. Microanalytical data for inclusions in allotriomorphic α is sparse, although Ricks et al ⁽⁶⁵⁾ found no consistent variation in substitutional alloying element, using STEM/EDS around intragranular inclusions in HSLA welds. Depletion of substitutional elements in the matrix around an inclusion due to its formation is not expected as they form in the melt ahead of the solid/liquid interface, where convection currents would rapidly remove any concentration gradients. Any variations introduced through solid-state changes in the inclusions are likely to be limited and of much lesser extent than segregation introduced through solidification.

As inclusions do not offer preferential sites for nucleation when compared to grain boundaries for the same driving force, then the transformation start temperature would be determined by nucleation on γ grain boundaries and preferential growth along them rather than into the grain. The formation of primary side plates is associated with an increase in hardenability favouring displacive transformations over diffusional transformations; a decrease in hardenability generally results in the decoration of γ grain boundaries by a thicker layer of allotriomorphic ferrite. Alloying elements and carbon partition coupled with decreasing temperature would then cause a change from allotriomorphic ferrite to Widmanstätten α side plates, rather than the weaker effect of interface instabilities, although the exact reasons for and conditions at the changeover still need clarification. The need therefore exists to determine the dominant factors - inclusions, grain size or segregation - affecting the transformation start temperature, in order to give an accurate prediction of the volume fraction of allotriomorphic ferrite.

The conflicting effects of inclusions on cleavage toughness in acting as nucleation sites for α_{acic} and microcracks has focussed attention on determining the mechanism responsible for nucleation of acicular ferrite so that a desirable microstructure can be attained with the minimum total inclusion population. Several mechanisms have been proposed, but so far no systematic study of inclusion phases has been undertaken, instead flux compositions have been related to toughness measurements, or inclusions found in α_{acic} plates have been chemically and structurally analysed. The first approach is complicated by other factors such as yield stress, whereas the heterogeneous nature of inclusions make deductions from the second method unreliable. Several reviews on the role of inclusions have recently been published ^(247,248) and the major effects will be summarised here.

In addition to oxides, carbides and sulphides are also usually present in welds and there is the possibility of nitride formation with elements such as Al, Ti and B from interstitial nitrogen. The effect of sulphur contents has been investigated by Abson, Dolby and Hart ⁽²⁴⁶⁾, who carried out SA welding on base plates of varying S content to produce final weld values of between 70 and 290 ppm. Although, 0.09wt% S can be accommodated in solid solution at the peritectic temperature ⁽²⁰²⁾, solubility of this element decreases rapidly so as to be negligible below 800°C. This means that the majority of the sulphur present will tend to precipitate as sulphide inclusions, which exsolve after the oxides and silicates either at grain boundaries or on those preexisting inclusions. With increasing [S] an increase in inclusion population was seen, but not quantified - the volume fraction of inclusions being estimated from Widgery's empirical formula (equation 49) quoted above. The expected variation in inclusion volume fraction ranged from 0.19 to 0.51, depending on flux. There was no increased nucleation of α_{acic} for increased sulphur content, which contrasted strongly with the effect of oxygen content changes, induced by flux changes or by laser remelting. Contents around 200 - 300 ppm (by weight) gave an α_{acic} structure, which gave way to a lath (bainitic) structure when laser remelting lowered [O] to 110 - 150 ppm, although total inclusion content remained constant due to S uptake. Although no detailed analysis

of inclusion composition or distribution (size, spacing, shape) was undertaken, the effect of oxides on α_{acic} formation is seen to be much greater than that of sulphides. There was no study using ultra clean steels with very low sulphur levels (below 70 ppm) so that it is still possible that a lower minimum level of S is required for α_{acic} nucleation, although increases above that level do not enhance its effect. In fact, increasing S levels (0.007-0.040wt% Evans ⁽¹⁰¹⁾) have been associated with an increase in the occurrence of sulphide films around inclusions and a corresponding reduction in the proportion of α_{acic} ⁽¹⁰¹⁾. The films in Evans' study being identified as MnS type. It may be necessary to form a Cu_xS film around the inclusions for them to act as nucleation sites; films of this type have often been noted ^(249,250), but their role has not been deduced. It has been postulated that the thermal expansivity of these films is such as to reduce tessellated stresses, arising from differences in thermal expansivity between matrix and inclusion, around inclusions and so improve fatigue behaviour ⁽²⁵¹⁾. The tessellated stresses arise from differences in thermal expansivity between the matrix and the particle. A similar mechanism of stress relief may assist nucleation of α_{acic} , although in general the inclusions have a thermal expansivity greater than that of steel and would put the steel surrounding them into compression. The volume increase from γ to α would then relieve this stress and be enhanced; therefore reduction of the stress by sulphide films would be expected to hinder nucleation not assist. Other possibilities are that the reduced contraction of the film or its bonding strength prevent voiding at the interface so that stress transfer can take place to counter the strain energy associated with the formation of α_{acic} . However, the interfacial bond strength for sulphide particles in steel is very weak, so that these particles readily detach, as noted by Evans for sulphide coated inclusions ⁽¹⁰¹⁾. Nucleation on fully sulphidic particles in welds e.g. MnS has not been observed and nucleant particles have been observed with no sulphide film, although the film might not fully envelop the inclusion and its absence in any particular plane may be a sectioning effect. Recently, evidence was presented for the apparent nucleation of bainite on FeS precipitates at prior γ boundaries ⁽²⁵²⁾. In this study segregation of S to γ grain boundaries in Fe-7.6 Ni-0.48 C wt% and Fe-0.61 C wt% alloys was stimulated by the use of a double austenitising treatment, first at 1200°C for 15 mins then various times (0-20 mins) at temperatures between 550 and 800°C. This caused large discs (up to 10 μm in diameter) of iron rich sulphides to be deposited on the prior γ grain boundaries, from which bainite-like laths were seen to emanate after transformation at 440°C. The laths were observed by use of SEM on intergranular fracture surfaces and so could not be unambiguously determined as being bainitic, nor could the nucleation mechanism be deduced. These structures could also be seen, again on fracture surfaces, to have formed around cementite particles (0.1-0.3 μm) at prior γ grain boundaries when enhanced S segregation had not occurred.

Nitrogen levels from 71 to 247 ppm were investigated by Kirkwood ⁽²⁵³⁾, but no microstructural effects were noted, merely a solid solution hardening effect. Although N in stainless steels tends to segregate to and stabilise γ no similar effect on the microstructure of these dilute weld metals was noted on the optical scale used in Kirkwood's work. Any effect may

be confined to regions of retained γ in the microphases, whose proportion would be enhanced, though not as strongly as for Ni, and would require TEM studies to determine. Nitrogen will probably exert a stronger influence in the presence of strong nitride formers, such as B, Al and Ti. In order to retain B in solid solution, where it is able to remove nucleation sites for allotriomorphic α , Ti or Al additions are also made to preferentially tie up N and O. Aluminium nitrides were proposed as nucleation sites for α_{acic} by Cole and Colvin ⁽²⁵⁴⁾ to explain the high proportion of α_{acic} seen in SA welding with a 50% Al_2O_3 flux. However, no analysis at all was made of the inclusion population or for any element changes other than C, Mn, Si and Nb, so that no evidence exists to support this conjecture. Titanium, having a greater affinity for nitrogen than aluminium, is more likely to precipitate nitrides ⁽²⁵⁵⁾, although the proportion of Ti present as TiN in SA welds can be <20% ⁽²⁵⁶⁾. This is due to the higher affinity of Ti for oxygen than for nitrogen; the low proportion of TiN was obtained for welds with 200-300ppm [O], 40-100ppm [N] in the absence of Al ([Ti] \approx 0.017-0.022wt%). The presence of the stronger deoxidant would reduce the amount of oxygen available for Ti oxide formation allowing more TiN to form. The lattice parameter for TiN, which is cubic F, is 4.235Å and this gives a small planar registry of 3.8% with:

$$\begin{array}{c|c} \{100\}_n & || \{100\}_\alpha \\ \hline \langle 010 \rangle_n & || \langle 011 \rangle_\alpha \end{array}$$

Subscript n refers to the nitride.

This prompted North et al. ⁽²⁵⁷⁾ to suggest that the adoption of a low energy interface between TiN and α is responsible for preferential nucleation on these particles, a proposal echoed by Abson ⁽²⁴⁸⁾ and Mori et al. ⁽²⁵⁸⁾. This could then be extended to TiO and TiC, which, with TiN, form the TiX solid solution and so should also give ready lattice matching promoting α_{acic} nucleation. This has been extended by Mori et al. ⁽²⁵⁸⁾, who studied nucleant particles by diffraction and microanalysis in a TEM and found Ti bearing particles with a cubic F structure ($a = 4.12\text{\AA}$) in many nucleating sites. One major criticism of this mechanism, as pointed out by Kayali et al. ⁽²⁵⁰⁾, is that it is extremely unlikely for a random, heterogeneous inclusion population to adopt a cube-on-cube orientation with both γ and α in sufficient numbers to cause nucleation of α_{acic} on the scale observed. In addition, the extra driving force is related to, fig. 6.15:

$$\Delta E_s^c = A_i (\sigma_{\alpha i} - \sigma_{\gamma i} - (\sigma_{\alpha\gamma} - \sigma_{\gamma\gamma})) \quad \dots(54)$$

where

ΔE_s^c = surface energy change at inclusion upon nucleation

A_i = inclusion/nucleus interfacial area

$\sigma_{\alpha i}$ = α /inclusion interfacial energy

$\sigma_{\gamma i}$ = γ /inclusion interfacial energy

$\sigma_{\alpha\gamma}$ = α/γ interfacial energy

$\sigma_{\gamma\gamma}$ = γ/γ grain boundary energy

and hence is likely to be very small.

If γ adopts a high energy disordered interface with the inclusion and, as shown in chapter 4, α_{acic} adopts a low energy K-S orientation with γ , then it is likely that it will also have a disordered interface with the inclusion. This would then give:

$$\begin{aligned}\sigma_{\alpha i} &\approx \sigma_{\gamma i} \\ \Delta E &\Rightarrow 0\end{aligned}\quad \text{.....(55)}$$

More recent research, by Dowling, Corbett and Kerr ⁽²⁵⁹⁾, has produced TEM studies of inclusions and the ferrite nucleated upon them, which failed to give any evidence of epitaxial relationships. The welds were carried out using a B/Ti flux and contained around 80 - 100 % α_{acic} . The TEM study also produce EDS analyses of inclusions in welds with varying Ti, Cr & Mo, but this may not be the most efficient way of deducing inclusion nucleation and various effects on their nucleation efficiency. The very heterogeneous and heterophase nature of a weld metal inclusion may mean that the nucleation is due to one of the minor phases with the subsequent multiple nucleation arising from sympathetic nucleation of α_{acic} on preexisting plates.

The preponderance of oxides and silicates over sulphides and nitrides as weld metal inclusions has concentrated most attention on these and, in turn, mainly on (i) alumina based and (ii) titanium based inclusions. Minor phases such as oxides of zirconium, vanadium, manganese and calcium have also been reported. This division is somewhat artificial as generally an inclusion will contain Al, Ti and minor oxides, so that one is generally not independent of the others. However, trends in each may be highlighted so that the dominant mechanism for nucleation by that phase can be deduced.

In an attempt to account for the variation of allotriomorphic α width, α_{acic} lath size and aspect ratio with cooling rate and alloying, Abson ⁽²⁶⁰⁾ suggested a model for development of microstructure based on active inclusions.

- (i) Nucleation of allotriomorphic α at grain boundaries at $\approx 800^\circ\text{C}$.
- (ii) Growth of allotriomorphic α , with competing nucleation/growth of α_{acic} commencing between $\approx 700^\circ\text{C}$ and 600°C .
- (iii) Nucleation of α_{acic} occurs on oxide inclusions over a range of undercoolings, which he postulated as being due to e.g. inclusion size or composition. Those operating at small undercoolings (where surface/volume ratio is important) give more equiaxed grains, which, if there is limited nucleation around, may form ferrite islands. The plate-like shape develops as temperature decreases so that surface/volume ratio assumes less importance.
- (iv) Acicular ferrite will halt grain boundary ferrite growth and will be stopped by mutual impingement of the laths.
- (v) Increased cooling rate then allows more nucleation, hence there is a refining action on grain boundary ferrite and α_{acic} down to a limit where all inclusions nucleate and no further refinement can be obtained.

This suggests that α_{acic} is a diffusional transformation product, which, as shown in chapter 4, is not correct and does not give any mechanism for nucleation or growth or why a limited oxygen range is needed, other than change in [O] can alter a type (unspecified) of inclusion making nucleation less effective. Also a one-to-one inclusion/lath relationship, i.e. the nucleation of each α_{acic} plate upon an inclusion, is not seen. This was proposed to explain a limiting size of α_{acic} plate, which would be due to nucleation upon all available inclusions and impingement of plates. The displacive nature of the α_{acic} transformation means that the change in aspect ratio may be due to changes in habit plane as the γ lattice parameter varies if α_{acic} is nucleated at different temperatures. Varying strain effects and γ - α driving forces with different alloying could also account for changes in the lath characteristics such as size and shape. The role of surface/volume ratio is negligible by the time that the particles have developed to an observable size; hence it is unlikely to cause a change in the lath morphology. The limiting size of α_{acic} plates will then be due to the limit on bainite lath size, with the interlocking network arising from sympathetic nucleation and plate impingement.

6.4.3.1 Alumina Based Inclusions

The use of alumina based fluxes (and other basic fluxes) compared to acidic SiO_2 fluxes brings about less oxygen transfer to the weld pool and so results in a smaller inclusion population with corresponding increases in upper shelf energy ⁽²⁶¹⁾. The importance of alumina was expressed by Abson, Dolby and Hart ⁽²⁴⁶⁾ who noted that in high, 600ppm [O], welds a change in microstructure from <20% α_{acic} to \approx 70-80% occurred at the expense of grain boundary nucleated side plates and bainite when the flux was changed from a calcium silicate one to an alumina base. However, the change introduced was not solely in the replacement of SiO_2 -CaO by Al_2O_3 -CaF₂, but also increases MgO and TiO₂ (Table VI.2).

Unfortunately, there was no analysis of the nucleant inclusions to determine which of these elements and phases were concentrated in the nucleating particles. Devillers et al. ⁽²⁶²⁾ further studied the effect of alumina flux additions on α_{acic} nucleation at oxygen levels of 270, 440 and 670 ppm. The equilibrium inclusion phases were predicted thermodynamically, assuming equilibrium at 1500°C, which predicted alumina inclusions at low [O] switching to aluminium, manganese silicates with fluxes giving higher [O]. Inclusions were examined after extraction on carbon replicas and nucleating sites were found, by EDS, to be aluminium-manganese silicates without a sulphide coating and containing some Ti. Nucleation was less prevalent at angular Al_2O_3 or sulphide coated inclusions. From this and a study of thermal expansivities (fig. 6.16) the dominant mechanism was proposed to be due to matrix straining around the oxide during cooling. Some data on inclusion populations can be obtained by use of particle analysing scanning electron microscopy (PASEM), which reveals inclusion distribution and dominant elements, i.e. combines EDS with image analysis. Use of this technique with a range of fluxes (calcium silicate, alumina rutile, alumina basic, silica and manganese silicate) ⁽²⁶³⁾ has led to an association of major inclusion elements with microstructural features.

| | |
|-------------------|---|
| Si, Mn | coarse grain boundary α and Widmanstätten α |
| Al, Si, Mn | α_{acic} |
| Ti (rarely major) | α_{acic} |

This technique cannot, however, study an inclusion and its intimate environment and so the results only illustrate general trends not those specific to α_{acic} nucleation.

6.4.3.2 Titanium Based Inclusions

The strong effect of Ti upon the proportion of α_{acic} , especially with Ti-B fluxes has led to a considerable study on the effects of inclusions containing titanium oxides on microstructural development ^(250,256-258,264-270). Kayali et al. ⁽²⁵⁰⁾ studied 4 levels of [Ti] in 0.04 C-1.7Mn-0.4 Si-0.01 Al wt% SA HSLA welds. The lower levels (0.005 and 0.018 wt% Ti) gave a predominantly acicular ferrite microstructure nucleated initially on inclusions containing Al-Mn-Si-Ti, Al-Ti-Mn and Ti-Al-Mn, which were largely spherical. The oxygen level was $\approx 460\text{ppm}$. The two higher levels (0.090 and 0.230 wt% Ti) gave wholly lath structures indicative of increased hardenability (more Ti in solid solution) and lack of inclusion nucleation behaviour. This was associated with an increase in angularity of the inclusions, which were predominantly Ti-Al, Ti or Ti-Mn oxides, carbides or nitrides. These were subsequently identified as a TiX phase, probably TiO. The inclusions themselves were multiphase so that the statement that it was e.g. Ti-Al oxides refers to the fact that it contained regions of aluminium oxides and other regions of titanium oxides. The highest [Ti] level, achieved through flux additions, caused a large increase in [O] to 662 ppm and may not be valid for comparison. In the presence of boron, almost 100% α_{acic} can be achieved at [Ti] levels of 0.02-0.029wt% ⁽¹²¹⁾, within the range noted above, again [Al] $\approx 0.01\text{wt\%}$, [O] $\approx 400\text{ppm}$. The inclusions in this case showed a greater interfacial bond strength with the weld metal, being more embedded in the fracture surfaces studied and displaying some angularity. Low levels of Ti (0.003wt%) can result in α_{acic} formation in SA welds at oxygen levels of up to 1200ppm ⁽²⁶⁸⁾ by suitable alloying with Mn (and Si). This will have two main effects.

(i) The overall hardenability of the system will be altered so enhancing any effects of inclusions on nucleation as grain boundary nucleation becomes significantly more difficult. This would combat any decreased grain size effect at higher [O].

(ii) The increased proportions of Mn and Si would soak up any excess oxygen whilst still leaving titanium oxides so that the inclusions would contain Ti oxides supported upon manganese silicates. However, the nature of the inclusions at these oxygen levels was not investigated.

The behaviour of Ti with respect to inclusions has been investigated in relation to other flux additions, such as Al, Mn and Si. The poor toughness of MIG weld metal below 100ppm oxygen was studied in Ti-B fluxed systems ⁽²⁵⁶⁾. Two main effects were noted in the low oxygen regime.

(i) The total number of inclusions dropped from $17.5 \times 10^3 \text{ mm}^{-2}$ at 309 ppm to $7 \times 10^3 \text{ mm}^{-2}$ at 54 ppm, which reduces the total number of nucleation sites. The numbers were determined from optical micrographs and so would underestimate the number of fine ($<0.3\mu\text{m}$) particles present,

although these would be expected to vary in a similar way.

(ii) Below 70-100ppm [O], the proportion of Mn, Si and Ti in the oxide inclusions was reduced almost to zero, whereas there was a dramatic rise in the proportion of Al based oxides. This is consistent with the stronger oxygen affinity of Al compared with Mn, Si and Ti and so it is able to consume the vast majority of the available oxygen.

These changes in inclusion population were accompanied by a change in microstructure from predominantly α_{acic} (>100ppm) to grain boundary nucleated bainite (<100ppm) indicating the change in type and distribution of inclusions has drastically reduced the efficiency of intragranular nucleation.

These trends have been generalised into ratios of elements present and minimum amounts, so that Saggese et al. ⁽²¹⁸⁾ found the proportion of α_{acic} fell rapidly if the Ti content of inclusions fell below $\approx 2\%$. This figure must be treated carefully as excess Ti leads to large increases in hardenability and the replacement of α_{acic} by bainite ⁽²⁵⁰⁾. These inclusions also, generally, contain >50% Al_2O_3 and roughly equal proportions of SiO_2 and MnO_2 ^(111,218,271). The trend for alumina shows an initial rise in α_{acic} fraction with increasing alumina content, then a sharp drop above 50% Al_2O_3 , fig. 6.17; this decrease can be removed if Ti additions are made at high alumina contents, if sufficient oxygen is available. The two sides of the peak then explain decreases in toughness with:

(i) Change from alumina to aluminium-manganese silicates with increased oxygen content ^(212,239) to the left of the peak.

(ii) Increasing alumina to the right.

Attempts to fit Al/O and Al/Mn ratios have not succeeded in predicting the presence of large amounts of α_{acic} ⁽²⁶⁷⁾, where no epitaxial nucleation of α_{acic} on galaxite $\text{Al}_2\text{O}_3 \cdot \text{MnO}$ was observed.

Some recovery of Ca, Mg, Y, Nb, Zr and V from flux or base plate has been noted with oxides of these elements being present in some inclusions, though as minor phases compared to Al, Si, Mn and Ti ⁽²⁷¹⁻²⁷⁴⁾. These appear to have a minor effect upon nucleation of α_{acic} .

It therefore appears that Ti rich particles are necessary for the nucleation of α_{acic} , although vanadium and zirconium oxides may give similar, smaller effects. In addition, alumina and silica phases are also present with sulphides such as Cu_xS and MnS , the latter not having been shown to nucleate α_{acic} . Despite this, the actual mechanism(s) promoting α_{acic} nucleation have not been identified, several having been proposed:

(i) Lattice matching. This would be particularly strong for the TiX phases and would explain the dependence on Ti content, but has drawbacks as noted above.

(ii) Thermal strains. The differential thermal expansivities between inclusions and steel give rise to thermal strains during cooling of the weld. This has been mathematically modelled by Brooksbank and Andrews ⁽²⁵¹⁾ for wrought steels and the strain field round an inclusion compared to a grain boundary would increase the driving force for transformation and promote nucleation

on the inclusion. The large strain energy associated with both α_{acic} and bainite transformations ($\approx 400 \text{ Jmol}^{-1}$) and recovery of sufficient strain energy would be highly beneficial. This mechanism depends strongly upon the thermal expansivity of the inclusion and its interface strength with steel, as stress transfer rather than decohering is required. This may be why pure sulphides are inefficient as they decohere too readily and do not provide strain energy in the α_{acic} transformation range. The size and distribution of the inclusions will also play a part, as there will be interactions between the strain fields of adjacent particles at small spacings, as indicated by Barritte ⁽⁵⁷⁾. However, the thermal expansivities of oxide particles do not show large variations and so the effect of a change from titania to alumina inclusions would not be expected, only a decrease in the total population, assuming stress transfer is equally effective.

(iii) Dislocation punching. Taking (ii) further the thermal strain around larger particles is sufficient to cause yielding in the steel and so the particles act as sites for nucleation of dislocations. These are required to perform the shear component of the γ to bainite sub-unit formation. These can be nucleated at temperatures below 700°C and so would be available in the α_{acic} transformation range. Dislocations around inclusions were illustrated by Ferrante ^(275,276), but these were not indexed and it is not clear whether these could accomplish the γ to α transformation. This mechanism would depend on the same inclusion parameters as (ii) and so would also not explain the dependence upon Ti bearing inclusions.

(iv) Hardenability effects. The hardenability of a steel depends upon its grain size, the finer it is the easier formation of grain boundary phases such as bainite becomes. Cochrane & Kirkwood suggested that the pinning action of inclusions alters grain size to allow the homogeneous nucleation of α_{acic} intragranularly. The large amount of evidence for direct nucleation on inclusions refutes this and homogeneous nucleation in the presence of so many heterogeneities is energetically very unlikely.

(v) Inert surface. Many researchers have decided on the action on inclusions as inert surfaces as being the mechanism for nucleation. There would then be no chemical composition favoured and only the number and size of inclusions would determine the effective nucleating behaviour, subject to grain boundary pinning. In order to fully verify this mechanism a large series of welds with varying inclusion populations would have to be microstructurally quantified followed by a full characterisation of inclusion contents i.e. size distribution and phase relationships would have to be undertaken. To date such a massive study has not been undertaken, although several of the references above provide supportive evidence.

(vi) Chemical heterogeneities. The depletion of substitutional alloying elements around an inclusion due to its formation has already been considered (section 6.3.3). The turbulent nature of the weld pool in which the inclusions form, removes such composition gradients making this an unlikely mechanism for nucleation. Microanalytical results ⁽⁶⁵⁾ fail to show any substitutional alloying element depletion around nucleating inclusions.

Therefore, despite a large amount of evidence, there is no coherent theory for nucleation of α_{acic} or which (if any) of the above mechanisms acts under different conditions. It is this that this project will attempt to determine as the identification of the most efficient nucleant will allow total inclusion content to be reduced to optimise toughness under both cleavage and ductile failure conditions.

(241) Table VI.1. Values of critical inclusion sizes (d_{cr}) and inclusion densities from Liu & Olson

| $\gamma_{gs}/\mu\text{m}$ | f_v | $d_{cr}/\mu\text{m}$ | $N_v/10^8\text{mm}^{-3}$ | F | $n_b/10^8\text{mm}^{-3}$ |
|---------------------------|--------|----------------------|--------------------------|------|--------------------------|
| 55 | 0.033 | 0.27 | 7.60 | 0.82 | 6.23 |
| 85 | 0.0040 | 0.51 | 2.01 | 0.85 | 1.71 |
| 85 | 0.033 | 0.42 | 2.99 | 0.88 | 2.63 |
| 55 | 0.0051 | 0.42 | 6.40 | 0.87 | 5.57 |
| 80 | 0.0033 | 0.40 | 3.27 | 0.86 | 2.81 |
| 88 | 0.0025 | 0.33 | 1.54 | 0.72 | 1.11 |

where:

- γ_{gs} =austenite grain size
- f_v =inclusion volume fraction
- N_v =inclusion number density
- F=fraction of inclusions at γ grain boundaries
- n_b =inclusion density associated with prior γ grain boundaries

Table VI.2. Compositions in wt % of calcium silicate (80R) and alumina (Lincoln 11) fluxes.

| Flux | SiO ₂ | TiO ₂ | ZrO ₂ | Al ₂ O ₃ | MnO | CaO | MgO | K ₂ O | CaF ₂ |
|------------|------------------|------------------|------------------|--------------------------------|-----|------|------|------------------|------------------|
| 80R | 15.7 | 0.5 | 0 | 12.1 | 5.1 | 26.7 | 12.6 | 0.2 | 10.0 |
| Lincoln 11 | 15.6 | 4.0 | 0.1 | 21.4 | 3.2 | 3.2 | 24.4 | <0.1 | 26.9 |

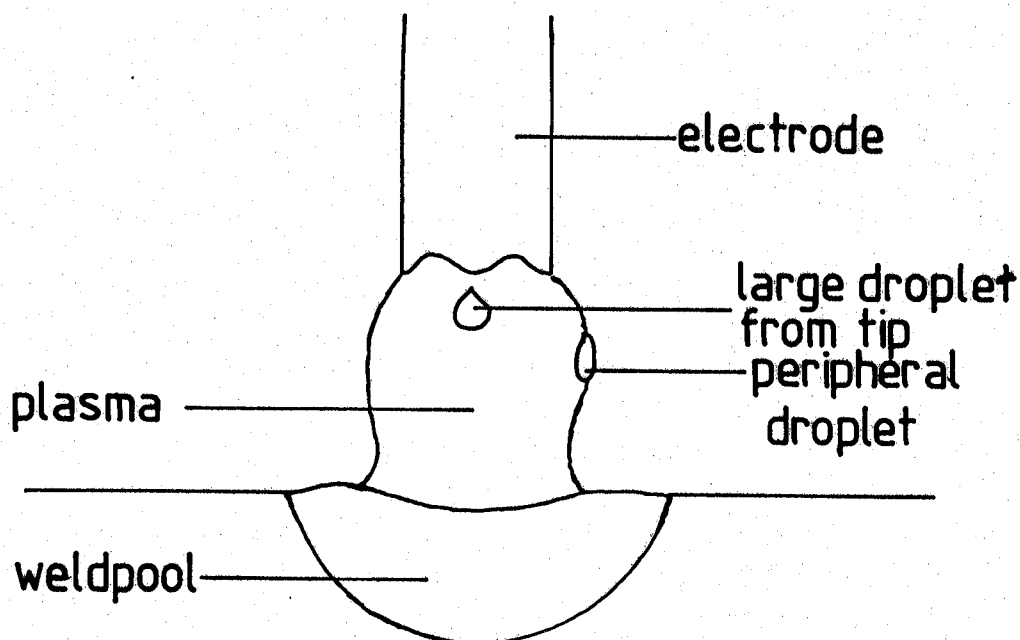


Figure 6.1. Element arc transfer routes.

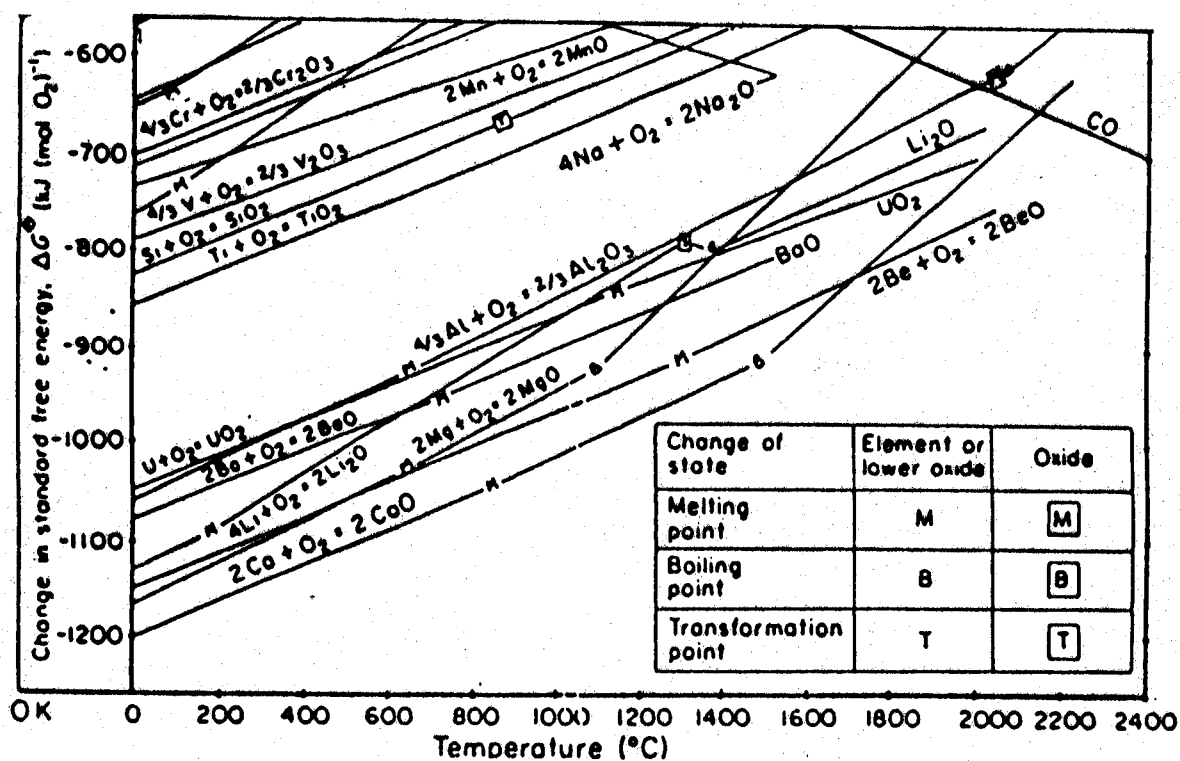
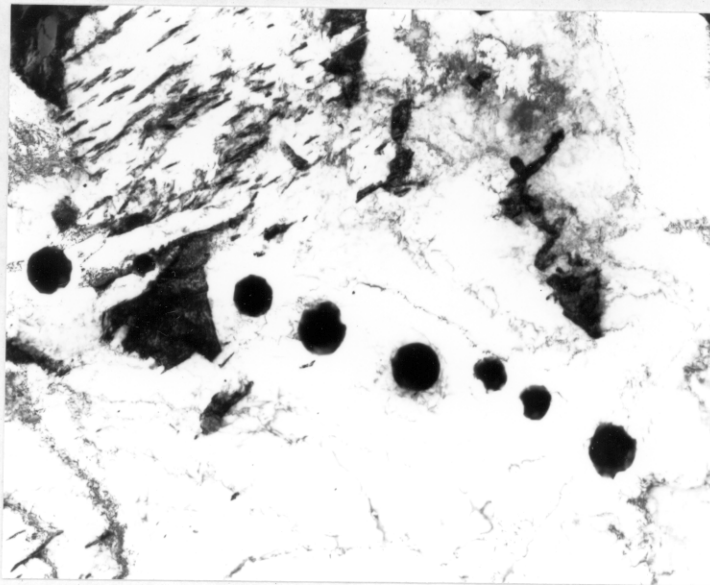


Figure 6.2. Ellingham diagram for selected oxides.



1.0 μm

Figure 6.3. Aligned weld metal inclusions.

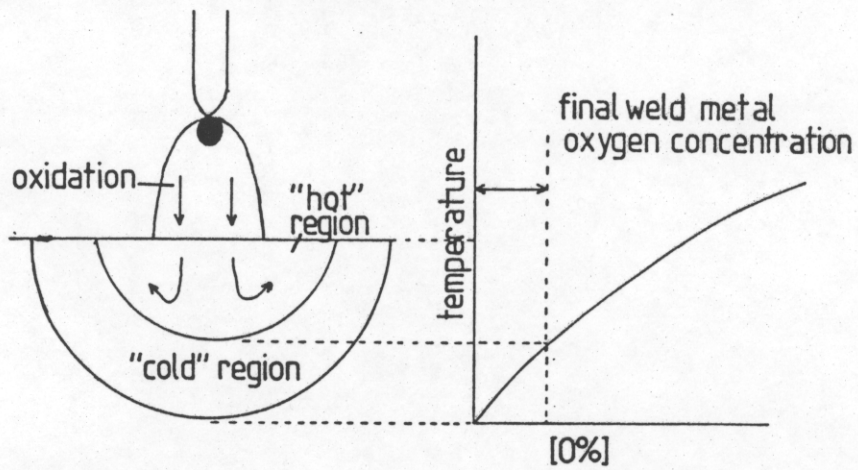


Figure 6.4. Hot and cold weld pool regions ⁽²¹³⁾.

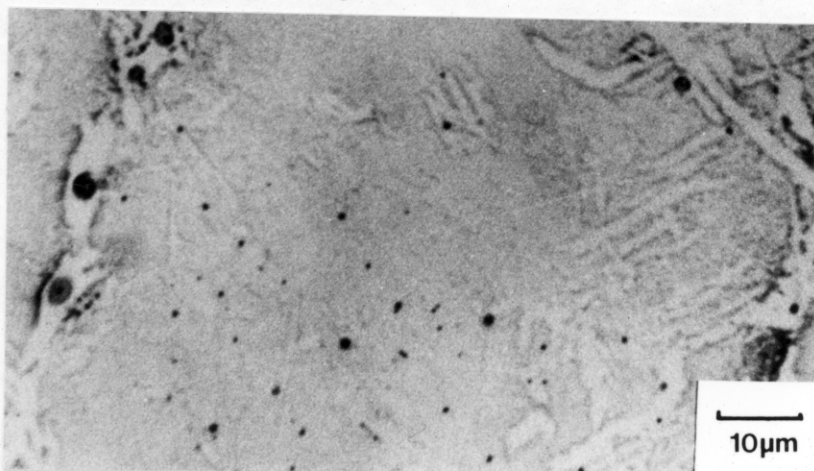


Figure 6.5. Segregation of inclusions to solidification boundaries ⁽²¹⁶⁾.

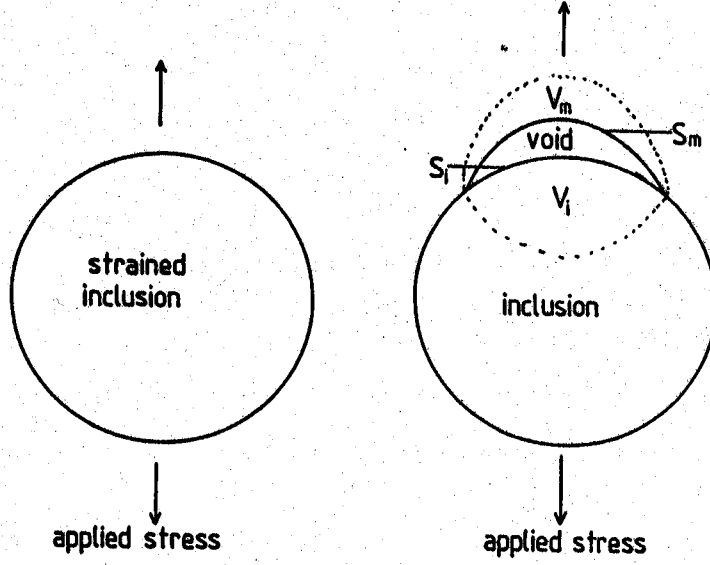


Figure 6.6. Nucleation of a void around a second-phase particle by particle/matrix interface decohesion.

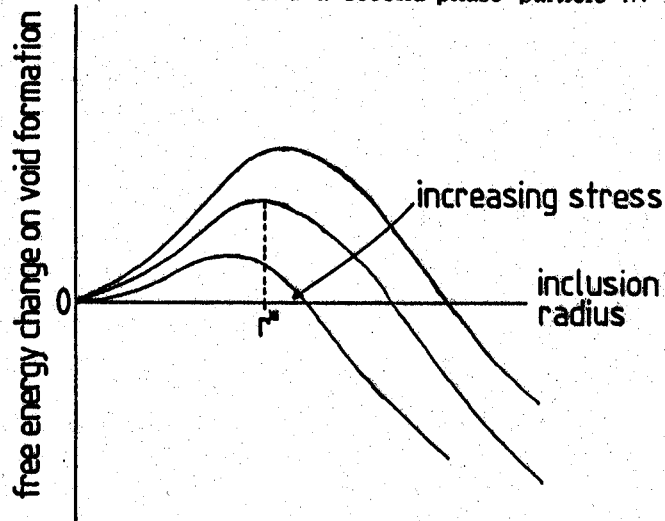


Figure 6.7. Energy balance for interface decohesion around a second-phase particle.

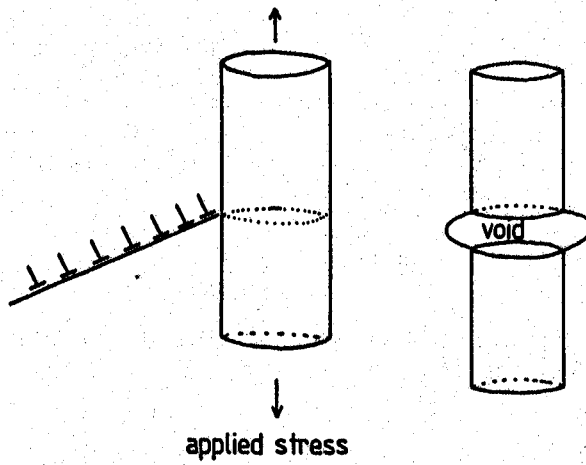


Figure 6.8. Particle cracking due to dislocation pile-ups.

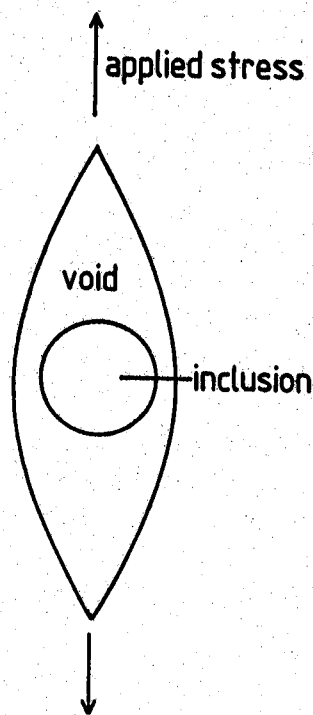


Figure 6.9. Growth of void around a second-phase particle.

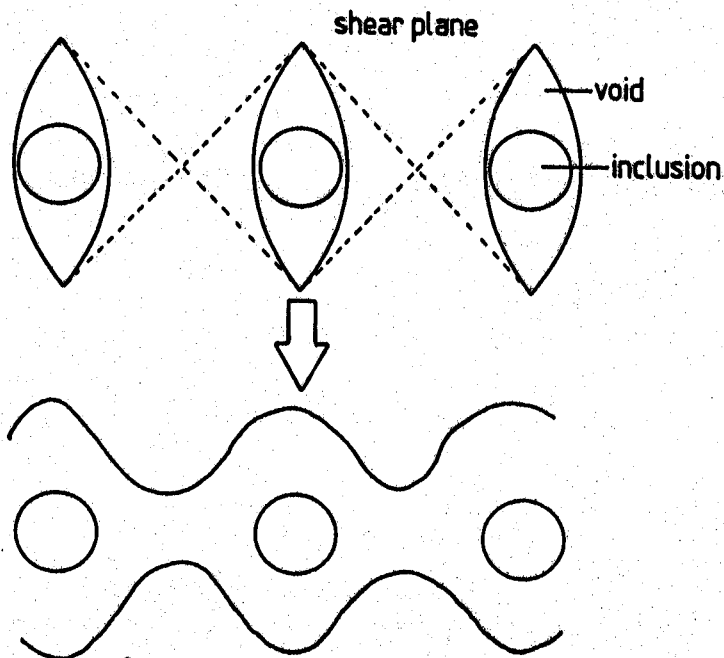


Figure 6.10. Coalescence of voids by internal necking.

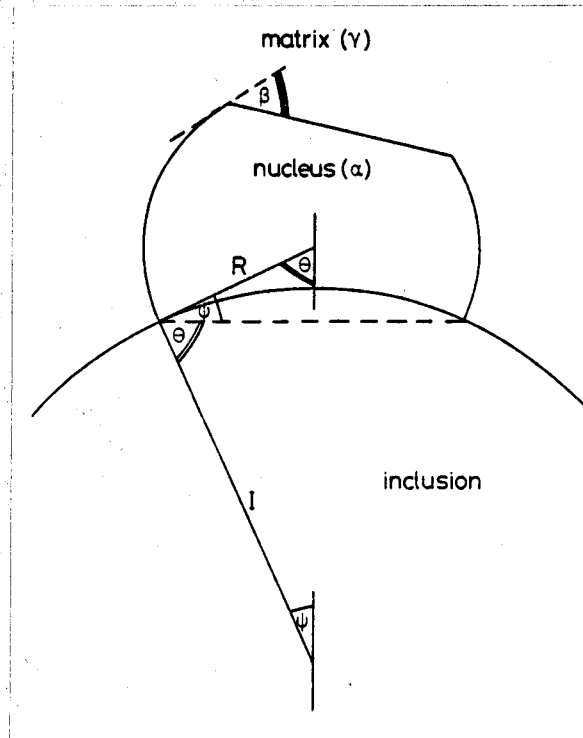
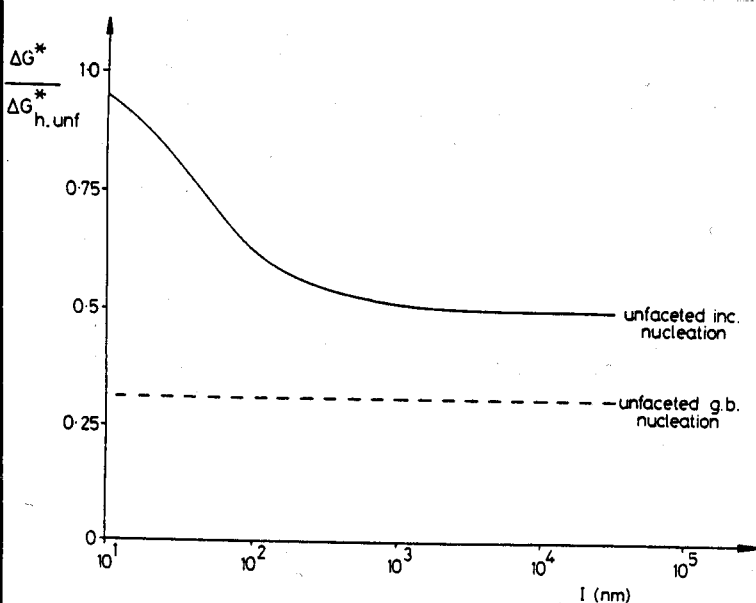


Figure 6.11. Barritte's ⁽³⁷⁾ analysis for the activation energy for nucleation, ΔG^* , as a function of radius, I . Facetted spherical nucleus is also shown.

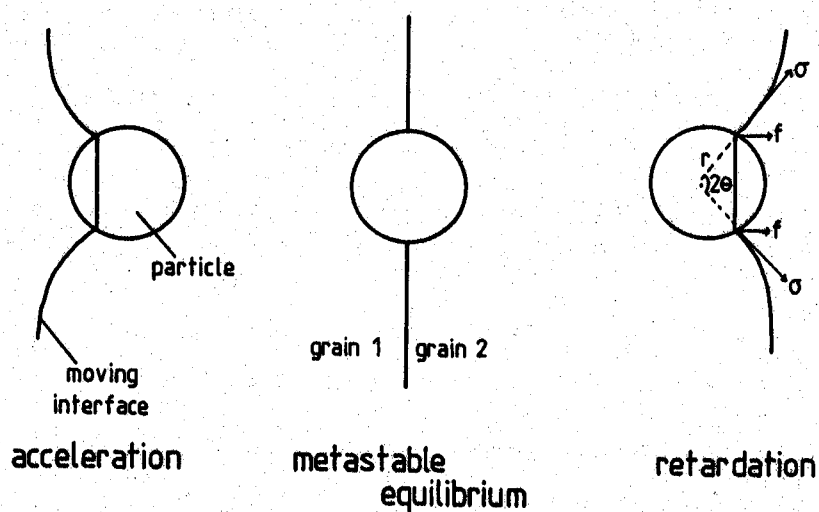
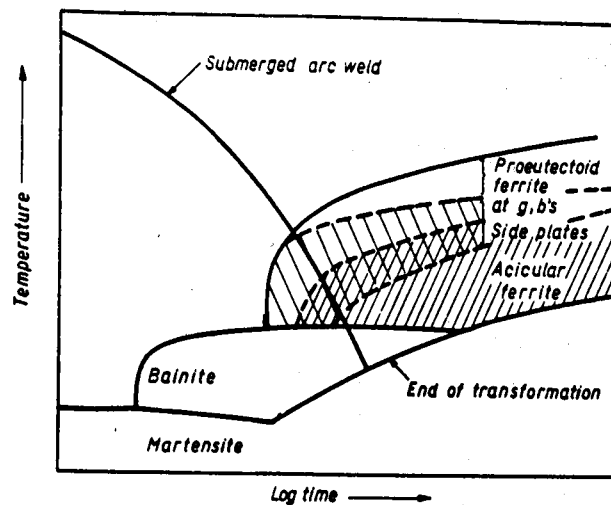


Figure 6.12. Interaction of a moving boundary with a particle.

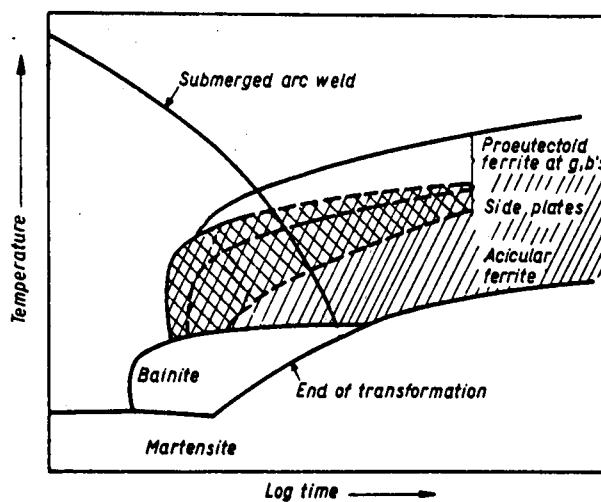
(a) LOW OXYGEN

0.01 % O_2



(b) MEDIUM OXYGEN

0.03 - 0.04 % O_2



(c) HIGH OXYGEN

0.06 % O_2

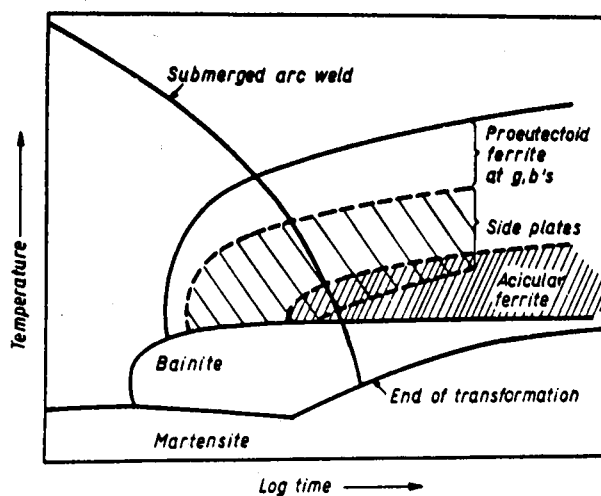
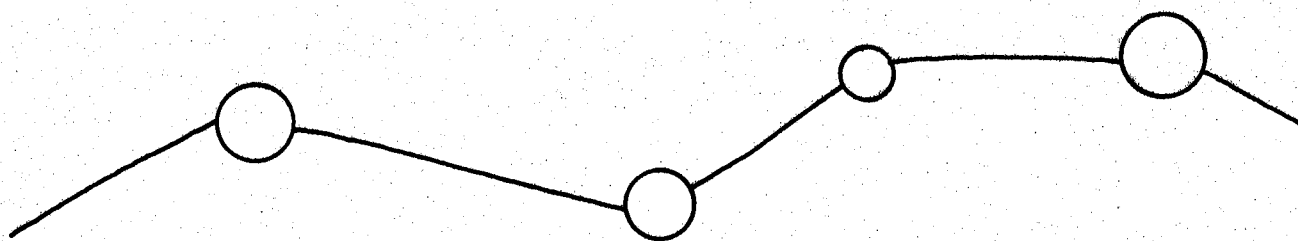
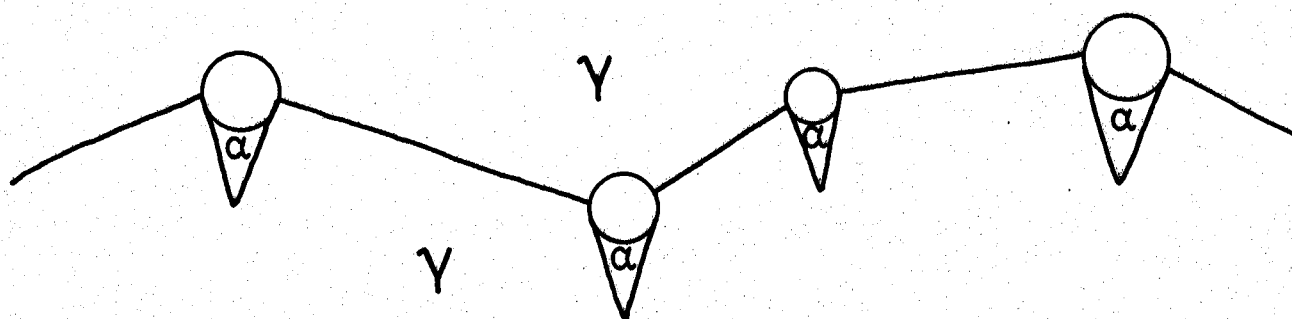


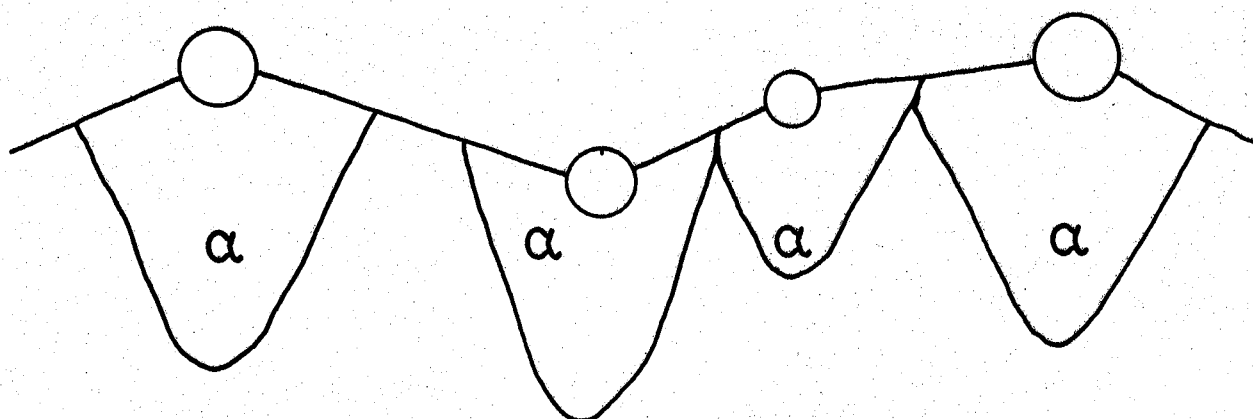
Figure 6.13. Welding Institute CCT curves to show proposed effect of oxygen upon transformation behaviour ⁽²⁴⁶⁾.



oxide particles pin γ grain boundaries
making them wavy



α nucleates preferentially on oxide particles



interfacial instabilities promote sideplates

Figure 6.14. Cochrane and Kirkwood's ⁽²⁴⁴⁾ model for sideplate formation.

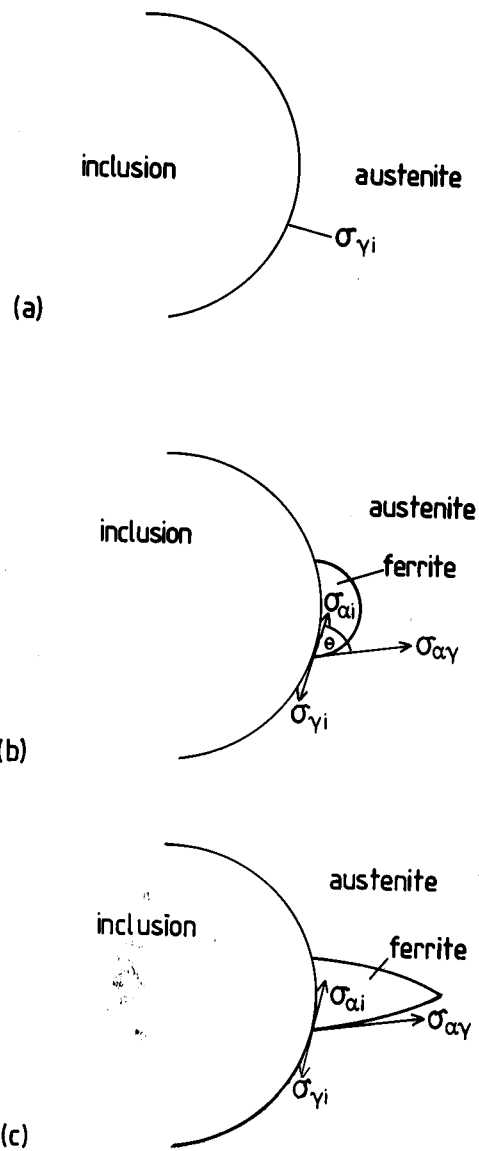


Figure 6.15. Various forms of inclusion nucleation.

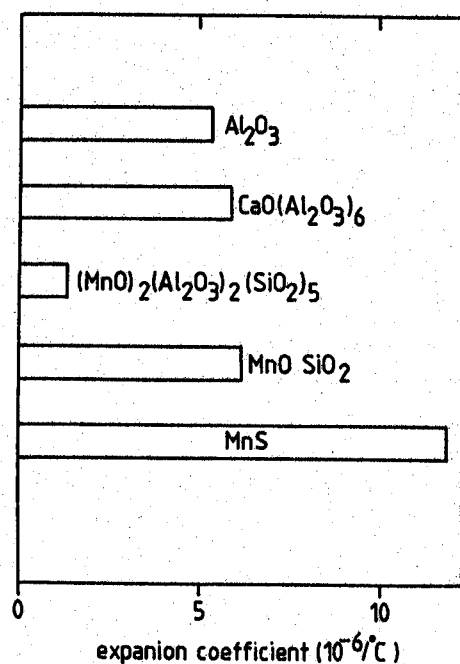


Figure 6.16. Thermal expansivities of various inclusion phases.

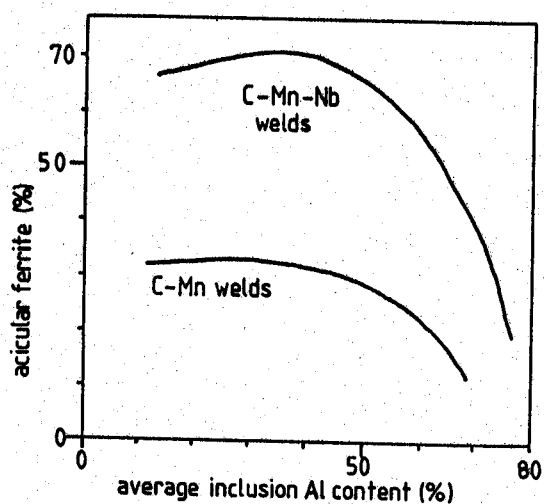


Figure 6.17. Variation of % α_{acic} with flux aluminium content.

7. Segregation, Oxygen Content and the Transformation Start Temperature in Steel Weld Deposits

7.1 Introduction

In order to accurately predict weld metal microstructures the volume fraction of allotriomorphic ferrite must be calculated with precision, as any errors in this are magnified when calculating the volume fractions of subsequent phases. In its current form the BSG model does not take account of the oxygen level in the weld metal, although there are reports that this element may affect the austenite to ferrite transformation start temperature ($T_s^{\gamma-\alpha}$)^(63,244). However, this is not universally accepted and, as mentioned above, doubts have been expressed over the relative roles of oxygen content and γ grain size. In modelling the formation of ferrite on prior γ grain boundaries by the unidirectional advance of a planar interface then $T_s^{\gamma-\alpha}$ becomes an extremely important parameter as it determines the time available for diffusional advance of the γ/α interface before displacive reactions dominate. In view of the lack of agreement upon the effect of oxygen on $T_s^{\gamma-\alpha}$ an investigation into this was undertaken. Due to the numerous changes brought about by varying fluxes in addition to changes in oxygen level, it was decided to contrast and compare the transformation behaviour of a weld with a pure alloy of identical composition except for oxygen and nitrogen. In this way the effect of oxygen can be studied independently of other alloy effects.

7.2 Experimental

Three multipass, submerged arc welds were provided by ESAB AB,¹ whose compositions are given in Table VII.1. 65g melts of pure alloys of similar compositions (except O and N) were prepared using a vacuum arc furnace, their compositions also being given in Table VII.1.

A number of 3mm diameter rods were machined from each weld samples parallel to the welding direction, some of which had a 1.2 mm diameter hole drilled along the axis, fig. 7.1. The rods were identified by their position in the weld, fig. 7.2. Homogenised rods were prepared by sealing in a quartz tube, after flushing three times with argon, pumping down to a pressure of 10^{-6} torr and backfilling with a partial pressure of argon before final sealing and heating at 1200°C for 3 days. This procedure is sufficient to remove microsegregation within the rods, but not macrosegregation effects, such as dilution from the baseplate. This was later seen in the

¹ The nomenclature for these welds are W1(=3499), W2(=3501), W3(=3519) and pure alloys P1(=MSPA2), P2(=MSPA3), P3(=MSPA1).

substantially different transformation behaviour of those rods adjacent to the HAZ (e.g. 1, 6, 10 in fig. 7.2). The data from these were discarded as they were not representative of the bulk weld metal and only those relatively undiluted regions towards the centre and top of the weld were used.

The pure alloy melts were homogenised in a similar way to the weld rods and then cold swaged from 11mm to 4mm in 1mm steps. After an anneal at 600°C for 30mins, they were further swaged to 3.2mm, given a second anneal (600°C/30mins) and finally cold swaged to 3mm diameter.

The small radius of the specimen gave a high surface/volume ratio (especially in the hollow specimens), which may lead to surface nucleation effects. These were assessed by using an homogenised weld specimen cut into two halves; one half being nickel plated,² whilst the other was not. Both specimens were transformed over a series of cooling rates in a Theta Industries high speed dilatometer, under a slight pressure of helium to reduce decarburisation and surface oxidation, after austenitising for 10 minutes at 1000°C.

The results, fig. 7.3, indicated a strong effect of surface nucleation with the unplated specimen having a $T_s^{\gamma-\alpha}$ 40-100°C greater than that of the plated specimen. The difference between the $\gamma-\alpha$ transformation start temperatures for the plated and unplated specimens increased as the alloy content of the welds increased. This variation with alloy content is expected as surface nucleation is relatively insensitive to alloy content, so that $T_s^{\gamma-\alpha}$ remains fairly constant. As alloy content increases, however, grain boundary nucleation is inhibited depressing $T_s^{\gamma-\alpha}$ to lower temperatures and increasing the difference between this and the temperature corresponding to nucleation at the free surface. All specimens were subsequently nickel plated.

7.2.1 Theta Industries High Speed Dilatometer

This machine and its operation were described in detail in chapter 3 for isothermal transformations. The only difference here being the study of continuous cooling transformations (CCT), so that, after reaustenitisation, the specimen is cooled at a constant rate controlled by the Data-Trak programmer. High cooling rates were achieved by continuous use of a helium quench. The data was recorded on a Honeywell chart as temperature versus time (distance along chart) and length change versus time or on disc as length, temperature (T) and time (t) via a BBC microcomputer. These were replotted as $\Delta L/L_0$ (ΔL =length change at T, t; L_0 = initial specimen length) vs T from which $T_s^{\gamma-\alpha}$ could be measured, fig. 7.4. The high temperature linear region of the $\Delta L/L_0$ vs T plot represents the thermal contraction of 100% γ and so the slope represents the thermal expansivity of γ . This is constant over the temperature range studied, but once ferrite starts to form the mean linear expansivity of the specimen varies and so the curve will deviate

² A two stage treatment:

Strike: 3 minutes at 50°C, 775mAcm⁻², electrolyte 250g NiSO₄+27ml. conc. H₂SO₄ made up to 1 litre in distilled water.

Plate: 25 minutes at 35°C, 40mAcm⁻², electrolyte 140g NiSO₄+140g Na₂SO₄+15g NH₄Cl+20g Boric acid made up to 1 litre in distilled water.

from the straight line plot. If a least squares line is fitted to the linear portion of the curve, then the initial formation of ferrite can be found from the point where the curve starts to deviate from that least squares line. Such a method allows $T_s^{\gamma-\alpha}$ to be determined to an accuracy of within $\pm 5^\circ\text{C}$. In order to confirm the trends indicated for $T_s^{\gamma-\alpha}$, the temperatures for 10% ($T_{10}^{\gamma-\alpha}$) and 100% ($T_{100}^{\gamma-\alpha}$) transformation were also recorded. These were obtained by extrapolation of the linear regions (corresponding to 100% γ and 100% α) then finding the vertical section where the actual length change/temperature plot split these in the ratio 1:9 for 10% transformation. The end of the transformation is the first temperature at which the plot again becomes linear; this parameter was not used as the wide range of cooling rates meant that, whereas $T_s^{\gamma-\alpha}$ always corresponded to the formation of grain boundary allotriomorphic ferrite, there was a variation in the nature of the final ferrite phases to form.

7.3 Continuous Cooling Transformation (CCT) Measurements

CCT curves (for $T_s^{\gamma-\alpha}$ and $T_{10}^{\gamma-\alpha}$) were determined over a range of linear cooling rates for:

- (i) Homogenised samples of each weld
- (ii) As-deposited (segregated) samples of each weld
- (iii) Homogenised samples of each pure alloy

The different cooling rates were achieved by using different Data-Trak program times and are given in Table VII.2. Each sample was reaustenitised at 1000°C for 10mins.

The measurements were repeated on 2 or 3 samples in each case to ensure reproducibility and ascertain approximate errors.

For each weld and pure alloy the CCT curve was also calculated using TTT curves predicted using a program based upon modifications of Russell's ⁽⁸¹⁾ nucleation work ^(144,145). The CCT curve was obtained from the TTT curve by use of the

$$\sum_i t_i/\tau_i = 1 \quad \text{.....(56)}$$

where i =Temperature step

t_i =time spent at temperature i

τ_i =incubation time at temperature i

criterion for the start of transformation, fig. 7.5 ⁽⁹⁴⁾.

In order to assess the importance of oxygen content upon $T_s^{\gamma-\alpha}$, various other possible effects were initially investigated so that their role may be deduced.

7.3.1 Effect of Austenitising Treatment

7.3.1.1 Austenitising Time

Whilst keeping austenitising temperature (T_γ) constant at 1000°C , homogenised weld and pure alloy specimens were austenitised for

10, 30 and 45 minutes each

prior to transformation at 3 different cooling rates, 425, 125 and $25^{\circ}\text{Cmin}^{-1}$. Transformation temperatures were then determined as outlined above.

7.3.1.2 Austenitising Temperature

For homogenised specimens of each weld and pure alloy a series of transformations was carried out using a constant cooling rate. The specimens were each reaustenitised for 10 minutes at temperatures of:

1000, 1050, 1100, 1150 and 1200°C

prior to transformation.

Specimens were also helium quenched to ambient temperature after 10 minutes at:

(i) 1000°C

(ii) 1200°C

for prior austenite grain size measurements which were carried out on a Quantimet 720 image analyser, using upward of 50 fields to reduce statistical scatter.

7.3.2 Fast Cooling Rates

Specimens of each weld and pure alloy were given a series of quenches using helium of varying flow rates, fast program times and finally natural cooling in vacuum. These achieved cooling rates of $\approx 20\text{-}60^{\circ}\text{Cs}^{-1}$ and times to cool from $800\text{-}500^{\circ}\text{C}$ ($t_{800-500}$) of 8-20s.

7.3.3 Repeated Cycling

As the specimens above were subjected to several transformations, test specimens (segregated and homogenised) were given 11 identical thermal cycles to gauge the extent of any variation in $T_s^{\gamma-\alpha}$ induced through repeated cycling. The thermal cycle used was reaustenitisation at 1000°C for 10 minutes followed by cooling at $200^{\circ}\text{Cmin}^{-1}$ and the variation in $T_s^{\gamma-\alpha}$ is shown in fig. 7.6. This indicates some scatter, but overall little consistent variation. A slight increase in $T_s^{\gamma-\alpha}$ noted on cycling may result from increased decarburisation or a change in γ grain structure.

7.3.4 Order of Testing

Specimens were generally tested from faster cooling rates to slower, so this order was reversed for some specimens to see if any change in transformation temperatures resulted. No change was detected and so the same order was adopted for all specimens.

7.3.5 Specimen Position

As mentioned previously, specimens from regions suffering high baseplate dilution were not used as their compositions did not represent the bulk weld composition and behaviour.

7.4 Results and Discussion

The CCT curves for the γ - α transformation start temperature for each weld/pure alloy combination are plotted in fig. 7.7, along with predicted curves. The predicted CCT curves were derived by application of the additive reaction rule, equation 56, to computed TTT curves (assuming homogeneous alloys). Also plotted are CCT curves for 10% transformation (fig. 7.8). Comparison of these curves shows the following trends.

The shapes of the theoretical and experimental curves are very similar indicating that the effect of cooling rate was as expected.

The predicted CCT curve for the homogenised case was found to lie below the experimental homogenised weld curve by 10-20°C, the difference decreasing slightly with increasing cooling rate. This would give rise to some underestimation in the volume fraction of grain boundary ferrite. This is probably due to either approximations made in deriving the TTT curve, the errors in Russell's incubation time approach becoming large at very small undercoolings and near the bay in the TTT curve. Alternatively, approximations made in the use of the additive reaction rule in converting TTT curves into CCT curves may be responsible. The additive reaction rule is known not to apply to the lower C (displacive) curve, but the reason is, at present unclear, and so may become less valid towards the bay region as well. The effect of such an underestimation in $T_s^{\gamma-\alpha}$ can be calculated from the BSG model ⁽²⁷⁾. For a weld, whose composition is identical to W1, welded using the parameters in Table VII.3, then a change in $T_s^{\gamma-\alpha}$ from 760 to 780°C results in a predicted variation of only 0.01 in the volume fraction of allotriomorphic ferrite (0.37-0.38). This arises because the growth rate of allotriomorphic ferrite is very slow around $T_s^{\gamma-\alpha}$ and very little transformation takes place between the two temperatures.

Comparison of the data from homogenised welds W1 and W2 with alloys P1 and P2 respectively shows that there is excellent agreement between these samples, even though the welds contain considerably higher oxygen levels. This proves that oxygen concentration, up to 200 ppm, does not influence the transformation start temperature of austenite. This is different from published work which is believed to be based on an incorrect interpretation of dilatometric curves, from experiments in which the specimens are not protected from effects such as surface nucleation.

The data from homogenised specimen W3 and alloy P3 cannot be compared directly, but when allowance is made for the difference in carbon concentration (fig. 7.7c), it is clear that both show equally good agreement with calculated data, consistent with the above conclusion.

The effect of alloying element segregation is evident from fig. 7.7. The transformation start temperatures for the unhomogenised welds are typically 30-60°C higher than those for the homogenised welds, the difference increasing with average alloy content. The amplitude of composition differences in a given alloy must increase with average alloy content, since it is given by the product of the average composition and the partition coefficient during solidification. Thus, the influence of segregation should be most pronounced for more heavily alloyed materials.

We note that one important effect of segregation is to increase the amount of allotriomorphic ferrite content of welds, by raising the temperature at which this ferrite first forms. It can be seen from fig. 7.7 that the procedure for calculating the effect of chemical segregation⁽²⁷⁸⁾ on $T_s^{\gamma-\alpha}$ works well; the experimental data from the unhomogenised weld agree with the CCT curves calculated for the solute-depleted regions. The CCT curves for segregated welds are predicted by calculating the equilibrium partition coefficients between the initial solidification phase (γ or δ) and liquid for the alloying elements present. This allows the concentrations of these elements to be calculated in the first solid to form (i.e. the solute depleted region) and the TTT curve for this can then be computed as above for conversion to a CCT curve. The underestimation of $T_s^{\gamma-\alpha}$ still exists, but now between the predicted and segregated welds, so allowing a more accurate prediction of $T_s^{\gamma-\alpha}$ for weld metal assuming equilibrium partitioning of solute between solid and liquid. The underestimation again suggests some approximation in the calculation of the CCT curves could be improved either in the TTT curves or in their conversion.

Similar trends are observed for both $T_s^{\gamma-\alpha}$ and $T_{10}^{\gamma-\alpha}$ curves, with the $T_{10}^{\gamma-\alpha}$ curve lying much closer to the predicted line for the homogeneous case giving an approximate indication of the discrepancy between prediction and theory. This corresponds well to the 10% difference between the two noted for weld 4 in ref. 8, a weld of similar composition to those used here. The deviation between theory and experiment will depend on segregation levels, which were not quantitatively measured here, and will also vary with alloying content. In general, the higher the alloy content, then the greater the degree of segregation.

The effect of austenitising time on transformation temperatures was found to be negligible; the variation was less than the scatter noted in repeated cycling, which was $\pm 10-15^\circ\text{C}$, with no noticeable trend.

The variation of $T_s^{\gamma-\alpha}$ with austenitising temperature (T_γ) is shown in fig. 7.9. This indicates a steady decrease in $T_s^{\gamma-\alpha}$ as T_γ increases consistent with the theory that $T_s^{\gamma-\alpha}$ is determined by grain boundary nucleation of ferrite. As T_γ increases the grain size increases causing a decrease in the number of nucleation sites and a corresponding decrease in the transformation start temperature as the nucleation rate is reduced.

The grain sizes produced in both homogenised welds and pure alloys by austenitising at 1000°C and 1200°C are shown in Table VII.4.

The programmed linear cooling rates correspond well to those typical of submerged arc welds and, as noted above, the discrepancy between homogenised welds and theory appeared to decrease as cooling rate increased. Attempts to use helium and vacuum quenches to further decrease the cooling rate were unsuccessful as the surface cooled much more rapidly than the bulk. This resulted in surface cooling rates of the order of $60-80^\circ\text{C s}^{-1}$, which should give martensitic structures. The bulk structure was, however, grain boundary allotriomorphic and Widmanstätten α indicative of much slower cooling rates. This problem may be overcome by the use of reduced specimen radius or hollow specimens, although surface effects may then become dominant.

The effect of segregation is seen to be important indicating depletion of γ -stabilisers and/or excess of α -stabilisers at prior γ grain boundaries. This segregation would arise from the original solidification structure. The enhanced driving force then existing increases $T_s^{\gamma-\alpha}$ and initial growth rate.

An attempt was made to relate $\Delta L/L_0$ to ferrite volume fraction V_α by computer modelling, using the change in lattice parameters on transformation and expansivities derived by regression analysis on the linear portions of the $\Delta L/L_0$ vs T curve (fig. 7.2). This neglects slight changes in the austenite lattice parameter (a_γ) due to segregation but uses a_γ calculated from bulk alloy content based upon the work of Dyson and Holmes ⁽¹⁶⁹⁾. The ferrite lattice parameter (a_α) was determined by sealing a specimen in quartz tube under a partial pressure of argon and annealing at 500°C for 24 hours. The specimen was then sliced to 0.1mm thickness and chemical polished in aqueous 10%HF-10%H₂O₂ solution, which removed any strained surface layer. The resulting needle was then used for Debye-Scherrer powder photography using Cu K α radiation. An extrapolation of the recorded $\sin^2(\theta)$ values then gave an accurate value of a_α at room temperature. This value, with the thermal expansivities derived from the dilatometer, allowed the ferrite lattice parameter to be calculated through the transformation temperature range.

This has not been entirely successful, but seems to show, for segregated welds the higher $T_s^{\gamma-\alpha}$ and faster initial growth as driving force for ferrite formation is higher. However, as the ferrite grains grow into regions of higher γ -stabiliser and/or lower α -stabiliser content further from the grain boundary, the driving force decreases. The growth rate will also decrease causing a 'plateau' in V_α vs T . On further cooling, the driving force would again increase as does the growth rate, which follows more closely the shape of that of the homogenised weld, fig. 7.10. The segregated weld has a greater proportion of ferrite formed earlier, which would be grain boundary allotriomorphic ferrite.

However, problems still remain and further work on computer modelling of the volume change on transformation is still required. Most of the problems seem to stem from the continuous nature of the temperature change, as a similar analysis for isothermal transformations, chapter 3, gives good agreement.

7.5 Conclusions and Further Work

$T_s^{\gamma-\alpha}$ is associated with nucleation of allotriomorphic ferrite at austenite grain boundaries and segregation in those regions exerts a strong influence, increasing $T_s^{\gamma-\alpha}$ by up to 40°C depending on alloy content.

The oxygen content of the weld does not affect the value of $T_s^{\gamma-\alpha}$, i.e. no evidence was found for the oxygen effect at these [O] levels, which did not appear to affect the austenite grain size.

Segregation in welds leads to earlier nucleation and a higher volume fraction of grain boundary allotriomorphic ferrite than expected on bulk composition.

Further work could be done at higher [O] to observe the effect there, where grain boundary pinning by inclusions could be more effective. Although a full series of tests could not be completed, initial studies have been performed on a higher oxygen weld and corresponding pure alloy, Table VII.5. As reaustenitisation was carried out at a fixed temperature, a greater influence of inclusions in the weld metal upon austenite grain size was noted. A reaustenitisation treatment of 1000°C for 10 minutes was used for the weld metal, but, to ensure the same grain size, 10 minutes at 970°C was needed for the pure alloy. Fig. 7.11 shows the CCT curves obtained, the first two points for the pure alloy resulted from reaustenitisation at 1000°C and show the effect of larger grain size in depressing $T_s^{\gamma-\alpha}$. These CCT curves illustrate the same points as those for the lower-oxygen weld metal/pure alloy combinations, namely:

(i) Negligible difference between the homogenised weld metal and the pure alloy is noted, i.e. no oxygen effect is seen at this oxygen level either.

(ii) A much larger difference in $T_s^{\gamma-\alpha}$ occurs between segregated and homogenised weld metal specimens.

The effect of segregation on grain size has not been studied and so grain size measurements should be repeated on segregated specimens, which should also be linked to quantitative measurements of the degree of segregation. Only a small amount of quantitative EDS was performed on these specimens, fig. 7.12, which indicated a large decrease in the degree of segregation after homogenisation at 1200°C for 3 days. The degree of segregation should also be related to total alloy content and $T_s^{\gamma-\alpha}$ so that the predictive program ⁽⁸⁾ can be modified to suitably account for it.

Table VII.1. Compositions, in wt.%, of welds (W1-3) and pure alloys (P1-3). The concentrations of oxygen and nitrogen are given in parts per million by weight.

| No. | C | Si | Mn | Al | S | P | O | N |
|-----|------|------|------|--------|--------|--------|-----|-----|
| W1 | 0.10 | 0.19 | 1.10 | 0.015 | 0.012 | 0.015 | 188 | 115 |
| W2 | 0.11 | 0.25 | 1.57 | 0.012 | 0.012 | 0.018 | 196 | 57 |
| W3 | 0.14 | 0.22 | 1.81 | 0.012 | 0.013 | 0.030 | 138 | 107 |
| P1 | 0.10 | 0.18 | 1.09 | <0.001 | <0.001 | <0.001 | <10 | <10 |
| P2 | 0.11 | 0.22 | 1.56 | <0.001 | <0.001 | <0.001 | <10 | <10 |
| P3 | 0.09 | 0.25 | 1.82 | <0.001 | <0.001 | <0.001 | <10 | <10 |

Table VII.2. Cooling rates used to derive CCT curves.

| Program Time (mins) | Actual Cooling Rate (°Cmin ⁻¹) |
|---------------------|--|
| 7 | 422.1-426.8 |
| 8 | 371.1-373.5 |
| 9 | 322.6-332.9 |
| 10 | 296.4-300.0 |
| 12 | 247.1-251.0 |
| 15 | 197.1-198.4 |
| 18 | 161.9-166.7 |
| 24 | 121.6-126.6 |
| 36 | 81.4- 83.3 |
| 72 | 40.6- 41.9 |
| 144 | 19.8- 22.1 |

Table VII.3. Welding parameters.

| | |
|-----------------------|--|
| Joint Geometry | ISO 2560 (24 runs in 8 layers of 3) |
| Welding Speed | 2mms ⁻¹ |
| Welding Voltage | 23V(DC+) |
| Welding Current | 180A |
| Interpass Temperature | 250°C |

Table VII.4. Austenite grain size (i.e., mean lineal intercept) obtained after austenitisation at 1000°C for 10 min.

| Specimen | Lineal intercept, µm |
|----------|----------------------|
| W1 | 27 |
| W2 | 42 |
| W3 | 17 |
| P1 | 22 |
| P2 | 20 |
| P3 | 21 |

Table VII.5. High oxygen weld composition (wt%, except [O] ppm).

| | C | Mn | Si | O |
|-----------|------|------|------|-----|
| Weld W104 | 0.10 | 1.31 | 0.58 | 530 |
| Weld W103 | 0.09 | 1.29 | 0.62 | 530 |
| Alloy A | 0.10 | 1.30 | 0.59 | <10 |
| Alloy B | 0.10 | 1.27 | 0.61 | <10 |

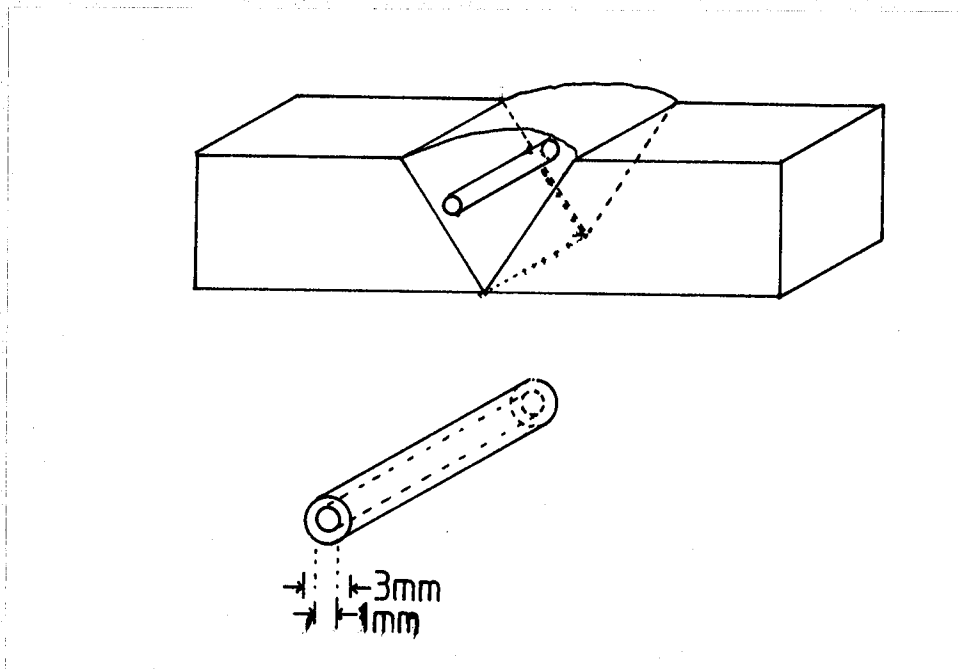


Figure 7.1. Dilatometric specimen preparation.

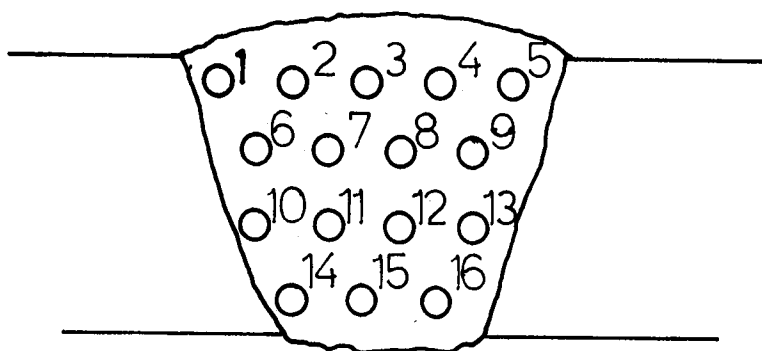


Figure 7.2. Specimen identification with respect to weld macrostructure.

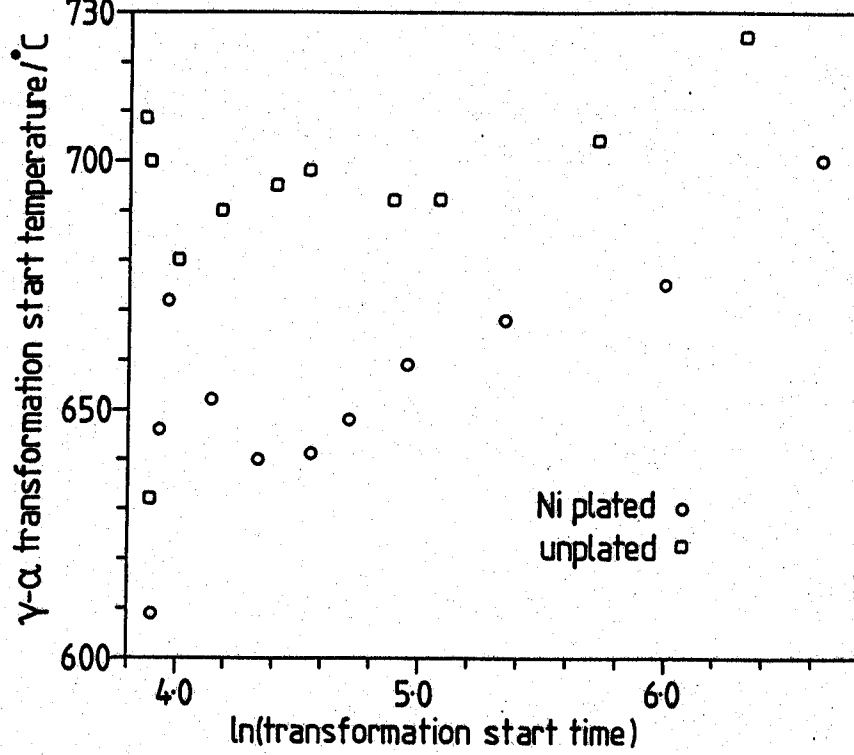


Figure 7.3. $T_s^{\gamma-\alpha}$ over a range of cooling rates for nickel plated and non-plated specimens.

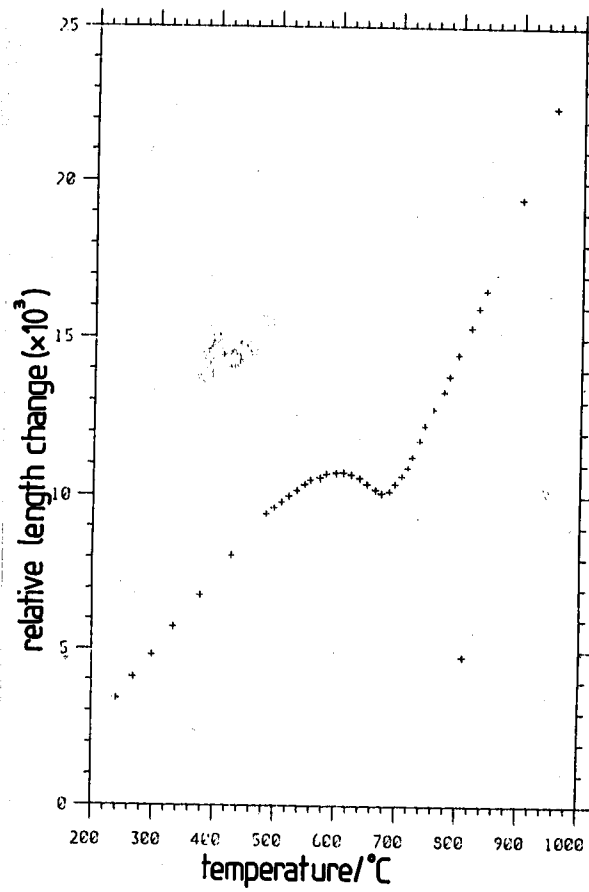


Figure 7.4. $\Delta L/L_0$ versus temperature plot.

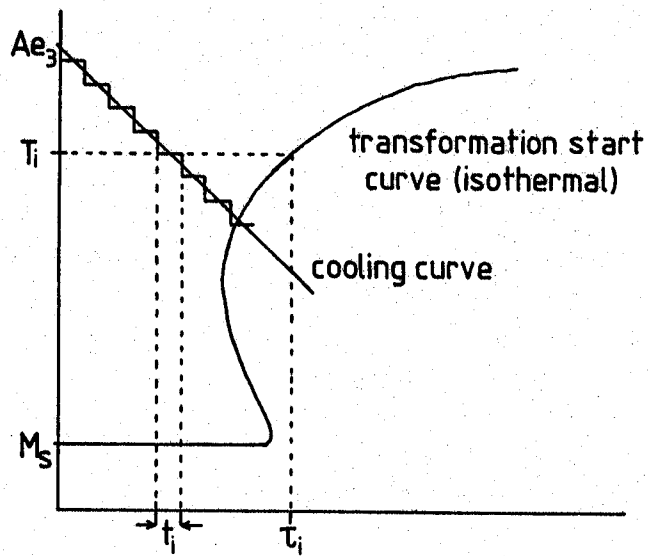


Figure 7.5. The addition rule approach to predict the start of transformation.

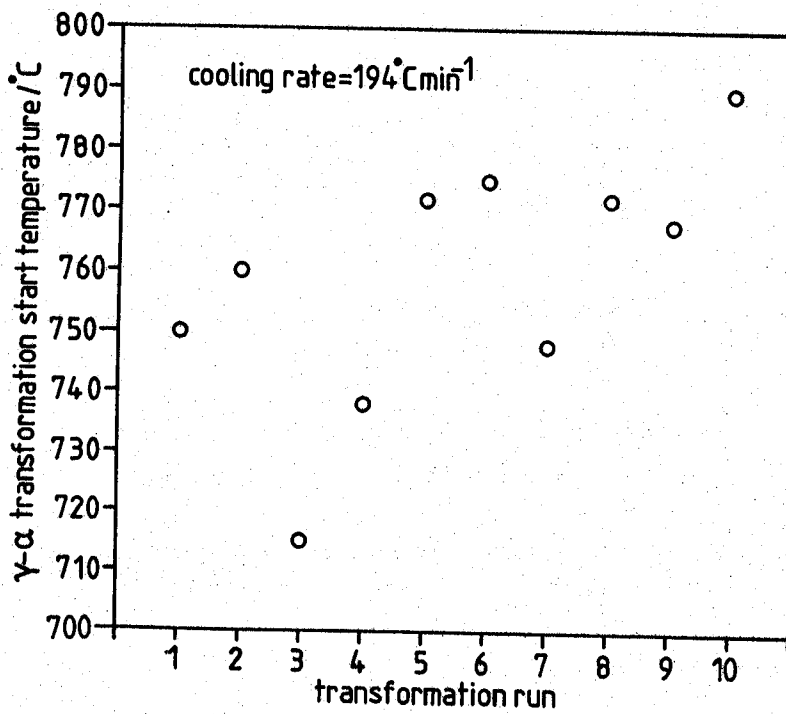


Figure 7.6. Variation of $T_s^{\gamma-\alpha}$ with repeated cycling.

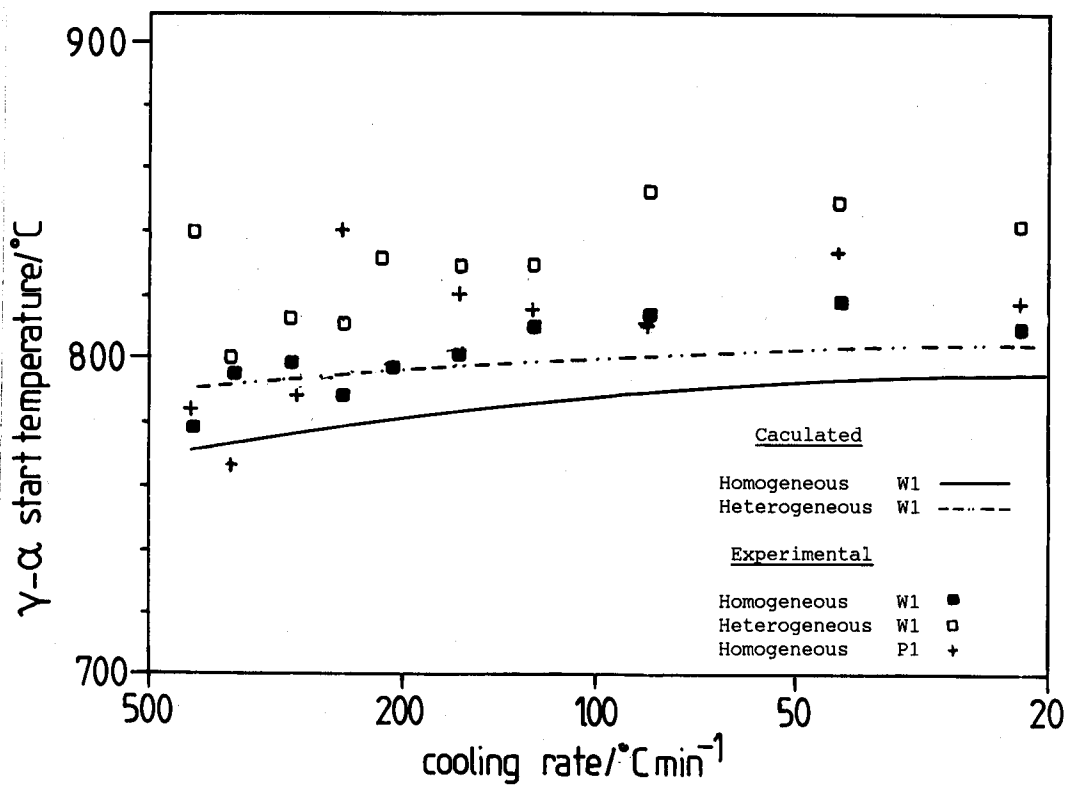


Figure 7.7(a).

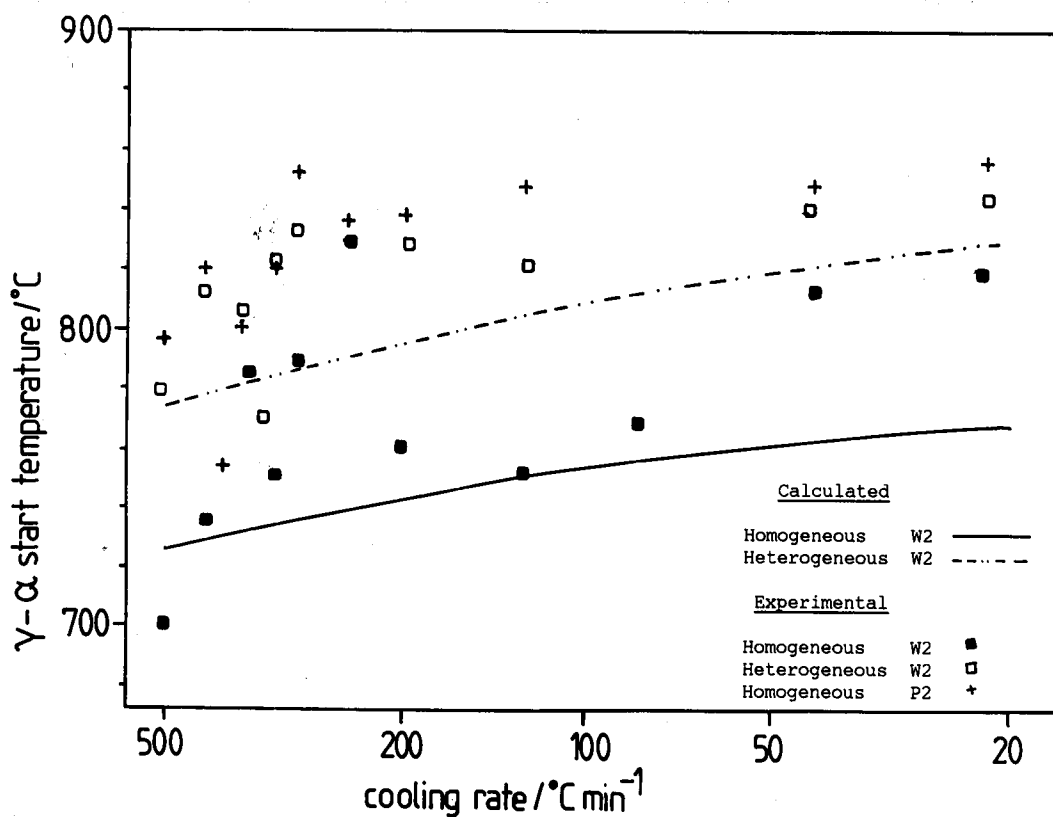


Figure 7.7(b).

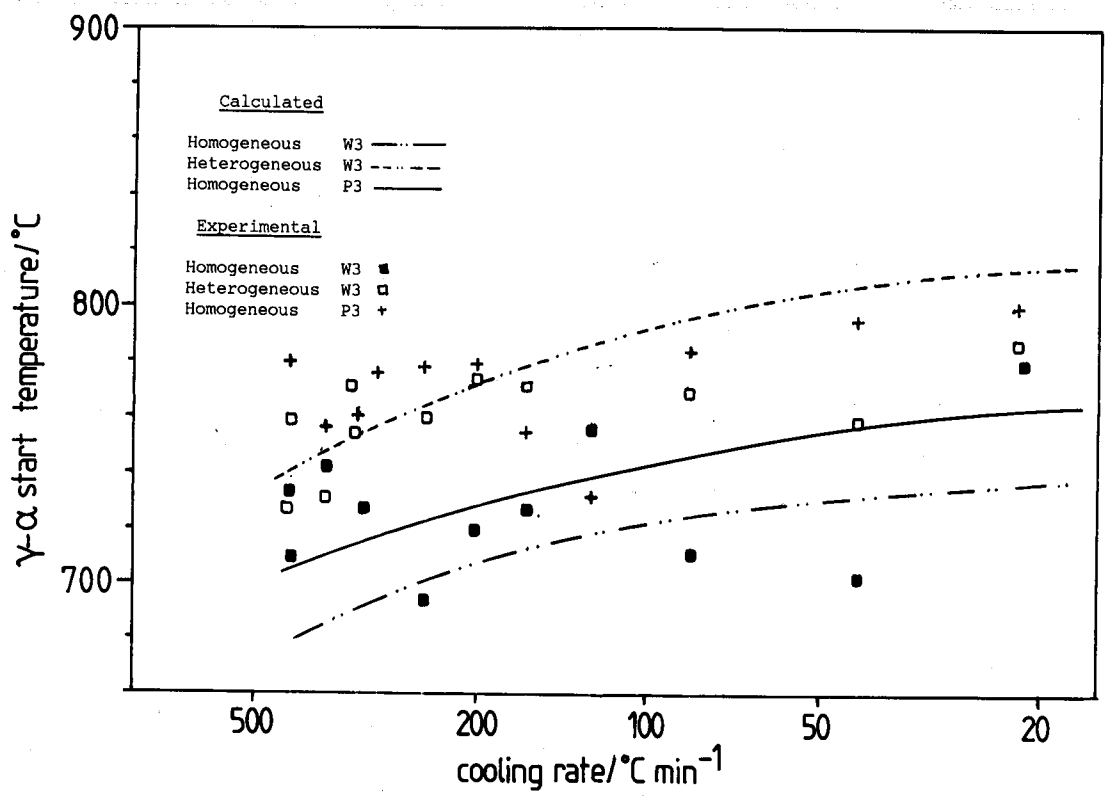


Figure 7.7(c). CCT curves for pure alloys, segregated and homogenised welds.

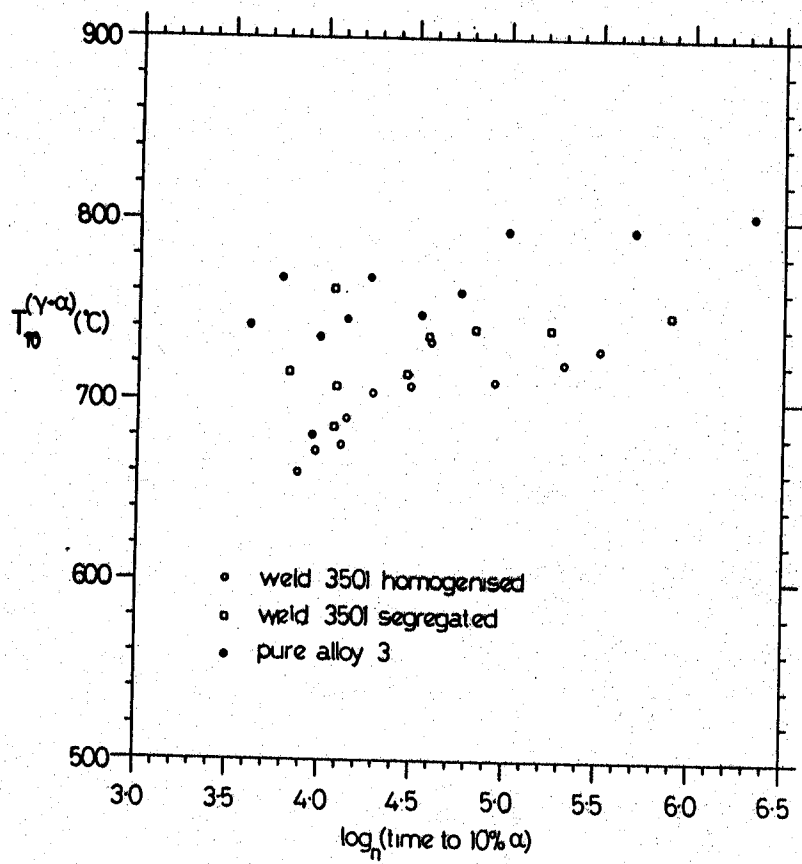


Figure 7.8(a).

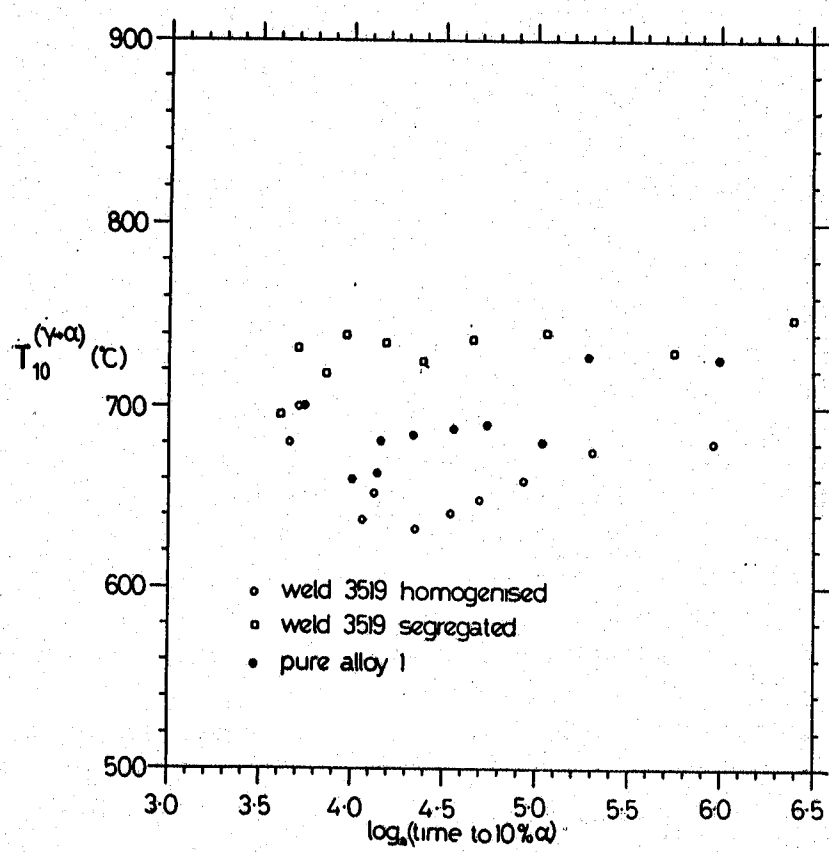


Figure 7.8(b). CCT curves for 10% transformation to ferrite.

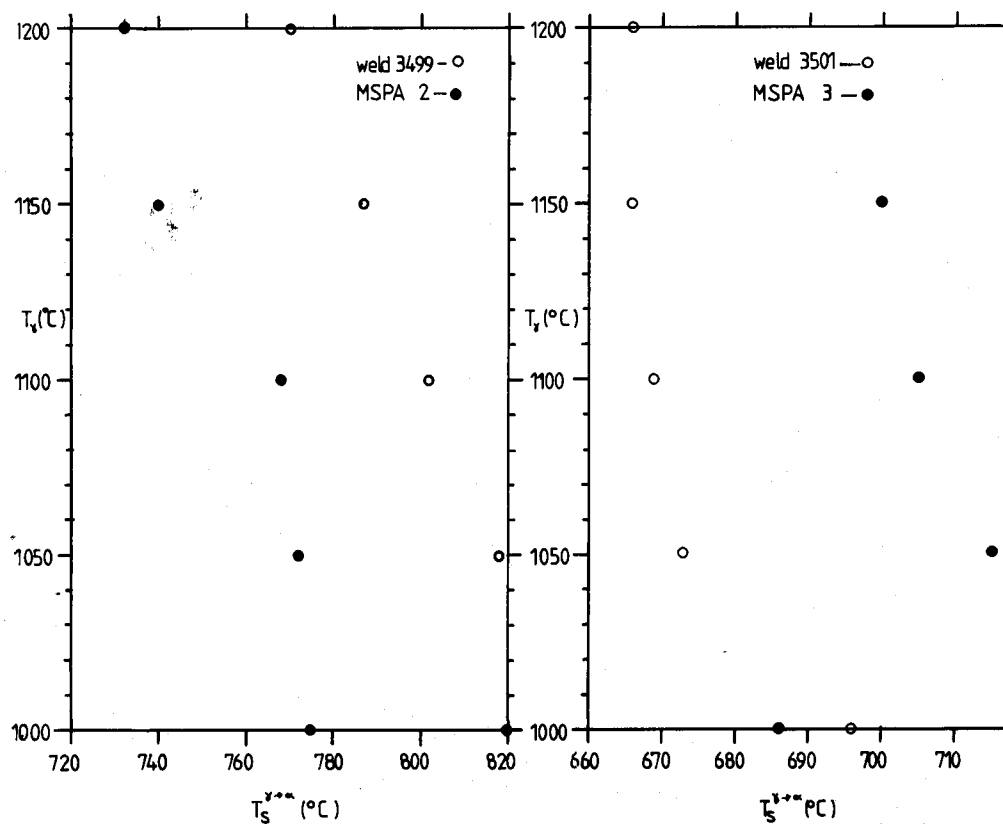


Figure 7.9(a) & (b).

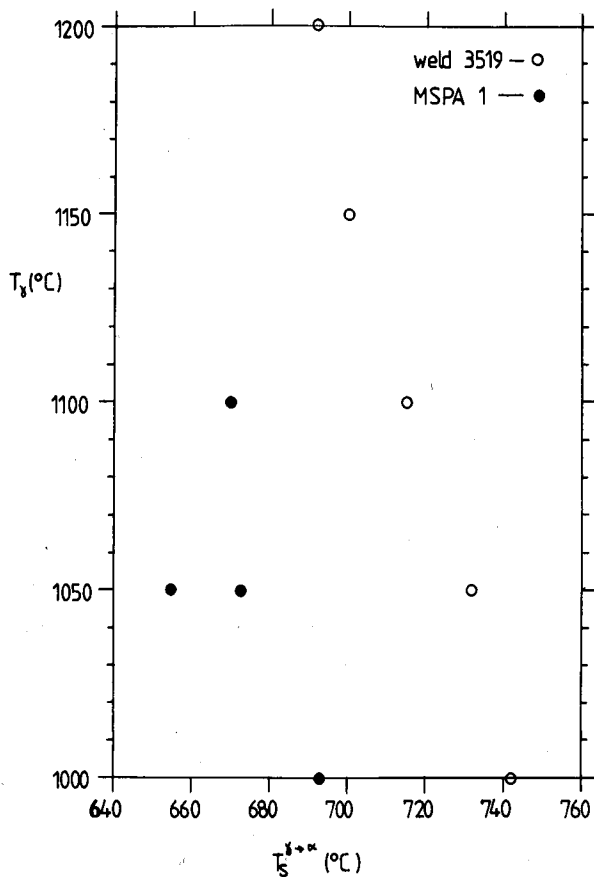


Figure 7.9(c). Variation of $T_s^{\gamma-\alpha}$ with re-austenitising temperature.

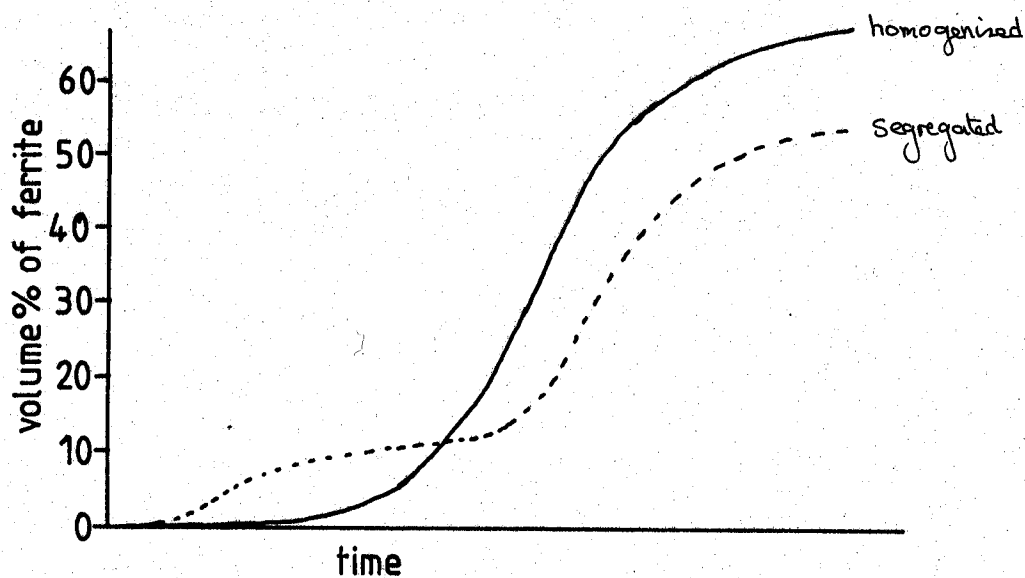


Figure 7.10. Schematic plot of volume fraction of ferrite versus time for segregated and homogenised weld specimens.

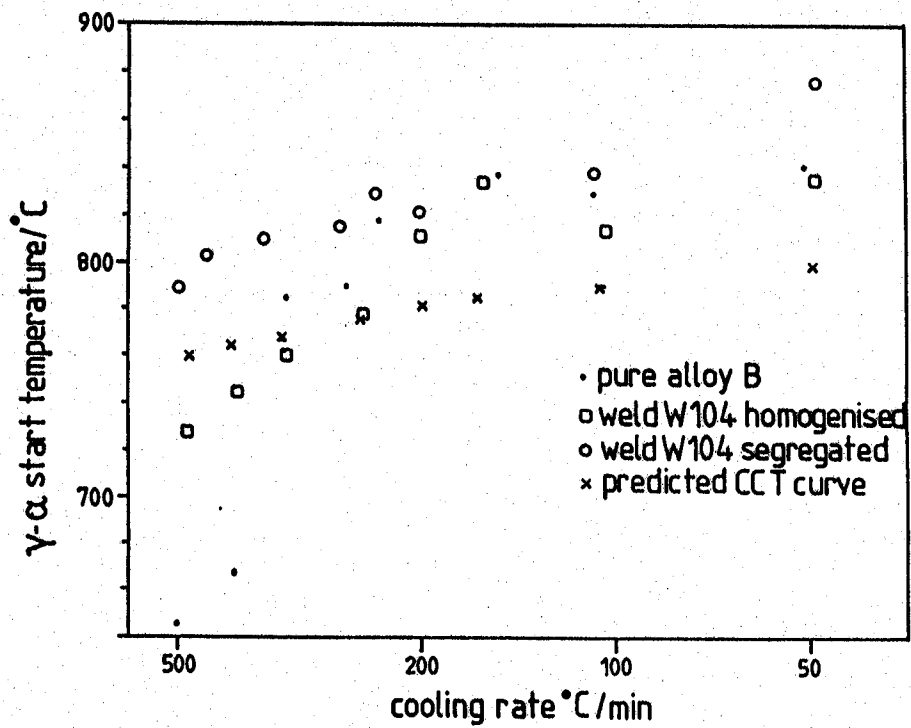


Figure 7.11. CCT curves for homogenised and segregated high oxygen welds and corresponding pure alloy.

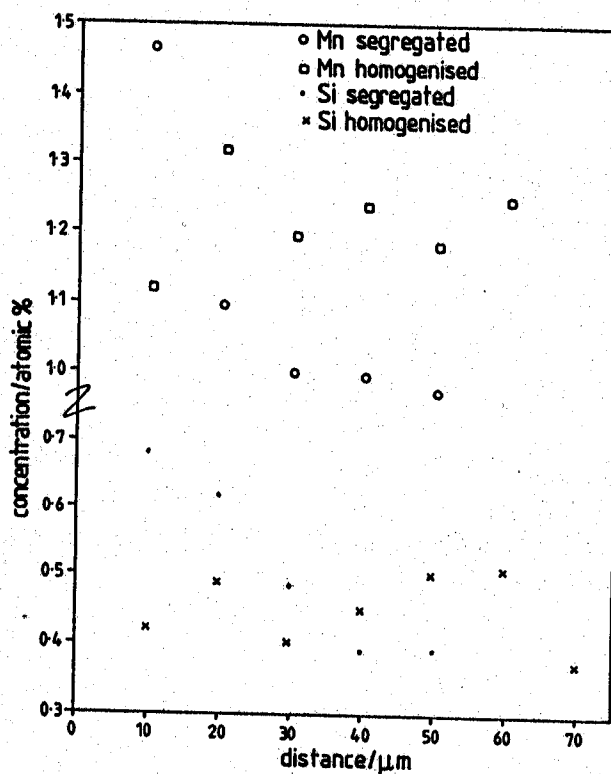


Figure 7.12. EDS traces of as-deposited and homogenised weld metal.

8. Nucleation Events at Inclusion/Steel Interfaces

8.1 Introduction

Although the presence of inclusions has been shown not to significantly affect the initial γ - α transformation start temperature, they are still important in the formation of α_{acic} . This phase was shown to be intragranular nucleated bainite in chapter 4 and so its presence is associated with the availability of preferential nucleation sites within the γ grain interiors compared with the grain boundaries and interfaces. The analysis of Barritte ⁽⁵⁷⁾ indicates that, for the same driving force, large inclusions are energetically more favourable nucleation sites than smaller ones, but are still less favourable than flat (infinite radius) interfaces. This treatment assumed the inclusions to be hard, inert, non-deformable spheres and fairly homogeneous, which is not the general case for weld metal inclusions. As indicated in chapter 6, a substantial effort has been made to determine the mechanism of nucleation of acicular ferrite on oxide inclusions. Trends in nucleation behaviour, taken as being related to the proportion of α_{acic} in the final weld microstructure, with e.g. inclusion composition, have generally been investigated by observation of inclusions in welds fabricated using baseplate, wire or flux composition variations. This approach may be valid for the designer of an electrode as the flux constituents go through many extreme changes en route from electrode to weld; however it has little to offer the materials scientist in deducing nucleation mechanisms. This approach reveals the role of inclusions under welding conditions, but the inclusions themselves and their environment are very difficult to accurately model or control. For instance, if an acicular ferrite plate is found to have nucleated upon a certain particle, then that particle probably consists of several phases e.g. Al_2O_3 , TiO_2 and Cu_xS and it is not possible in that case to identify which of these phases, if any, is responsible for the enhanced nucleation. The fine scale ($\leq 1\mu\text{m}$) of most nucleating particles means that examination must take place in a high resolution SEM or TEM and should sample a statistically significant number of particles in order to chart compositional variations and their effects. The numbers of particles studied in previous reports are of the order of 10-40, which are insufficient to reveal the major trends in nucleation behaviour. Due to this fact, a plethora of theories abound for the controlling mechanism in nucleation of α_{acic} , of which the main ones are (chapter 6):

- (i) Inert surface ^(65,260).
- (ii) Thermal strain/dislocation punching ^(275,276).

(iii) Lattice matching ^(257,258).

(iv) Substitutional alloying element heterogeneities due to inclusion formation ⁽¹¹³⁾.

It is necessary therefore, in order to model the formation of α_{acic} , to be able to determine which of these mechanisms, if any, is operative and under what conditions. In view of the lack of success of the 'trial weld' approach and its time consuming nature, it was decided that a new method of studying the effect of an inclusion/steel interface was required, where the conditions pertaining at the interface were accurately known and controllable. This chapter describes the method and initial trials to prove its viability; in the next chapter the work is extended to cover possible α_{acic} nucleation mechanisms.

8.2 Inclusion Nucleation TEsting Rig (INTER)

In order to determine the efficiency of a particular inclusion phase for ferrite nucleation, that phase e.g. SiO_2 , Al_2O_3 or TiO_2 was obtained as a pure (99.9%+) powder. The next step was to devise a method of simulating the γ - α transformation under known conditions, but similar to those that exist in a cooling weldment. The apparatus finally chosen was a diffusion bonding rig (fig. 8.1), which became INTER, with the following experimental procedure.

High hardenability steel specimens were obtained as 10mm diameter rods and homogenised by sealing in a quartz tube under a partial pressure of argon and heating for 3 days at 1200°C. This treatment removes microsegregation of substitutional alloying elements introduced in drawing to rod. The homogenised rod was then cut into 10mm lengths, the fresh cut ends being ground to a standard finish on 1200 grit silicon carbide paper. A Pt/Pt-10%Rh thermocouple was spot welded to the surface of one of the lengths below a fresh cut and ground end; thus the temperature preset and recorded was that of the interface and not affected by end effects on the radio frequency (RF) coil or by the thermal mass of the rams. A fresh cut surface was used for the interface to avoid any decarburisation that may have occurred during the homogenisation treatment. After a final polish and degreasing of the surface (with methanol) the ceramic phase was sandwiched between the two lengths, with or without a mild steel washer, and the 'composite' was placed between the rams, with the ceramic in the centre of the RF coil. The chamber was then pumped down to 10^{-6} torr by means of a diffusion pump. The 'composite' was then heated into the austenite range, temperature being actively controlled by the thermocouple, for a set time to ensure complete γ formation. Argon quenching then brought the interface temperature down to that of the isothermal transformation for a set time before quenching to room temperature. During the run a constant load could be applied through the proof ring which had previously been calibrated against a load cell up to 200kg.

In the initial studies a series of silicon based phases were used as the ceramic with a high hardenability chrome steel 4857 (Fe-4.08 Cr-0.30C wt%) (Table VIII.1). Although these phases are not reported to have acted as nucleation sites for α_{acic} , they were readily available for testing the procedure, offering a range of thermal and chemical properties, which, with varying load,

could be used to investigate the effect of thermal strain.

8.3 Silicon Phases

8.3.1 Comparison of Si, SiC, Si₃N₄ and SiO₂

Fig. 8.2 shows optical micrographs from the first comparative study on these silicon based inclusions, which were performed using an isothermal treatment of 60s at 505°C, following reaustenitisation at 900°C for 1 to 10mins. The RF coil gave rapid heating to $\approx 700^\circ\text{C}$, but the heating rate decreased drastically above 800°C so that the heating cycle typically lasted around 2.5mins. Heat transfer was limited by generator power and coil-specimen separation; the latter was reduced to the minimum value, which still allowed the specimen to be set up and would not cause the specimen to touch the coil if it barrelled or crept during the heat treatment. This would have caused severe damage to the controlling electronics. At 900°C the temperature fluctuation was maintained below $\pm 5^\circ\text{C}$, due mainly to a slight time lag in the temperature control circuit and through the increased thermal contact with the rams on loading. The load was applied at the start of the reaustenitisation treatment, applied until the completion of the isothermal treatment and removed during the quench to room temperature. After reaustenitisation the specimen was argon quenched to the isothermal treatment temperature. Because of the large volume of the chamber the quench rate was fairly slow, taking around 100s to reach 505°C, at this temperature the fluctuation was less than $\pm 3^\circ\text{C}$, often as low as $\pm 1^\circ\text{C}$. The quench rate was insufficient to take the specimen into the bainitic region before grain boundary nucleation occurred, which restricts its application in studying the nucleation of α_{acic} . It is fast enough to avoid the ferrite nose at 640°C and 60s. The TTT curve also predicts an incubation time (to around 5% transformation) of 40 minutes at 505°C, fig. 8.3. After transformation the specimens were sectioned vertically along their mid-plane, this avoided any surface effects due to carbon loss during the heat treatment, which would have promoted ferrite formation. The microstructure of 4857 away from the interface was martensitic with no grain boundary ferrite and this microstructure continued right up to the ceramic for SiO₂ and Si₃N₄ indicating no ferrite nucleation behaviour for these phases. The interface region for SiC and Si is very different with the microstructure being characterised by several layers (fig. 8.4).

- (i) Along the original interface line, particles of the ceramic powder still remain.
 - (ii) Next follows a layer of ferrite, which appears to be a single grain. In the case of SiC this ferrite has a series of precipitates in it, which are spherical and banded, roughly 0.1 μm in diameter and with a spacing of 0.3 μm .
 - (iii) A precipitate free zone (PFZ) for SiC.
 - (iv) A layer of chromium/iron carbides developing at the ferrite/martensite interface.
- The nucleated ferrite was characterised by microhardness traces and that for SiC is shown in

fig. 8.5 indicating the exceptional hardness imparted to the ferrite by the precipitates; $\approx 700\text{VDN}$ compared with 350VDN for the PFZ and 240VDN for the carbides. Similar results were recorded for 4857/Si, but there was very little change in hardness in the steel up to the ceramic for the nitride and oxide.

The development of the ferrite layers with the 4857/SiC system was further investigated by a series of isothermal treatments at 505°C (Table VIII.2), under a pressure of 12.5MPa after reaustenitisation at 900°C for 1 minute. The relatively long heating and quenching times allow full reaustenitisation of the specimen, but also allow some γ - α transformation to occur at the steel/ceramic interface during cooling. This last point is illustrated in fig. 8.6, which shows the 4857/SiC interface region for a specimen that was argon quenched directly to room temperature after reaustenitisation. The ferritic layer that has formed in the direct quench is between 4 and $20\mu\text{m}$ thick and exhibits a thickness variation along the surface of remenant particles of SiC. The variation in thickness of the ferrite corresponds to an undulation in the surface of the remaining particles of SiC and an extension of the PFZ to the particle in the ferrite above the peaks, fig. 8.7. The peaks on the particle surface correspond to the minimum thickness of ferrite. The thinner areas of ferrite are generally associated with a greater amount of carbide formation at the ferrite/martensite interface, which arises from greater carbon redistribution into these areas compared to the thicker ferritic regions.

This behaviour is repeated for the specimens with isothermal holds at 505°C . After 10s at 505°C , the plateaus on the particle surface corresponding to minimum ferrite thickness are of reduced extent, with ferrite developing to between 4.8 and $16\mu\text{m}$, fig. 8.8. On some remaining SiC particles the thickness of ferrite is fairly uniform, but a central SiC peak persists with an extended PFZ, fig. 8.9.

The ferrite thickness formed after 30s at 505°C is 10 - $34\mu\text{m}$ with the thickness along a single SiC/4857 interface now being more uniform than at shorter times, fig. 8.10. The undulations in the surface of remaining SiC particles are much less pronounced and this is accompanied by the PFZ being confined to the α /martensite interface. The PFZ does not extend down to the SiC even when a prominent peak is retained, fig. 8.11. The other heat treatment, 45s at 505°C , resulted in a decrease in the ferrite thickness developed compared to the previous specimen. This was probably due to a shorter heating cycle as the quenching times were both around 80s. The ferrite thickness varied between 10 and $14\mu\text{m}$ and was associated with the return of undulating particle surface and the PFZ extending down to the SiC, fig. 8.12.

The variations in interface morphology and PFZ distribution are therefore dependent upon the amount of ferrite formed, which generally increases with increased isothermal holding time as shown in fig. 8.13.

Once formed, the ferrite allotriomorphs and their precipitates are stable to further aging. A 4857/SiC couple was prepared by reaustenitising at 900°C for 1 minute, quenching to 505°C for

VDN=Vickers diamond number, also used is H_V . $\text{VDN} \equiv \text{kgmm}^{-2}$.

60s, then quenching to room temperature. Subsequent aging of this specimen at 505°C for 22.5 hours did not result in any change in the ferrite allotriomorphs or in the PFZ, only in tempering of the martensitic 4857. Hence, the ferrite and precipitate structure is thermally stable in the ferrite regime and would require heating into the austenite region to remove the PFZ, which may also cause further ferrite formation, but this point was not investigated further.

8.3.2 Chemical Analysis

The amount of ferrite developed e.g. $\approx 40\mu\text{m}$ width of which $\approx 5\mu\text{m}$ is the PFZ after 60s at 505°C, and variations in the SiC/ α interface are incompatible with the small energy changes introduced by lattice matching, thermal strain or inert surface. This suggests that a chemical effect is at work.

In order to investigate the chemical nature of this effect, EDS analysis - again performed on an ISI-100A SEM - was made across the interface and the resulting traces for all four combinations are presented in figs 8.5, 8.14-16, along with the corresponding hardness traces. In the cases where ferrite formation had taken place, the ferrite layer was found to have a substantially higher concentration of silicon, 20-25at% in the precipitated layer, steadily falling through the PFZ (5-10at%) to be negligible in the carbide layer and martensite. The variation in Fe and Cr levels show a decrease in relative terms in the ferrite, which is consistent with increased [Si], but no change in Fe or Cr. The corresponding analyses for Si_3N_4 indicated no enrichment in Si in the steel as did results for SiO_2 , but the thin nature of the layer led to some beam overlap with the surrounding steel and so quantitative results could not be obtained for this system.

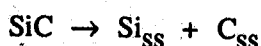
These results indicate that the nucleation of ferrite is linked to dramatic increases in the silicon level of the steel introduced from the ceramic. The Fe-Si binary phase diagram predicts, at these silicon levels (20-25at%), the presence of Fe_3Si or FeSi precipitates. The volume fraction of precipitates observed is around 50% and this would suggest FeSi as Fe_3Si precipitation would give rise to 100% precipitates. However, the absence of any precipitates in the case of 4857/Si draws this conclusion into question as similar [Si] was achieved. It is also possible that for the 4857/Si system the whole of the 'ferrite' may be a single allotriomorph of ordered Fe_3Si . TEM studies of the interface regions were difficult. Often, the bond broke during machining to discs and foil preparation was hampered by the large variations in properties of the layers constituting the interface region. Ion beam thinning methods perforated the disc unevenly and introduced large amounts of damage, whereas jet polishing resulted in etching away of the steel before the precipitated ferrite or ceramic were thin enough to be transparent to electrons. Some thin area around the interface for a 4857/SiC couple (900°C/10mins then 700°C/120s) ^{was seen,} fig. 8.17, which exhibits some precipitate-like structures. Closer inspection, fig. 8.18, reveals a series of roughly spherical particles, of the order of $0.1\mu\text{m}$ in diameter spaced about $0.2\text{-}0.3\mu\text{m}$ apart and banded. These regions were thin enough to allow selected area diffraction patterns (SADP) to be obtained from both the particle and surrounding matrix, fig. 8.18. Indexing of these SADPs shows the

strong diffraction arising from the ferrite and also spots consistent with $\text{Fe}_8\text{Si}_2\text{C}$. None of the other possible precipitates, e.g. FeSi , Fe_3Si , FeSiC , could account for the observed patterns. In order to check the identity of the precipitates the bonds were broken open and X-ray diffractometry carried out on the reacted interlayer to deduce the precipitate phases present. The possible precipitates are limited to those containing Fe, Si and C as these were the only elements detected. EDS techniques were unable to detect carbon as a windowless detector was not available and the accuracy of such devices is open to question at low concentrations. The presence of more carbide with SiC than for Si suggests that in addition to silicon, carbon is also being released into the steel and so there may still be a substantial carbon content in the precipitates in the ferritic region.

The X-ray diffraction results give diffraction peaks for 4857/SiC corresponding to iron silicon carbides (FeSiC and $\text{Fe}_8\text{Si}_2\text{C}$), fig. 8.19, but no consistent iron silicide phases can account for the peaks observed. Other peaks were ascribed to $(\text{Fe,Cr})_7\text{C}_3$ and ferrite, only the ferrite peaks were observed for 4857/Si. Therefore the absence of precipitates in the case of Si is due to the lack of any carbon enrichment whose greater activity in steel compared with silicon causes precipitation to occur more readily. The much slower (substitutional) diffusion of silicon may also slow the kinetics of precipitation so that iron silicides do not form during the quench to room temperature; the precipitation is, however, seen to be ancillary to the dissolution in the promotion of ferrite formation.

If dissolution does, in fact, take place during the heat treatment, then it should be possible, by extending the treatment, to fully dissolve the ceramic interlayer. Therefore, for a 4857/SiC couple, the austenitisation treatment was extended to 10mins at 900°C followed by 2mins at 720°C in an attempt to show this. The resulting interface structure is illustrated in fig. 8.20. None of the original SiC is retained, having all dissolved to give very large allotriomorphs of ferrite, again illustrating precipitation, along with a PFZ of greater extent both relatively and in real terms. The much larger release of carbon into the steel has caused the formation of copious 'fans' of (Fe, Cr) carbides emanating from the α /martensite boundary.

The nucleation can now be determined as the dissolution of SiC into the steel by the reaction:



The subscript ss refers to solid solution within the steel.

The corresponding reaction for silicon would be identical except for the omission of carbon. However, it is not known which phase, α or γ , the ceramic dissolves in, although the low solubility of carbon in ferrite suggests that dissolution in this phase is unlikely.

8.3.3 Temperature of Dissolution

In order to ascertain the temperature of dissolution, i.e. which phase the ceramic dissolves in, a further run was carried out using 4857/SiC that did not heat the steel into the austenitic region. This specimen was heated to 500°C and held for 10mins under a bonding pressure of 12.5MPa before quenching to room temperature. The resulting microstructure (fig. 8.21) shows no

preferential nucleation of ferrite or any change in the original SiC powder, although in the bulk of the sample tempering of the starting martensitic microstructure has taken place with grain boundary nucleation of ferrite. Microhardness and microanalytical traces, fig. 8.22, confirm the lack of any reaction of the ceramic with little variation in hardness - in the same phase - up to the ceramic. In addition, no enrichment of the interface region in Si is noted and so it seems that the dissolution is a thermally activated process.

8.3.4 Mechanism of Dissolution

The proposed mechanism for enhanced ferrite formation at steel/SiC interfaces is summarised in fig. 8.23. The initial solution consists of a sharp interface and step functions in the Si and C concentration profiles at the interface. During the re-austenitisation treatment, sufficient activation energy is supplied to allow the initial dissolution of the ceramic. This will commence at certain high energy sites in the ceramic, possibly grain boundaries, the regions between them remaining as flat plateaus, as observed in the continuously quenched specimen, fig. 8.24. As the ceramic passes into solid solution in the steel, equilibrium at the steel/ceramic interface is most likely established, with both Si and C diffusing away from the interface, fig. 8.23(b). Variation of isothermal treatment time at 505°C, section 8.2.1, revealed that longer holding times caused further changes in the ceramic, the heating, re-austenitisation and quenching times for these specimens being similar. Hence, the dissolution of the ceramic must continue at temperatures below 900°C and probably at 505°C. The highest energy sites now are the edges of the plateaus, whose small radius of curvature cause them to dissolve most readily, reducing the extent of the plateaus, fig. 8.24(b). Fig. 8.24 also shows the contours of different Si and C levels in the steel due to diffusion away from the ceramic.

Eventually, either during the quench to room temperature or after a certain incubation time, ferrite forms, initially at the interface between the steel and remnant SiC. This has the highest [Si] and so is most favourable for ferrite formation as it has lowest hardenability. The α/γ interface then sweeps out as a single entity from the remnant SiC/steel boundary through the Si enriched γ , partitioning carbon into the γ ahead of it. The movement of the α/γ interface as a whole, but single entity gives rise to the single allotriomorph observed. This also suggests that the conditions pertaining at the interface are the same along its whole surface, so that ferrite formation occurs at all points simultaneously. The peak of partitioned carbon ahead of the advancing α/γ interface is sufficient to cause precipitation of (Fe,Si) carbides on the interface. Immediately after precipitation of carbides, the Si and C levels fall and so precipitation does not occur until these rise again resulting in the banded appearance observed. The level of [Si] is also important as witnessed by the PFZ at low Si levels. The extension of the PFZ to the ceramic above the peaks and plateaus for short isothermal holds is due to low [Si] resulting from the small amount of dissolution that has occurred at these sites. After longer isothermal holds, more dissolution and lateral diffusion of Si may have taken place to reduce composition variations within the eventual ferrite allotriomorph. SiC peaks in these specimens, are bordered by regions

suffering high degrees of dissolution and so the overall Si level is high. Once the α/γ interface reaches the limit of the Si enriched area, it stops, but the carbon partitioning ahead of the interface is still present and this partitions to a greater extent into the γ regions adjacent to a peak or plateau, fig. 8.24(c). This results in greater carbide precipitation in the latter regions, as observed in figs 8.6-8.12. The formation of (Fe,Cr) carbides may be inhibited by the presence of Si within the allotriomorph and so as [Si] falls towards the periphery, the partitioned carbon causes carbide precipitation ahead of the α/γ interface. The (Fe,Cr) carbides then prevent Si diffusion out of the allotriomorph and effectively forms a barrier to further ferrite formation. This is consistent with the lack of variation in the allotriomorphs with tempering at 500°C.

8.3.5 Use of Austenitic Steel

In an attempt to investigate possible inclusion effects upon the nucleation of martensitic phases in steel a fully austenitic steel 4863 (Fe-0.31 C-30.5 Ni wt%) was substituted for 4857 and interfaced with SiC. The specimen was 'reaustenitised' at 900°C for 10mins under a pressure of 12.5MPa to produce a strong intimate ceramic/steel interface for later quenching studies. The specimen was quenched directly to room temperature with no intermediate isothermal stage as no $\gamma\text{-}\alpha$ transformation should take place. Optical microscopy, however, revealed that the interface region appeared to have undergone a transformation to produce a structure very similar to that observed for the 4857/SiC couple, fig. 8.25. Differences that did exist included the lack of any carbides at the allotriomorph/martensite interface and more easily resolvable precipitates within the ferrite. The precipitates are more clearly defined and are banded parallel to the final allotriomorph/ γ interface as though they marked successive positions of that interface, i.e. they are similar to interphase carbide precipitates observed in Nb-Ti-V steels. They are also roughly spherical in shape. X-ray diffraction of the interface layer, fig. 8.27, gave strong peaks for γ and a peak corresponding to $d_{hkl}=2.02\text{\AA}$, which is a strong characteristic peak of the equiatomic silicide FeSi. The absence of $\alpha\text{-Fe}$ peaks in the X-ray diffraction data suggests that a different mechanism operates in this case than that operative for 4857/SiC. The situation is clarified somewhat by the TEM results, such as they are, fig. 8.26. The nature of the precipitates is banded, characteristic of interphase precipitation, within a single allotriomorph emanating from the remanant SiC particle. On indexing the SADP the precipitates are FeSi, but the matrix is $\gamma\text{-Fe}$. The precipitates adopt a cube-on-cube orientation with γ , consistent with their ordered nature. If the precipitates are FeSi and have a volume fraction of $\approx 50\%$, as indicated from the micrographs then, for a total Si level of 20-25at%, there is very little silicon remaining in solid solution. The net effect of SiC dissolution is an increase in the solid solution γ -stabiliser (C) content, making α formation even less favourable thermodynamically. The problem of the single allotriomorphs with their banded precipitate arrays still remains.

The mechanism differs from that operative with 4857/SiC and involves strain/diffusion induced grain boundary motion rather than a $\gamma\text{-}\alpha$ phase transformation. The following mechanism is proposed:

(i) Loading of the specimen causes yielding around asperities and so increases the strain energy in γ around the SiC particles.

(ii) Dissolution of SiC into γ takes place at 900 °C, Si and C diffusing away from the SiC/ γ interface.

(iii) The Si levels are insufficient, with increased carbon levels, to cause ferrite formation, but will further strain the γ lattice.

(iv) On cooling, as the load is still applied and dislocation motion becomes more difficult, grain boundary motion is initiated from the SiC/ γ interface. Grain boundary motion initiation is dependent upon load, temperature and [Si].

(v) As the boundary sweeps through the allotriomorph (silicon enriched γ), FeSi is precipitated at the advancing interface, resulting in the banded appearance. The ordered precipitate, which has a low mismatch with γ , would not be expected to hinder grain boundary motion. In contrast, the removal of Si from solid solution reduces lattice strain and increases the driving force for boundary migration.

(vi) On reaching the limit of Si enrichment the remaining steel has a much reduced lattice strain and so the driving force for migration is decreased and the grain boundary is arrested.

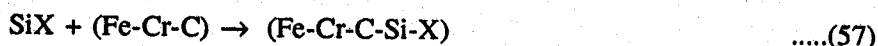
This hypothesis explains the observed features, but insufficient work has been performed on the fully austenitic system to fully verify this.

The change in character and size of the particles is then probably due to a much lower activity of carbon in the austenitic steel and a higher activity for the α -stabilising silicon. The absence of α /martensite interface carbides is probably due to the much weaker carbide forming nature of nickel compared to chromium. In other respects the two processes are very similar indicating the ready dissolution of SiC in steel at 900°C.

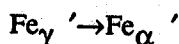
Thermal activation of the process was further demonstrated by the use of a 4863/SiC couple, which was only heated to 505°C for 10mins under an applied pressure of 12.5MPa before quenching to room temperature. As with 4857/SiC for the same heat treatment there was no ferrite formation at the ceramic/steel interface nor was there any enrichment of this region in silicon. This again illustrates the need for a certain amount of thermal activation before chemical reaction occurs between the steel and the ceramic.

8.3.6 Modelling the Dissolution

The different behaviour of the four ceramics studied can be understood by reference to their standard free energies of formation (ΔG_F°). The data in Kubaschewski, Alcock and Evans ⁽²⁷⁹⁾ was used to plot out ΔG_F° as a function of temperature for Si, SiC, Si_3N_4 and SiO_2 , fig. 8.28, for one mole of the product phase. The latter two compounds are considerably more stable than the other two and so would be expected to dissolve much less readily. The reaction can be represented as:



which may be accompanied by:



along with the possible precipitation of iron silicon (X).

The stoichiometric nature of SiC, i.e. its narrow composition range, allows it to be modelled thermodynamically as a line compound, characterised by its standard free energy of formation, ΔG_F , as the SiC used was a pure compound. 4857 is a low alloy steel and its solution free energy could be calculated on the basis of Wagner interaction parameters. However, the recorded levels of Si after heat treatment are too high for the approximations of the Wagner approach to be valid. Specifically the second and higher derivatives in the Taylor series for the logarithm of activity coefficient are non-negligible at high concentrations.

$$\ln f_1(x_2, x_3, x_4, \dots) = \ln f_1^0 + \left[x_1 \frac{\partial \ln f_1}{\partial x_1} + x_2 \frac{\partial \ln f_1}{\partial x_2} + x_3 \frac{\partial \ln f_1}{\partial x_3} + \dots \right] + \left[\frac{1}{2} x_1^2 \frac{\partial^2 \ln f_1}{\partial x_1^2} + x_1 x_2 \frac{\partial^2 \ln f_1}{\partial x_1 \partial x_2} + \dots \right] \quad \text{.....(58)}$$

The Wagner approach only considers the first two terms and so breaks down at solute contents greater than $\approx 5\text{at}\%$. Therefore, the solution free energies of the steel before and after SiC dissolution were calculated from the equation:

$$G_m^\phi = \sum_i x_i G_i^\phi + \sum_i x_i \ln x_i + E_{G_m}^\phi \quad \text{.....(59)}$$

$E_{G_m}^\phi$ = excess free energy of mixing

G_i^ϕ = lattice stability, i.e. free energy difference between component i in its free state and the structural form (phase) ϕ .

The excess free energy of a system represents the deviation from ideal behaviour and incorporates the solute activity coefficient terms. Lattice stabilities for many elements and phases are well known and documented, e.g. the journal Calphad, but the excess free energies are not, especially for ternary and higher systems. Hence, the approximation is made that $E_{G_m}^\phi$ is the sum of the excess free energies of the constituent binaries. This effectively neglects any ternary or higher interactions, but allows calculations to be made, based upon the (known) binary terms.

The initial dissolution step will be the dissolution of a small amount of SiC to increase [Si] and [C] in the adjacent steel by equal amounts. After this, diffusion of C and, to a lesser extent, Si away from the interface can take place. The thermodynamic feasibility can be determined by calculating the free energy change for the process:



Subscript 1=C, 2=Si, 3=Cr. either as α or γ .

This will not fully describe the reaction as free energy will be dissipated in the diffusion of Si and C away from the interface. However, if the free energy change is sufficiently negative, then it is energetically favourable and should proceed, subject to kinetic considerations and the presence

of sufficient thermal activation. The approach adopted was to use a series of combinations of x_{Si} and x_C in the final steel at temperatures between 500 and 900°C to calculate the free energy change for reaction 57. The results for 4857/SiC are presented in fig. 8.29 for both α and γ , between the limits of $x_C=0.0142$ and 0.164 mole fraction and $x_{Si}=0.0$ and 0.30 mole fraction. The curves represent carbon mole fractions of 0.0142 (a), 0.0342 (b), 0.0592 (c), 0.0842 (d), 0.1092 (e), 0.1342 (f), 0.1592 (g) and 0.1642 (h). The results indicate that the dissolution will not take place with α -4857, as was found experimentally, due to the very high free energy of carbon in the BCC lattice.

The reaction is favourable at all temperatures for γ -4857/SiC and so dissolution would proceed at 500°C until ferrite formation ^{took place at the interface,} as long as carbon diffusion away from the steel/SiC interface can take place. This is consistent with the extension of the reaction with longer holding at 505°C.

The free energy of reaction for 4863/SiC, with 4863 as γ , indicate that the dissolution is favourable at low carbon levels at 500°C and at higher carbon levels at higher temperatures, fig. 8.30. Experimental runs at 505°C, however, reveals no dissolution of the carbide. It therefore appears that sufficient thermal activation is necessary to initiate dissolution, which could be linked to the high level of carbon that results locally from the initial dissolution. In the later stages of dissolution carbon can diffuse away from the interface and dissolution does not result in such high carbon levels. Once started, the dissolution can proceed at lower temperatures until the formation of α prevents further carbon release from the ceramic.

The corresponding free energy traces for Si, Si_3N_4 and SiO_2 are presented in figs 8.31 to 8.33. The latter two compounds are simplified as data for the excess free energies of N and O in α and γ are limited. The behaviour of nitrogen is probably similar to that of carbon and the solubility of oxygen in iron in the solid state is limited and so would not favour the dissolution of the oxide. The traces, however, indicate that no reaction is expected for Si_3N_4 and SiO_2 , but is feasible for Si, again consistent with the experimental results.

In the systems for which reaction is feasible and observed to take place, it is possible to calculate the interface equilibrium, the conditions for this being:

$$\mu_1^\gamma = \mu_1^{SiC} \quad \text{.....(61)}$$

μ_1^ϕ = chemical potential of component i in phase ϕ

The absence of any Fe or Cr ingress into the ceramic phase, or only to a negligible, non-detectable amount allows the equilibrium to be restricted to Si and C. In addition, the stoichiometric nature of SiC means that a sufficient relation for equilibrium ⁽²⁸⁰⁾, fig. 8.34, is:

$$\mu_u^{SiC} = v_1^u \mu_1^\gamma + v_2^u \mu_2^\gamma \quad \text{.....(62)}$$

The compound, u, is SiC hence $v_1^u = v_2^u = 0.5$

In this situation, μ_u^{SiC} is merely the molar free energy of this phase and the potentials μ_1^γ and μ_2^γ are the partial derivatives:

$$\frac{\partial G_m^\gamma}{\partial x_C} = \frac{\partial G_m^\gamma}{\partial x_{Si}} \quad \text{.....(63)}$$

G_m^γ is again calculated on the basis of equation 59 and for variation of Si and C only:

$$x_{Cr} = Y_{Cr} x_{Fe} \quad \text{.....(64)}$$

$$x_{Fe} = (1 - x_C - x_{Si}) / (1 + Y_{Cr}) \quad \text{.....(65)}$$

Y_{Cr} = constant as there is no sizeable change in the iron-chromium ratio in the steel during heat treatment. Partial differentiation of equation 59 with respect to x_1 (C) and x_2 (Si) and iteration leads to a solution of equation 61, giving the interface concentrations of Si and C in 4857 at the interface with SiC. These are presented in Table VIII.3. Away from the interface, the composition of the steel will adjust itself to maximise the free energy decrease with respect to the starting 4857. This was also calculated during the calculation of the free energy of reaction for dissolution and the resulting values presented in Table VIII.4. These agree very well with the final Si levels recorded by EDS, although some Si and C will be tied up in the precipitates.

The effect of silicon in solid solution is to decrease hardenability, so accelerating the formation of ferrite and hence must more than compensate for the effect of increased carbon released from SiC in increasing hardenability. The reaction and release of silicon gives rise to the concept of *chemically active inclusions*, which can be defined as those which influence the microstructural stability of a material by reaction with it so that the chemistry local to the inclusion is altered. This mechanism is different from that of chemical heterogeneities induced by the formation of the inclusion as the inclusion is already present and subsequently reacts in the solid state; the former effect would be removed by fluid flow in a weld pool.

8.4 Cobalt Phases

Having identified one species of chemically active inclusions (CAI) other ceramic phases were investigated to see if similar behaviour existed for other compounds. Compounds of elements such as Mn, Ni, Ti, Mo and Cr, if they reacted by the same mechanism, would increase the hardenability locally so retarding ferrite formation. Elements which, like Si, reduce hardenability are Al and Co and so compounds of these were considered. These were generally very stable, e.g. Al_2O_3 or too unstable and toxic, e.g. AlC, but CoO was found to have a ΔG_F^0 very similar to that of SiC. Hence a series of specimens were prepared with the chrome steel 4857 used previously interfaced with CoO. Reaustenitising treatment was kept constant at 900°C for 10mins followed by isothermal treatments at 450, 505 and 550°C for various times from 1 minute to 45 minutes. A continuously cooled specimen was also prepared for comparison, the various treatments being presented in Table VIII.5.

The similar stabilities of SiC and CoO and the behaviour of Co on hardenability leads to the expectation that there will be ferrite nucleation at the ceramic/steel interface due to some reaction of the two components. If the activities of Si and Co are similar in the steel then a dissolution may take place, although the disposal of oxygen released may pose a problem as its solubility is

well below that of carbon in austenite.

Observation of the bond after treatment indicated that some reaction had occurred with the initial black powder becoming a continuous silvery/black sheet. The adherence of this layer to the steel was generally poor, separation of the two steel pieces readily taking place across the ceramic interlayer. The bond strength for 4857/SiC on the other hand was very good with extensive dissolution and diffusion.

Closer examination reveals a substantial change in the ceramic interlayer but relatively little effect on the surrounding steel. The interlayer now consists of a series of light etching precipitates which are arranged parallel to the original interface. At short treatment times, fig. 8.35, these precipitates remain as discrete globular particles, but with increased time they become continuous lines of precipitate. The thickness of the interlayer of CoO was important with a much larger proportion of the precipitate resulting from thinner interface regions of the same specimen, fig. 8.36. These lines of precipitates approximately occupy the outer third of the interlayer and when they are discrete, short times, the central third remains porous, as reflected in the microhardness results fig. 8.37. The greater density of the outer regions imparts a greater hardness on them. As the precipitates become more continuous the central region also becomes more dense with the appearance of light precipitates (globular) in it. Sufficiently long treatments gave fully continuous precipitates in thin interlayers. In addition, a grey layer was observed at the interlayer/martensite interface, which thickens slightly with extended heat treatment. A variation in the steel microstructure is also noted with the region adjacent to the interlayer etching more lightly and having a lower hardness than that further away, fig. 8.38. Fig. 8.39 illustrates the variation in the interlayer microstructure with isothermal treatment time, the dimensions of each region being summarised in Table VIII.6.

EDS results, fig. 8.37, indicated that the light precipitates were iron rich, the darker ones being cobalt rich and the porous layer being entirely Co (plus undetected light elements e.g. oxygen). Thus the porous layer is unreacted CoO powder and the appearance of the precipitates can be linked to the ingress of iron into the ceramic. The change in the interlayer with increased isothermal time is the result of increased Fe diffusion. Increased [Fe] further into the interlayer correlate with the appearance of more light precipitates/grey phase further towards the interlayer centre. The chromium level across the entire interlayer was minimal. The distribution of these three elements was mapped out from digital processing of EDS data from a scanning spectrum of the interlayer (DIGIMAP). The generally low Cr content meant that the dwell time, the time the spectra is sampled from each successive beam position on the specimen, had to be 70ms, which made beam stability very important, total sampling time being around 40mins. The image processing and resolution were improved by increased dwell time. Peak overlap between Fe K_{β} and Co K_{α} necessitated the use of windows centred on Cr K_{α} , Fe K_{α} and Co K_{β} in order to distinguish between these elements and their occurrence. The resulting maps are shown, with associated micrographs, in figs 8.40, with different colours representing different intensities in the

order

Green > Light Blue > Dark Blue > Pink

These show that the grey layer at the ceramic/steel interface is enriched in chromium an effect revealed by superposition of element maps using a different colour for each element, fig. 8.41.

Identification of the phases present by X-ray diffraction, fig. 8.42, revealed peaks characteristic of:

- (i) Cr_7C_3 , which would correspond to the Cr enriched grey martensite/ceramic interface layer.
- (ii) CoO , this could arise from the presence of unreacted powder and the dark areas between the precipitates.
- (iii) FeO & $(\text{Fe},\text{Co})_3\text{O}_4$, these are the lighter precipitates which result from reaction of the ingressed Fe with CoO . The phase diagram for this system predicts that this should give a spinel solid solution field at 900°C based on $(\text{Fe}, \text{Co})_3\text{O}_{4\pm x}$ ⁽²⁸¹⁾. On cooling to 500°C this should decompose spinodally to end members with Fe cation fractions of 0.1 and 0.65.¹ These would be the grey and light phases respectively.

The reaction route can now be seen to be:

- (i) Diffusion of Fe into CoO to form a solid solution at 900°C , probably around the surface of the original powder particles.
- (ii) Hoshino and Peterson⁽²⁸²⁾ measured the diffusivity of various transition metal ions in CoO in the temperature range $1000\text{--}1500^\circ\text{C}$ by tracer methods. Using their values of the pre-exponential factor, D_0 , and activation energy, Q , the diffusivities of Fe and Cr at 900°C in CoO can be estimated.

$$\begin{aligned} D_{\text{Cr}}^{\text{CoO}} &= 5.14 \times 10^{-10} \\ D_{\text{Fe}}^{\text{CoO}} &= 4.97 \times 10^{-14} \end{aligned}$$

These indicate that the diffusion of Cr through CoO is much slower than that of Fe and so, as Fe is removed into the ceramic, the interface region of the steel is enriched in Cr. A simple $x^2 = Dt$ calculation predicts a penetration of Fe of $\approx 5\mu\text{m}$ into CoO after 10 minutes at 900°C , whereas the actual distance is much greater. Some of the difference may be due to the greater Fe level in the oxide increasing the diffusion rate as will the driving force for dissolution. However, it seems likely that some surface diffusion takes place during initial ingress, although reaction between Fe and CoO requires bulk diffusion.

(iii) Reaction of Fe with CoO forms the spinel which, on quenching, decomposes spinodally to give the light precipitate and the greyer layers. Reaction is incomplete as evidenced by the presence of reaction rims around CoO particles in the centre of the interlayer, fig. 8.39.

(iv) At $500\text{--}600^\circ\text{C}$ conditions are favourable for the formation of Cr_7C_3 in the enriched Cr layer at the interface. This explains its presence in the specimens isothermally treated at 500 and 550°C , but its absence in the continuously cooled specimen and that treated at 450°C . The formation of this carbide denudes the interface region in carbon and so leads to a slight reduction

¹ Fe cation fraction is given by (atomic % Fe) divided by sum of (atomic % Fe + atomic % Co)

in hardenability in this region. It is this that is responsible for the change in the bainite/martensite in the steel observed when this film is formed.

This process is summarised in fig. 8.43.

As the carbide film is supposed to form after the reaction and diffusion of Fe if the bulk is assumed to take place at the re-austenitising temperature, then it should not act as a barrier to reaction. This was confirmed by use of longer reaction times at 900°C when extensive reaction occurred. Extension of isothermal treatment time to 45 minutes for a 4857/CoO couple gave increased precipitation within the interlayer, fig. 8.39(f).

Unlike Cr, Ni can diffuse into CoO at a rate similar to that of Fe and also react, there existing a solid solution at 900°C which decomposes to two NaCl structure solid solutions below 750°C. Hence reaction would be expected to extend in both directions when carried out on the austenitic steel 4863. Therefore, a further run was carried out using 4863 heating to 900°C for 10 minutes then holding at 500°C for 60s before quenching to room temperature. The resulting microstructure, fig. 8.44, exhibited the same precipitation within the interlayer as for the chrome steel, but in this case the grey interface layer was absent. Instead there was extension of the reaction zone into the steel, where interdiffusion of Ni and Co had occurred up to $\approx 20\text{-}22\mu\text{m}$, as was shown by EDS. The interpenetration of Co into the steel extends from 20-30 μm , which is probably mostly diffusion of Co into the steel. The diffusivity of Ni in CoO ⁽²⁸²⁾ at 900°C being only:

$$5.29 \times 10^{-12} \text{ cm}^2 \text{ s}^{-1}$$

and so would only diffuse a short distance into the interlayer, as evidenced by EDS results, which only reveal Co and Fe in the interlayer.

The chemical activity of CoO is seen to be by diffusion of substitutional alloying elements (Fe) into the ceramic in contrast to the silicon ceramics ~~where~~ ^{diffuse} substitutional (and interstitial) elements into the steel. Therefore, two mechanisms for chemically active inclusions have been identified one of which is long range, but the other (CoO) is restricted to the extent of the interlayer and so is not viable for α_{acic} nucleation.

Table VIII.1. Heat treatments used to compare Si based ceramics.

| Steel | Ceramic | Austenitising | | Quench Time/s | Isothermal | |
|-------|--------------------------------|----------------|------------|------------------------------|----------------|--------|
| | | Temperature/°C | Time /mins | | Temperature/°C | Time/s |
| 4857 | SiC | 900 | 1 | 100 | 505 | 60 |
| 4857 | Si | 900 | 1 | 81 | 505 | 60 |
| 4857 | Si ₃ N ₄ | 900 | 10 | 101 | 502 | 60 |
| 4857 | SiO ₂ | 900 | 10 | 112 | 505 | 60 |
| 4863 | SiC | 900 | 10 | Quenched to room temperature | | |
| 4857 | SiC | 900 | 10 | 35 | 700 | 120 |
| 4857 | SiC | — | — | — | 500 | 600 |

Table VIII.2. Isothermal heat treatments at 505°C for 4857/SiC couples reaustenitised at 900°C for 60s.

| Quench time from 900-505°C (s) | Isothermal holding time (s) |
|--------------------------------|-----------------------------|
| 70 | cont. cool |
| 70 | 10 |
| 81 | 30 |
| 82 | 45 |
| 100 | 60 |

Table VIII.3. Austenite carbon (x_1^γ) and silicon (x_2^γ) levels (mole fractions) in equilibrium with SiC. ΔG_m^γ represents the deviation (Jmol^{-1}) from true equilibrium.

| T (°C) | x_1^γ | x_2^γ | ΔG_m^γ |
|--------|--------------|--------------|---------------------|
| 900 | 0.0292 | 0.1100 | 169.4 |
| 900 | 0.0542 | 0.0800 | 173.6 |
| 900 | 0.0942 | 0.0400 | 27.1 |
| 800 | 0.0192 | 0.1100 | 100.9 |
| 800 | 0.0892 | 0.0300 | 175.0 |
| 700 | 0.0342 | 0.0700 | 104.7 |
| 700 | 0.0594 | 0.0400 | 61.4 |
| 600 | 0.0342 | 0.0500 | 112.4 |
| 600 | 0.0792 | 0.0100 | 101.7 |
| 500 | 0.0342 | 0.0300 | 25.2 |
| 500 | 0.0442 | 0.0200 | 171.8 |

Table VIII.4. Compositions maximising free energy decrease between final Fe-Si-Cr-C steel and starting 4857.

| Steel (phase) | Ceramic | T (°C) | x_C | x_{Si} | $\Delta G (\text{Jmol}^{-1})$ |
|-------------------|---------|--------|--------|----------|-------------------------------|
| 4857 (γ) | SiC | 900 | 0.0142 | 0.3000 | -0.2286.10 ⁺⁵ |
| 4857 (γ) | SiC | 800 | 0.0142 | 0.3000 | -0.2258.10 ⁺⁵ |
| 4857 (γ) | SiC | 700 | 0.0142 | 0.3000 | -0.2211.10 ⁺⁵ |
| 4857 (γ) | SiC | 600 | 0.0142 | 0.3000 | -0.2214.10 ⁺⁵ |
| 4857 (γ) | SiC | 500 | 0.0142 | 0.3000 | -0.2198.10 ⁺⁵ |
| 4857 (α) | SiC | 900 | 0.0142 | 0.2600 | -0.1090.10 ⁺⁵ |
| 4857 (α) | SiC | 800 | 0.0142 | 0.2600 | -0.1160.10 ⁺⁵ |
| 4857 (α) | SiC | 700 | 0.0142 | 0.2700 | -0.1232.10 ⁺⁵ |
| 4857 (α) | SiC | 600 | 0.0142 | 0.2800 | -0.1307.10 ⁺⁵ |
| 4857 (α) | SiC | 500 | 0.0142 | 0.2900 | -0.1385.10 ⁺⁵ |
| 4857 (α) | Si | 900 | 0.0142 | 0.2500 | -0.1090.10 ⁺⁵ |
| 4857 (α) | Si | 800 | 0.0142 | 0.2600 | -0.1160.10 ⁺⁵ |
| 4857 (α) | Si | 700 | 0.0142 | 0.2700 | -0.1232.10 ⁺⁵ |
| 4857 (α) | Si | 600 | 0.0142 | 0.2800 | -0.1307.10 ⁺⁵ |
| 4857 (α) | Si | 500 | 0.0142 | 0.2900 | -0.1385.10 ⁺⁵ |

x_C and x_{Si} are mole fractions of carbon and silicon respectively

ΔG is free energy difference between 4857 and final composition

Table VIII.5. Heat treatments for 4857/CoO couples. Bonding pressure is 12.5MPa.

| T_{γ} (°C) | t_{γ} (min) | t_q (s) | T_{iso} (°C) | t_{iso} (s) |
|-------------------|--------------------|-----------|----------------|------------------|
| 900 | 10 | 110 | Argon | continual quench |
| 900 | 10 | 92 | 508 | 60 |
| 900 | 10 | 118 | 503 | 300 |
| 900 | 10 | 105 | 504 | 900 |
| 900 | 10 | 110 | 505 | 2700 |
| 900 | 10 | 88 | 450 | 300 |
| 900 | 10 | - | 550 | 300 |

where

T_{γ} =reaustenitisation temperature

t_{γ} =reaustenitisation time

t_q =quench time from 900 to 505°C

T_{iso} =isothermal temperature

t_{iso} =isothermal time

Table VIII.6. Widths (μm) of various regions in CoO interlayer after heat treatment after reaustenitisation for 10 minutes at 900°C.

| Heat Treatment | Grey Film | Banded | Speckled | Porous | Total |
|----------------|-----------|--------|----------|--------|-------|
| Cont. Cool | - | 55 | - | 40 | 150 |
| 505°C/300s | 4 | 30 | 36 | - | 100 |
| 505°C/900s | 4 | 28 | 22 | - | 80 |
| 450°C/300s | - | 24 | 48 | - | 94 |
| 550°C/300s | 4 | 34 | 35 | - | 104 |

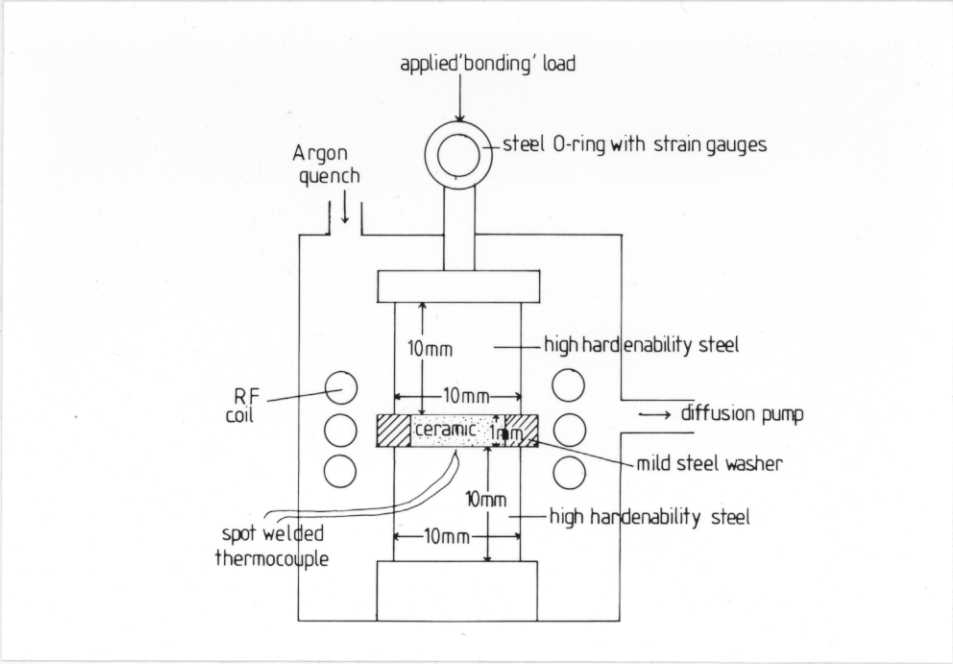
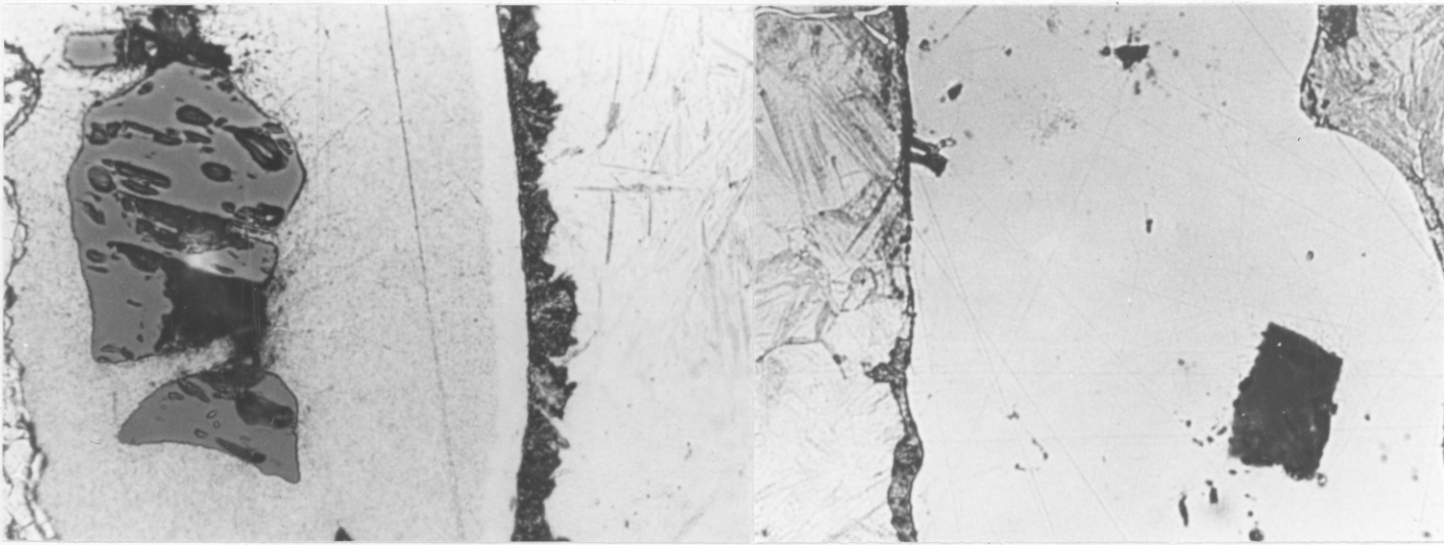


Figure 8.1. Diagram of modified diffusion bonder (INTER).



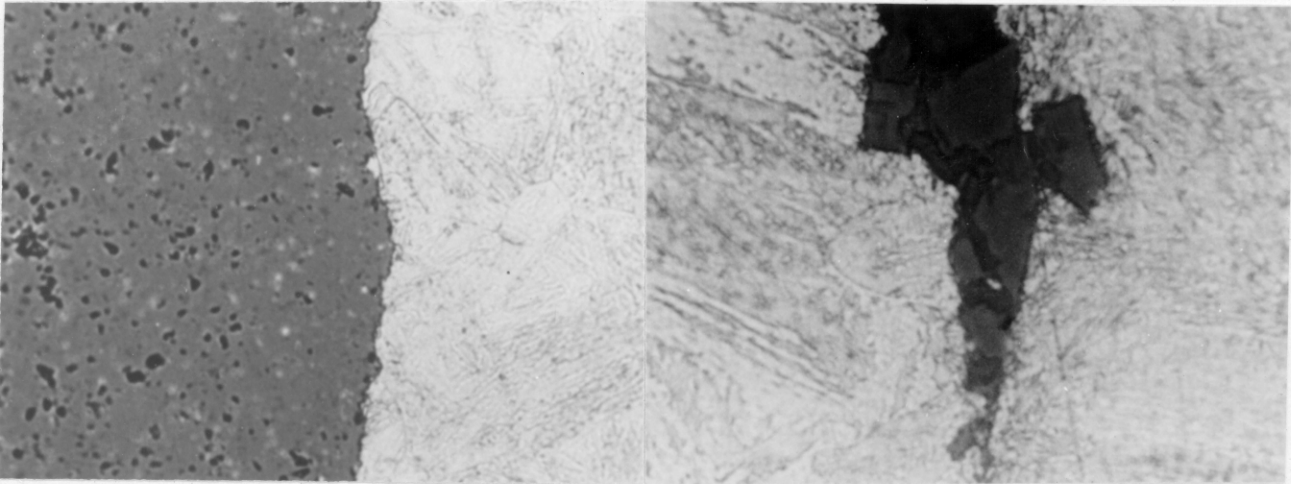
(a) 15µm

(b) 7µm

Figure 8.2. Interfacial region for 4857 bonded to (a) SiC, (b) Si, (c) Si₃N₄, (d) SiO₂. Reaustenitised at 900°C for 10 minutes then quenched to 505-508°C for 60s.

(c) 15µm

(d) 10µm



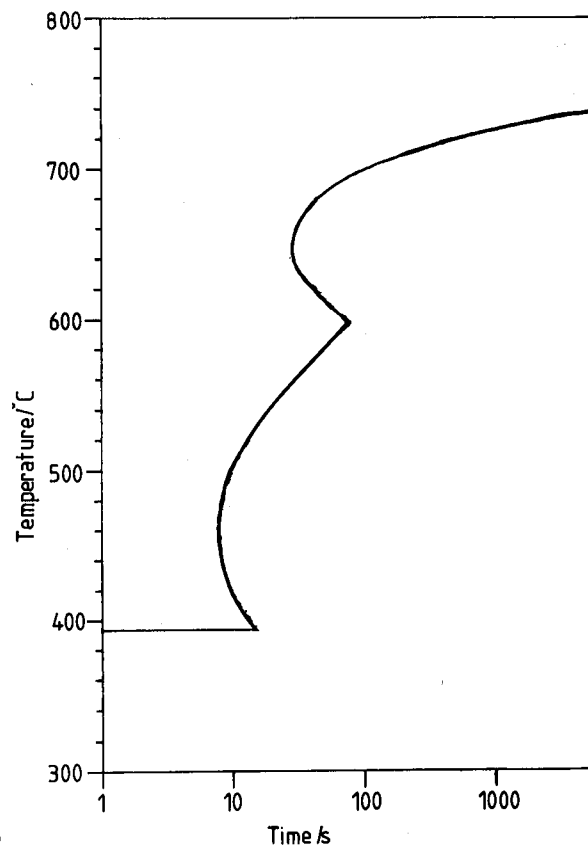
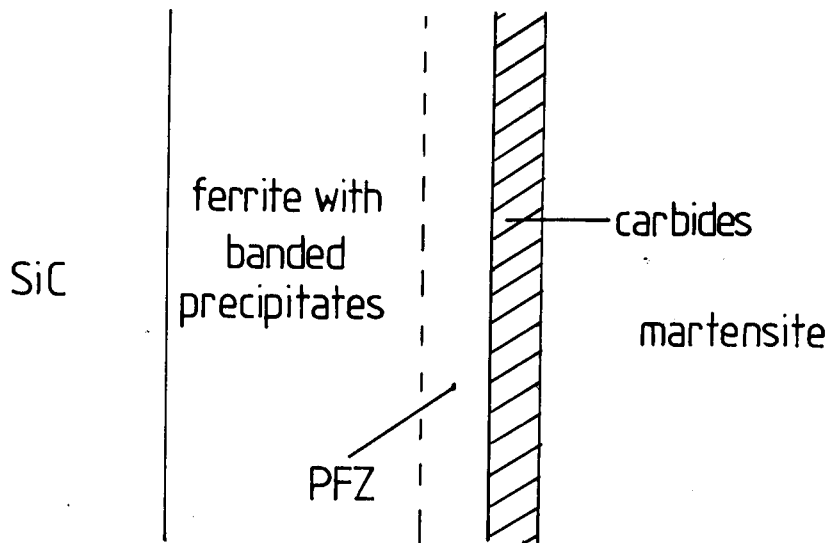


Figure 8.3. Predicted TTT curve for 4857.

Figure 8.4. Interfacial layers for heat treated 4857SiC



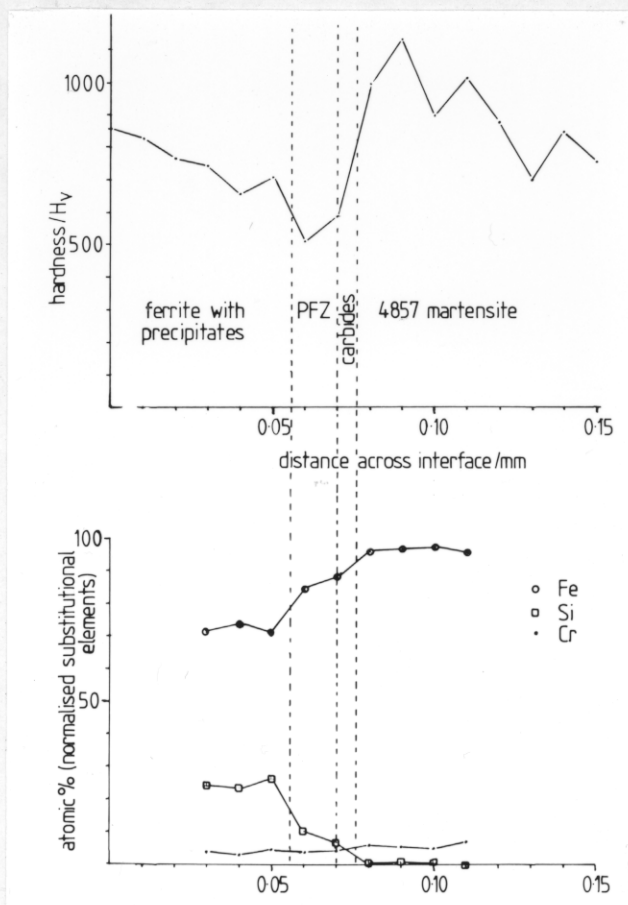
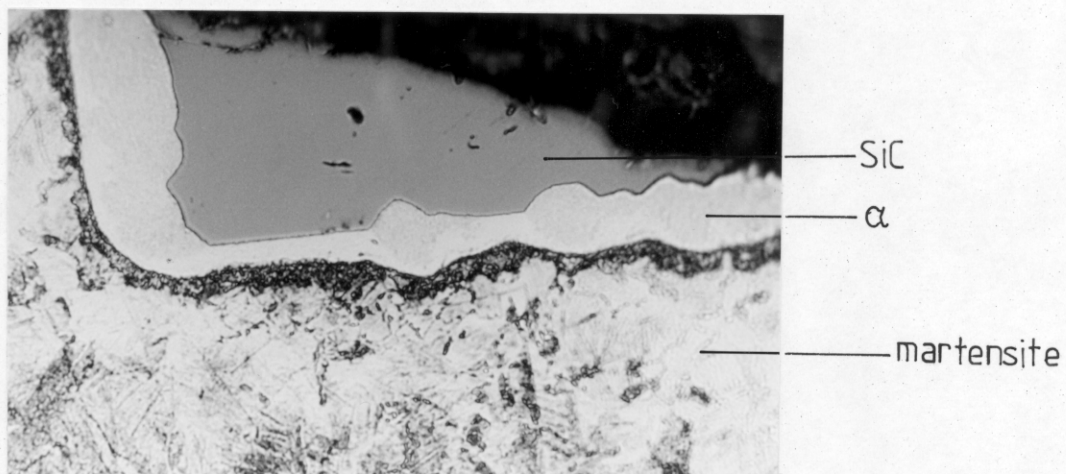
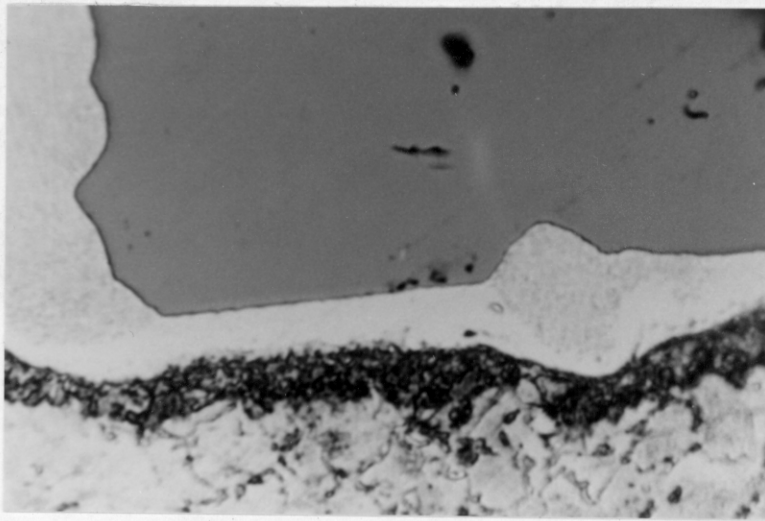


Figure 8.5. EDS trace for 4857/SiC couple shown in fig. 8.2.

Figure 8.6. 4837/SiC, continuously cooled from 900°C.

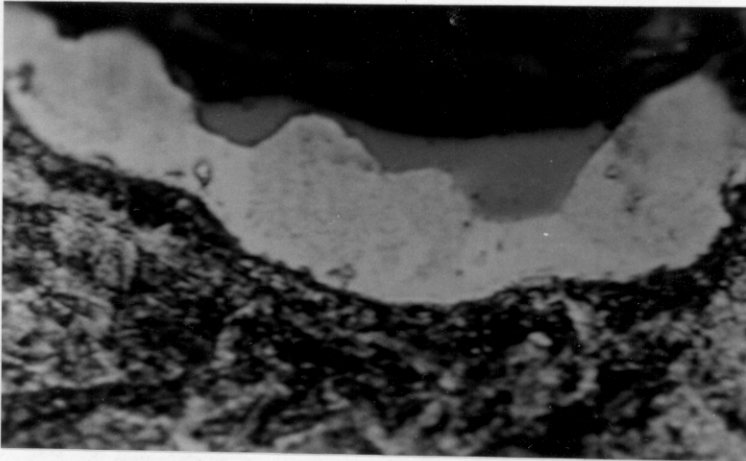
15μm —





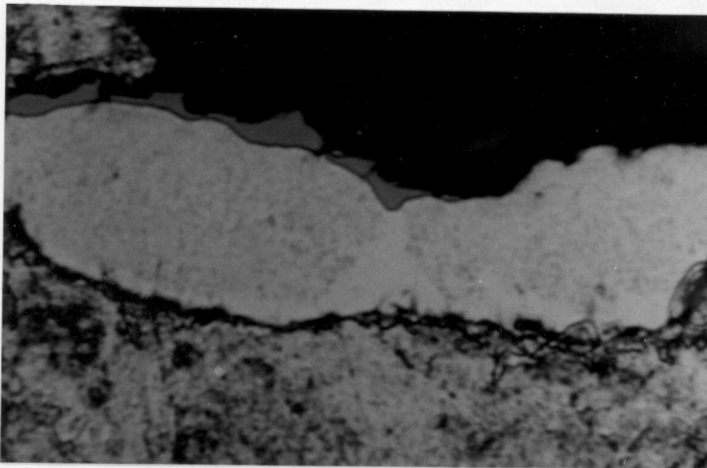
8μm

Figure 8.7. Plateau and extended PFZ, 4857/SiC. Continuously cooled from 900°C.



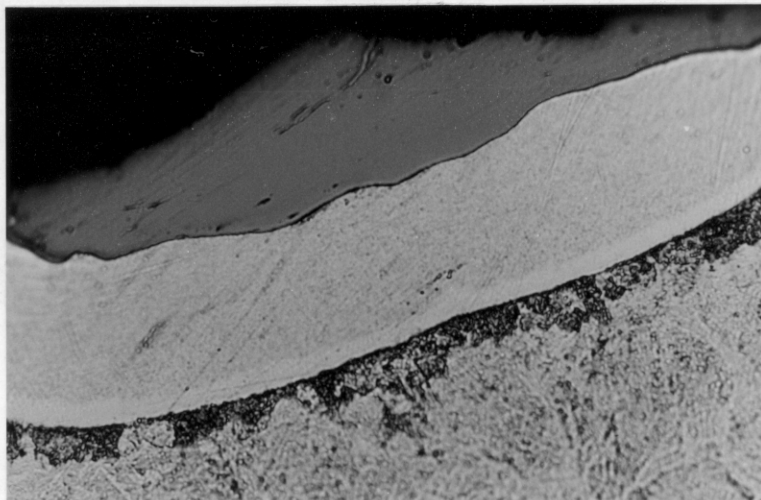
7μm

Figure 8.8. 4857/SiC, 505°C/10s.



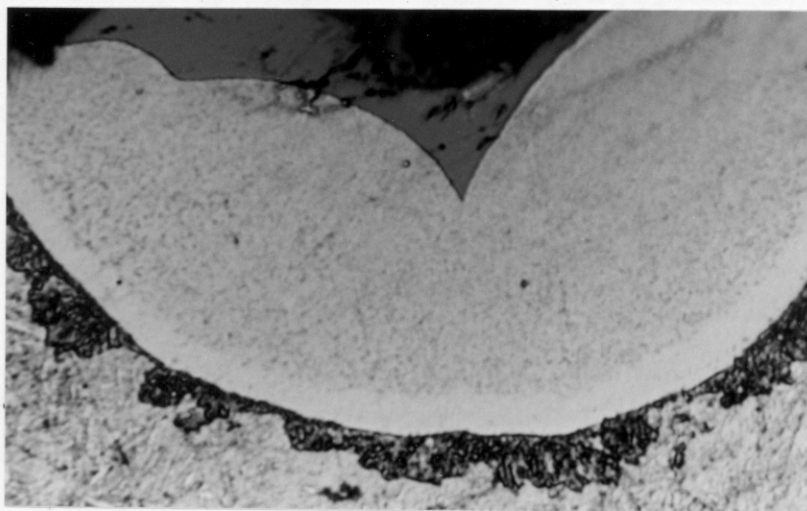
10μm

Figure 8.9. SiC peak, 505°C/10s.



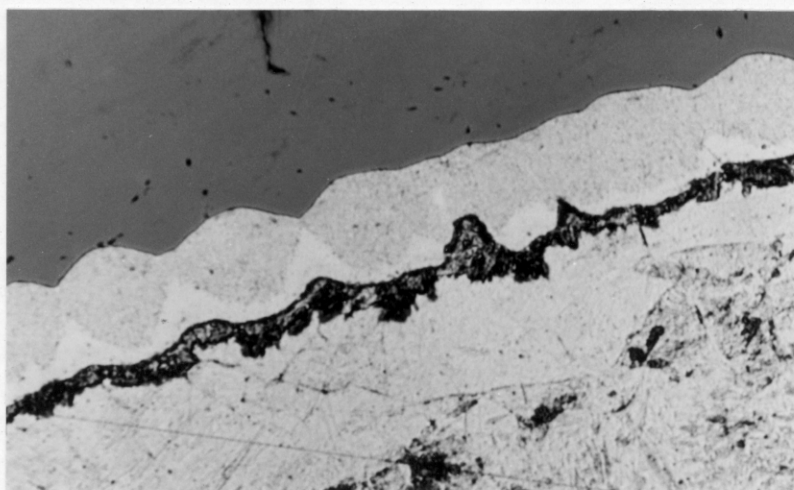
15μm

Figure 8.10. Uniform α allotriomorph, 4857/SiC, 505°C/30s.



7.5μm

Figure 8.11. SiC peak, 4857/SiC, 505°C/30s.



10μm

Figure 8.12. 4857/SiC, 504°C/45s.

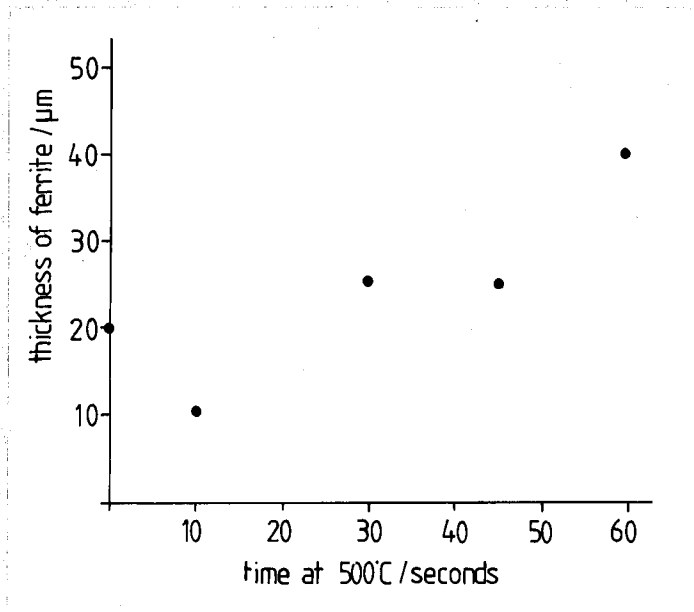


Figure 8.13. Variation of ferrite thickness with isothermal holding time at 505°C. Reaustenitisation for 1 minute at 900°C.

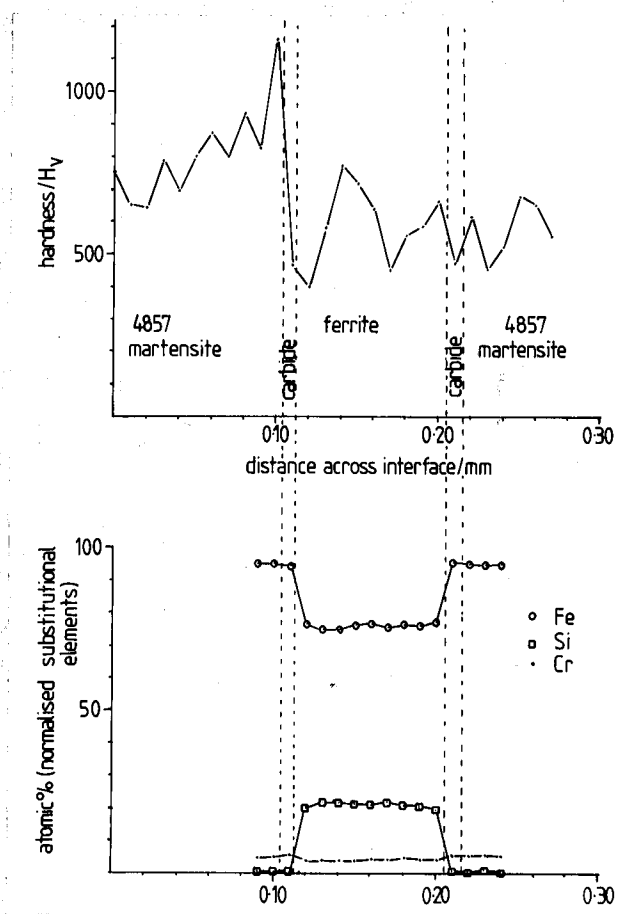


Figure 8.14. EDS trace across 4857/Si interface.

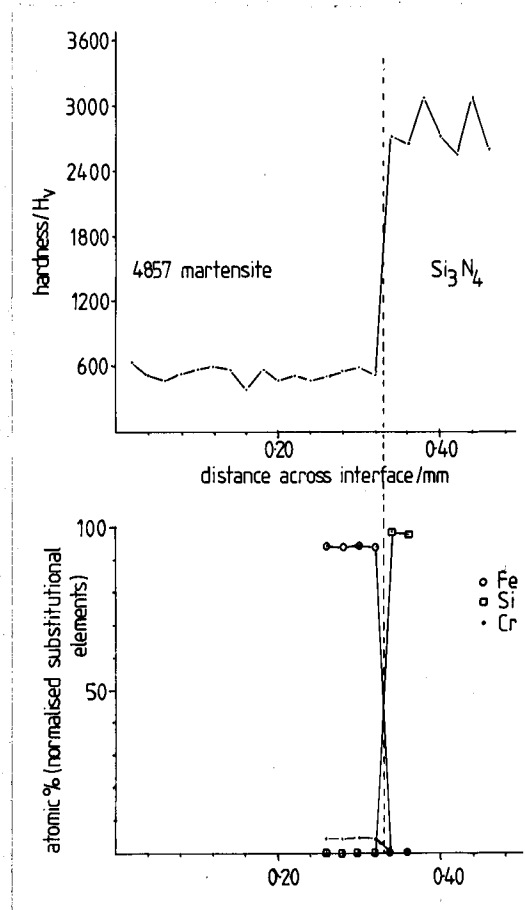


Figure 8.15. 4857/Si₃N₄ interface.

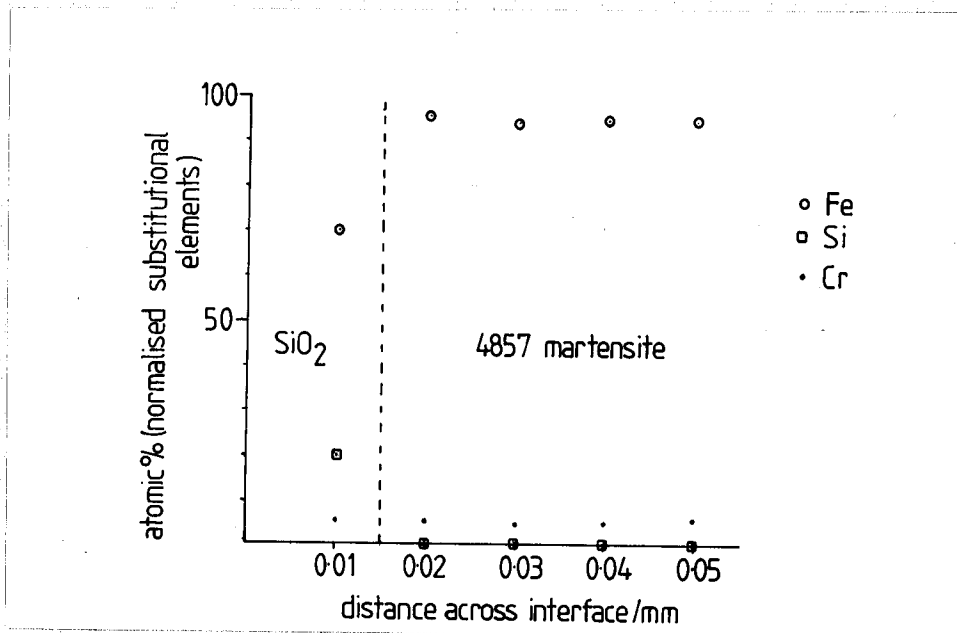
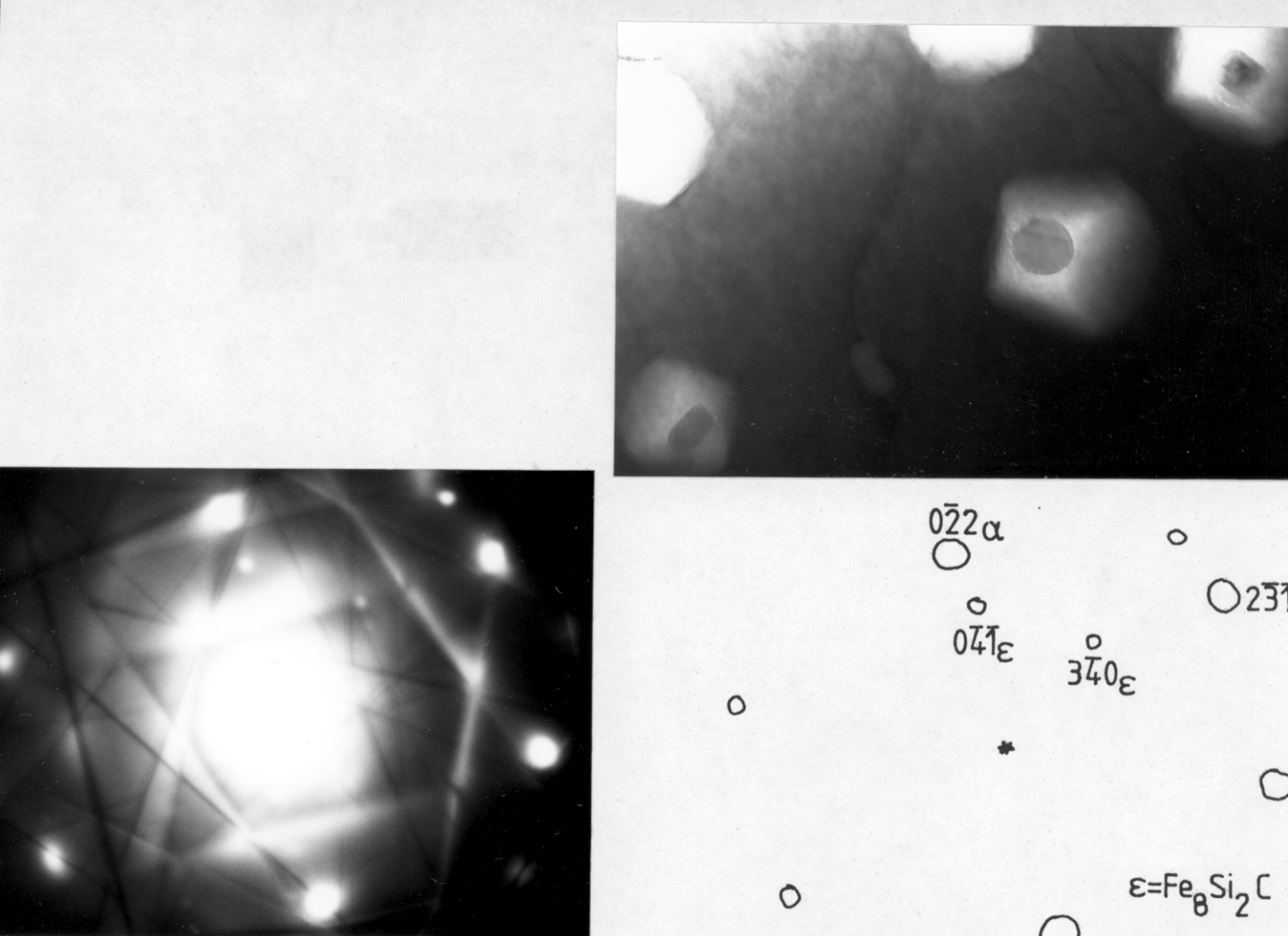


Figure 8.16. EDS trace across 4857/SiO₂ interface.



0.2 μm

Figure 8.17. Precipitates in α (right hand side) in 4857/SiC reaustenitised at 900°C for 10 minutes then held at 700°C for 120s.



0.1 μm

Figure 8.18. Bright field image of banded, spherical precipitates in 4857/SiC (900°C/10mins-700°C/120s), with SADP and analysis.

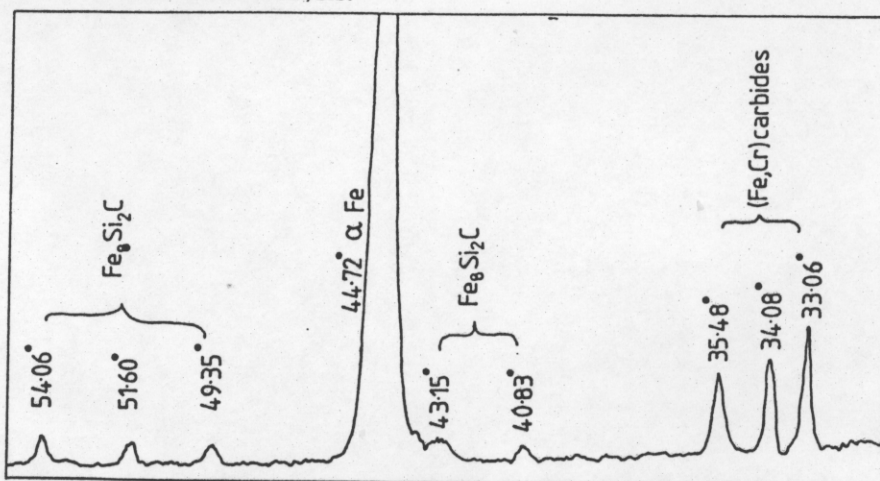


Figure 8.19. Portion of X-ray diffraction trace for 4857/SiC after heat treatment.

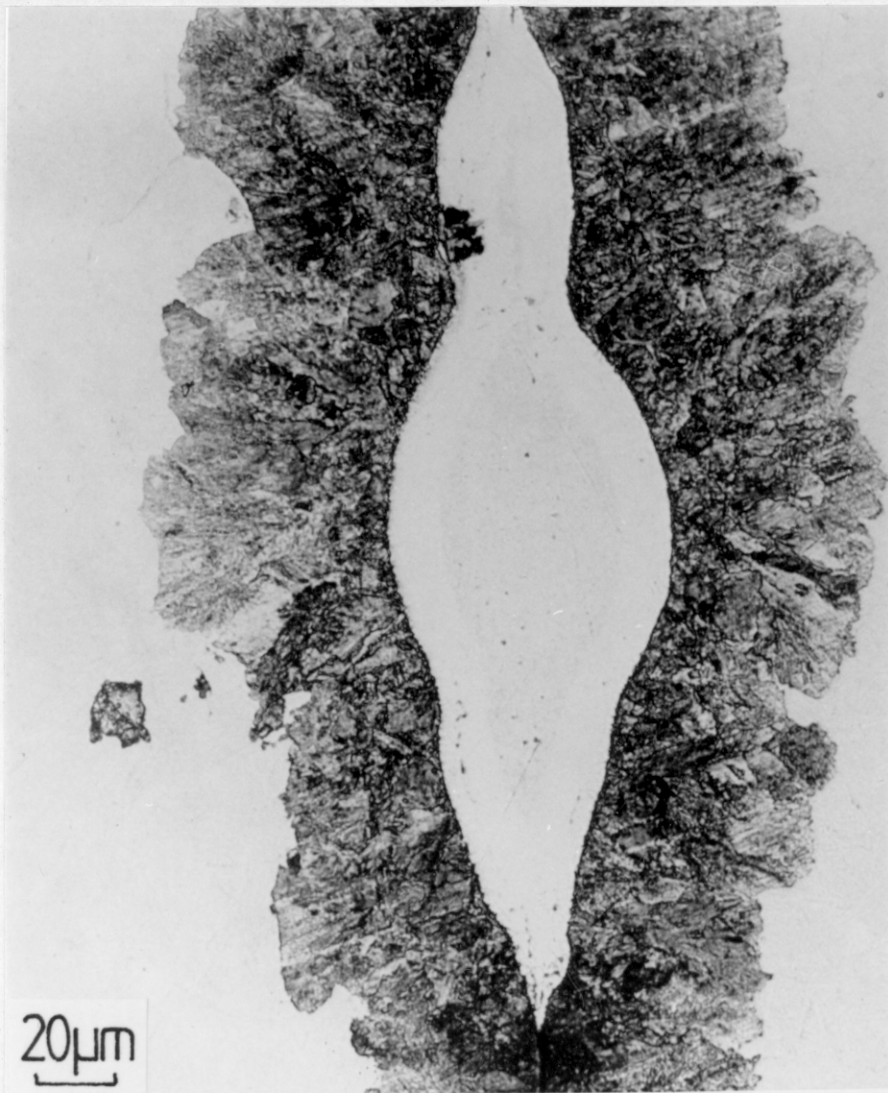


Figure 8.20. Complete dissolution of SiC after extended reaustenitisation.

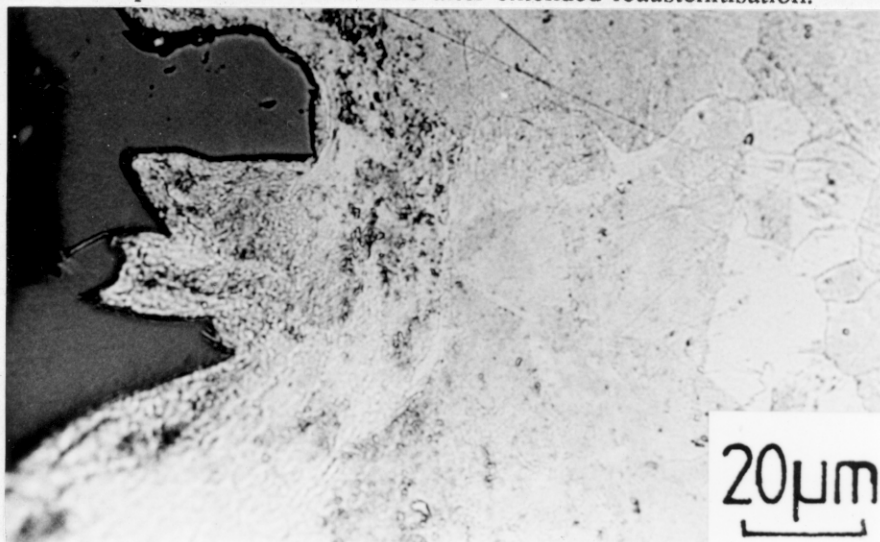


Figure 8.21. Absence of reaction or α , for 4857/SiC held at 505°C for 10 minutes without prior reaustenitisation.

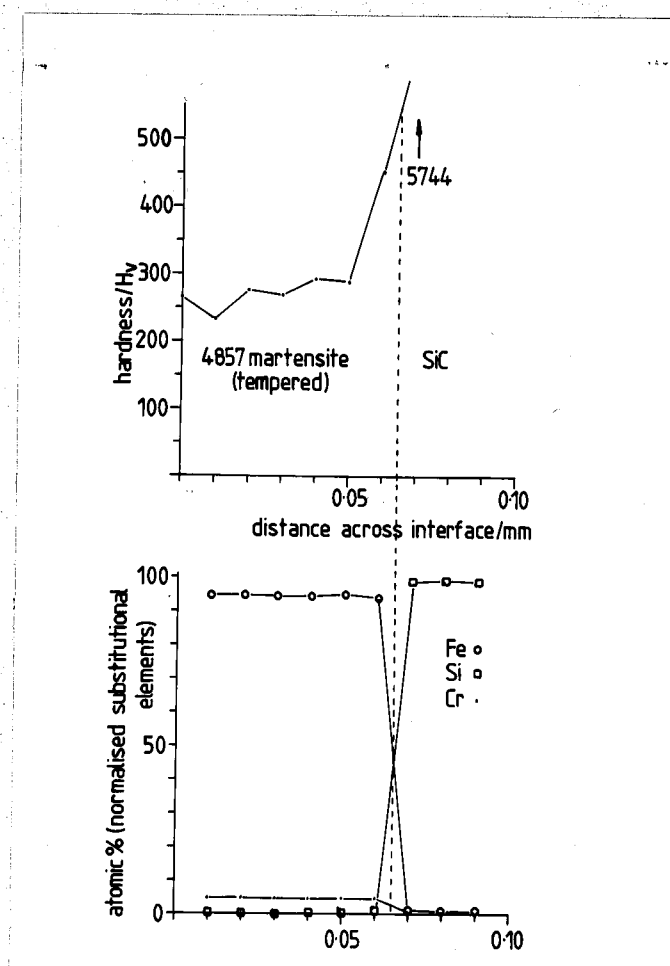


Figure 8.22. EDS trace across interface for 4857/SiC couple in fig. 8.21.

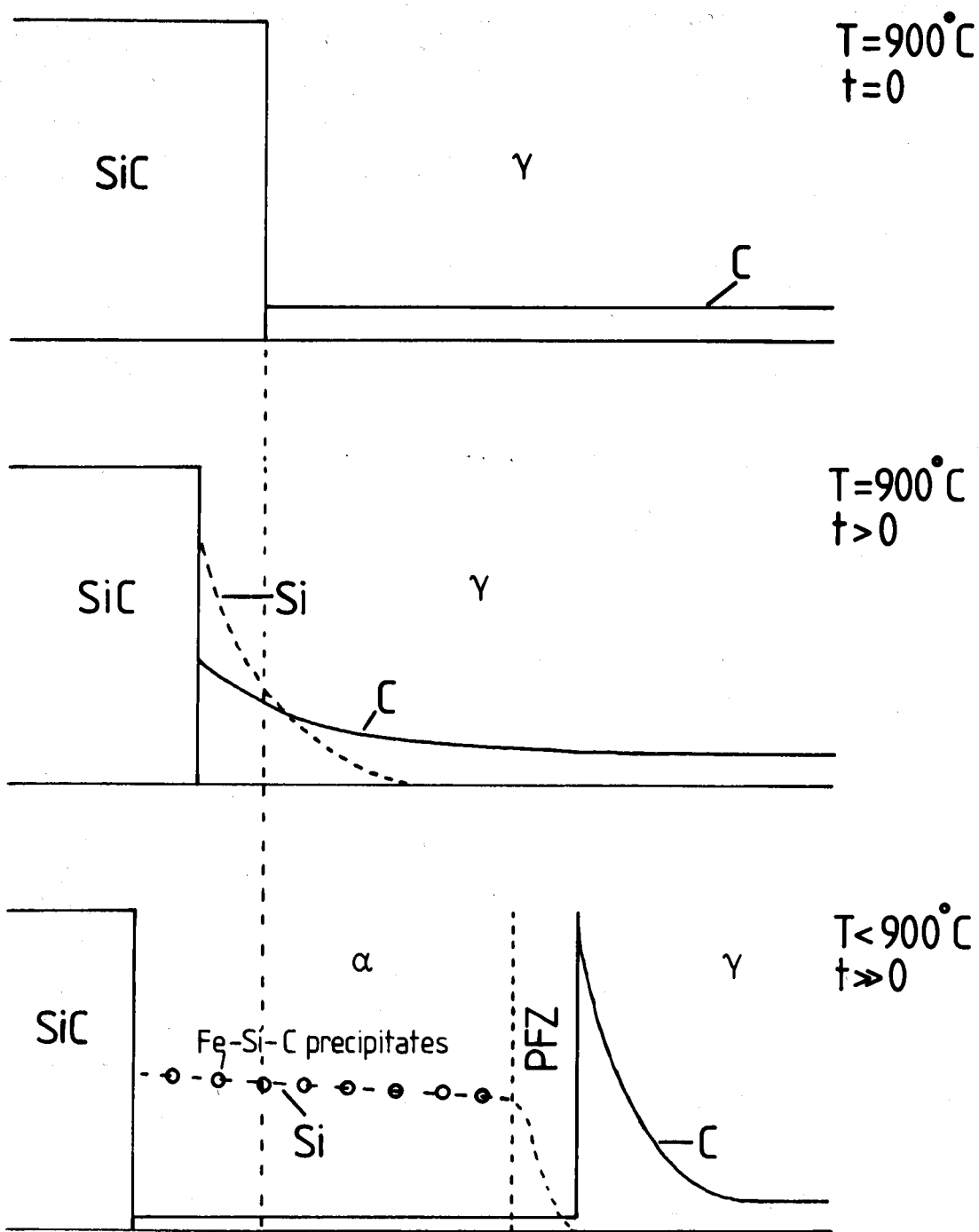


Figure 8.23. Model for dissolution of SiC in 4857.

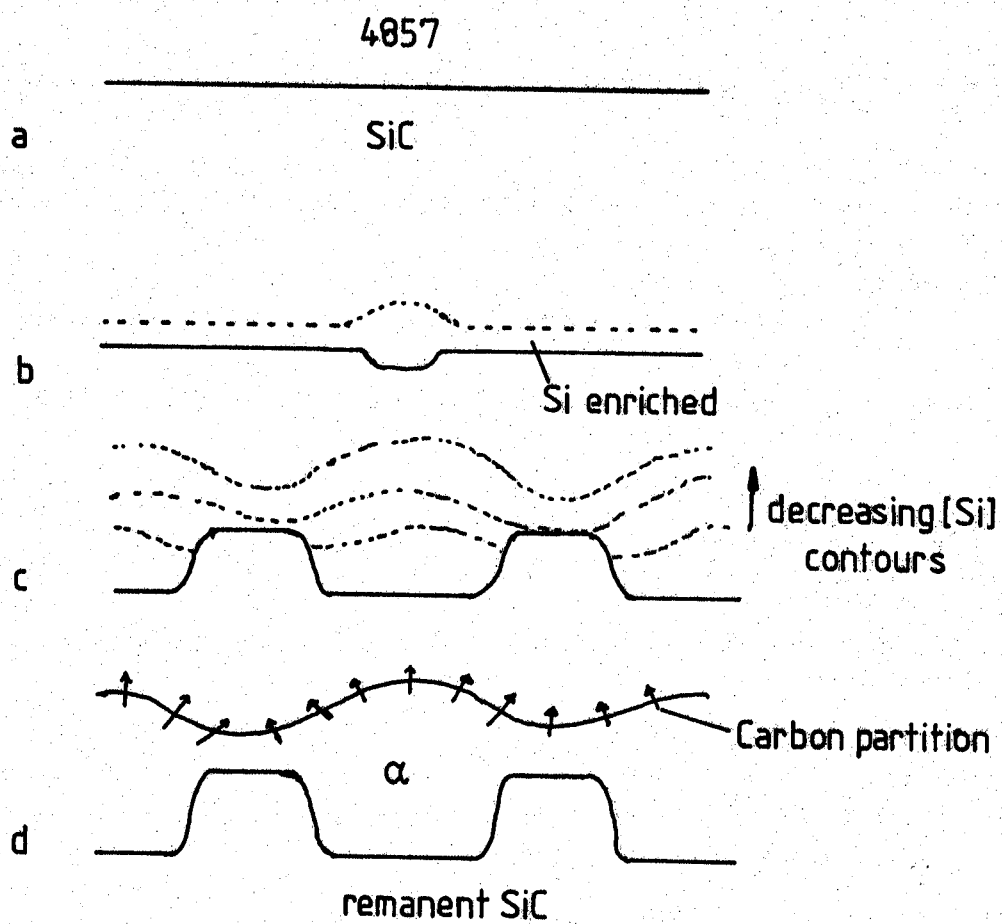
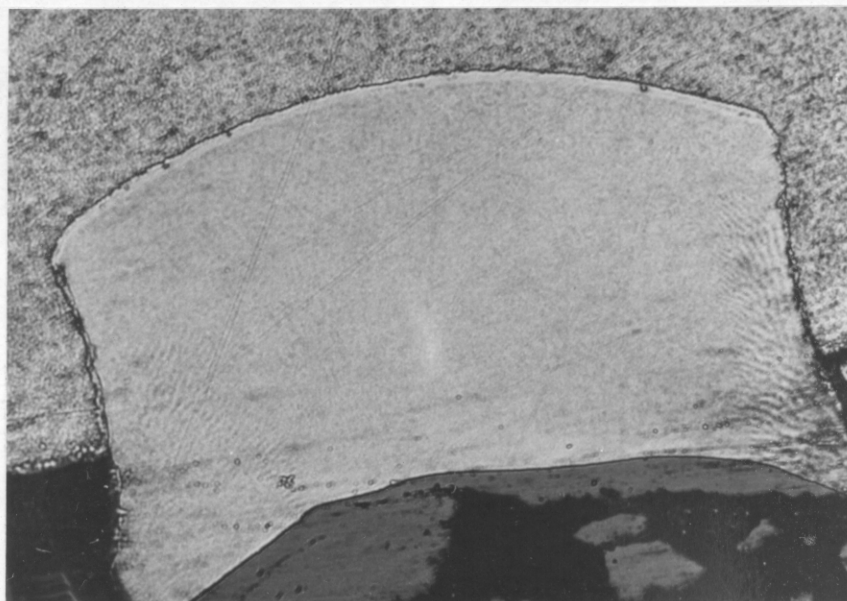
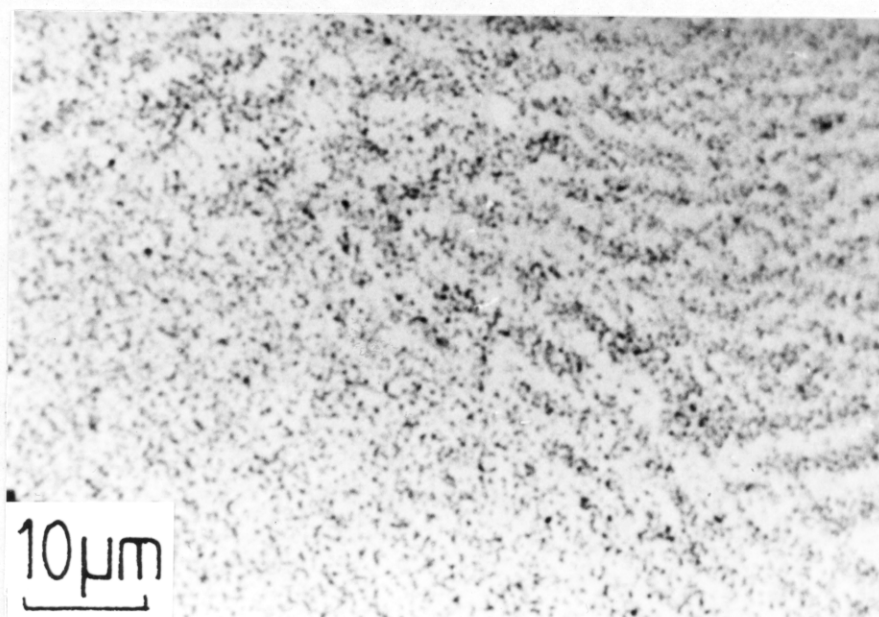


Figure 8.24. Details of plateau formation during dissolution.



(a) 30 μ m



(b)

Figure 8.25. Interface allotriomorphs for 4863/SiC, continuously cooled after 10 minutes at 900°C.

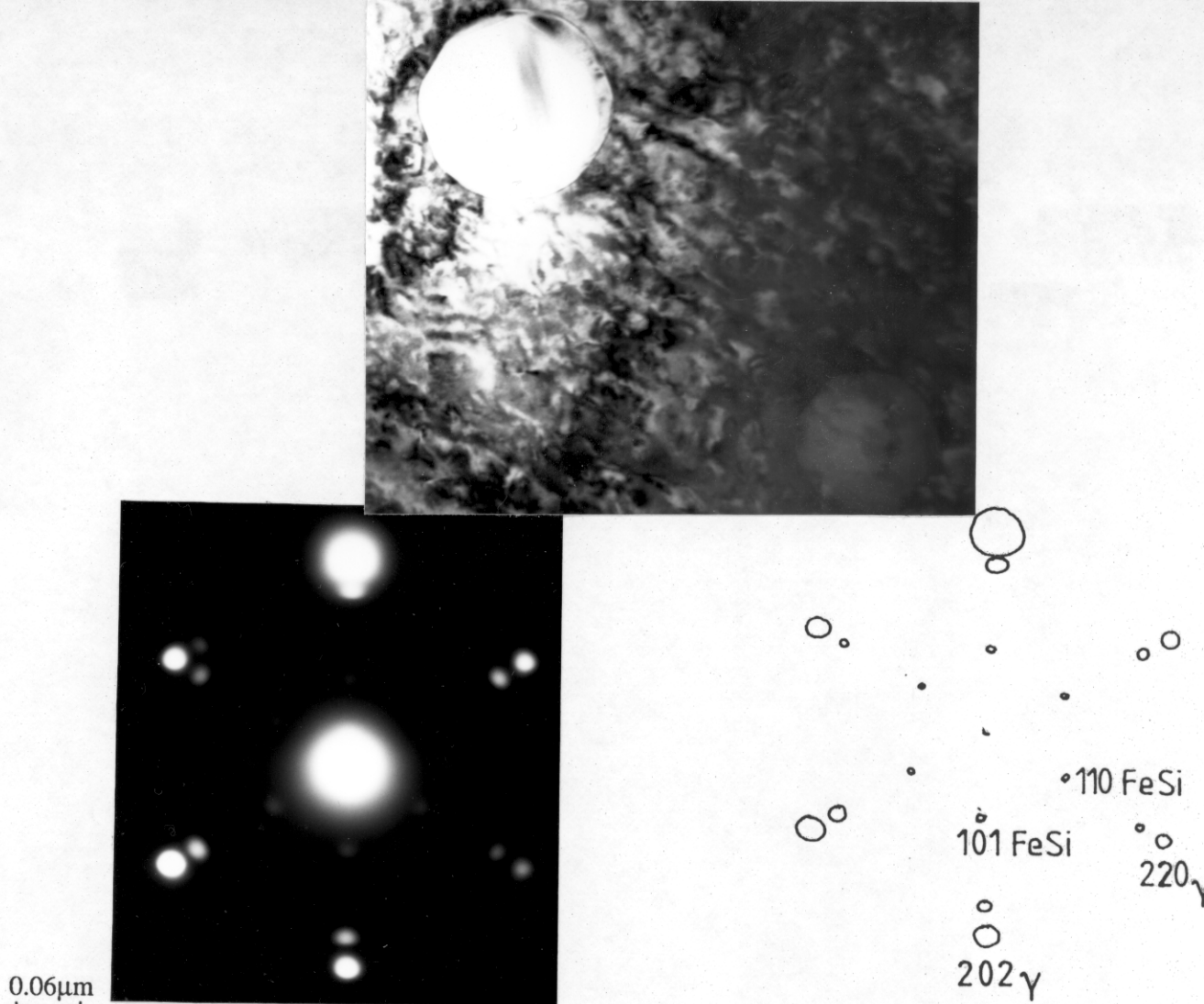


Figure 8.26. Bright field image of precipitates in 4863/SiC interface allotriomorph, SADP and analysis.

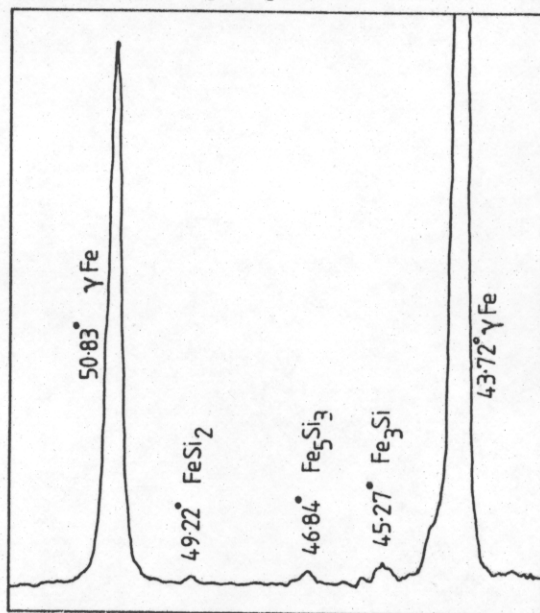


Figure 8.27. Portion of X-ray diffraction trace for 4863/SiC after heat treatment.

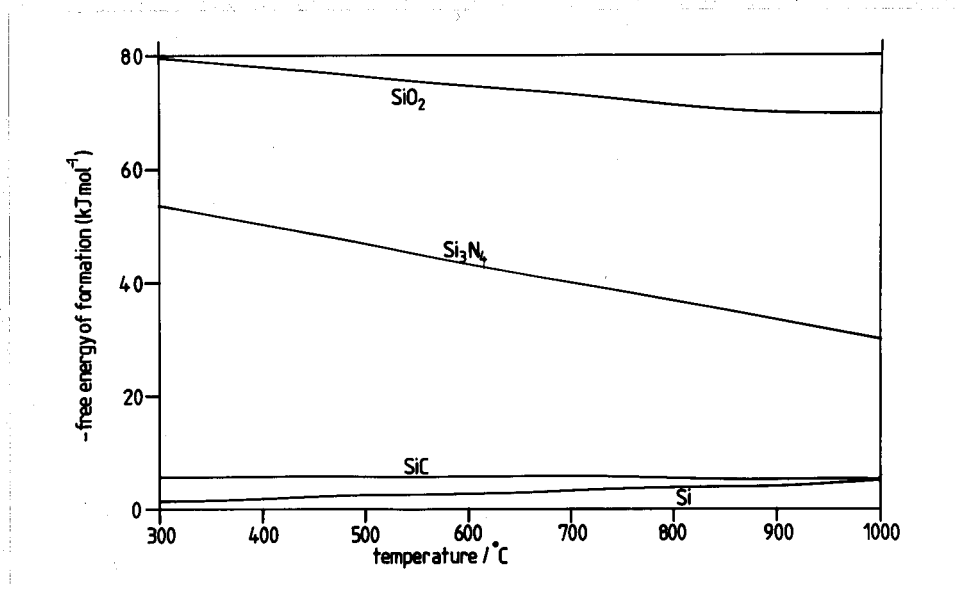


Figure 8.28. Free energies of formation of Si based ceramics.

Figure 8.29-33. The next pages show the calculated free energy of reaction plots for various steel/ceramic couples.

8.29(a). 4857(γ)/SiC

8.30. 4863(γ)/SiC

8.31(b). 4857(α)/Si

8.33. 4857(γ)/Si₃N₄

8.29(b). 4857(α)/SiC

8.31(a). 4857(γ)/Si

8.32. 4857(γ)/SiO₂

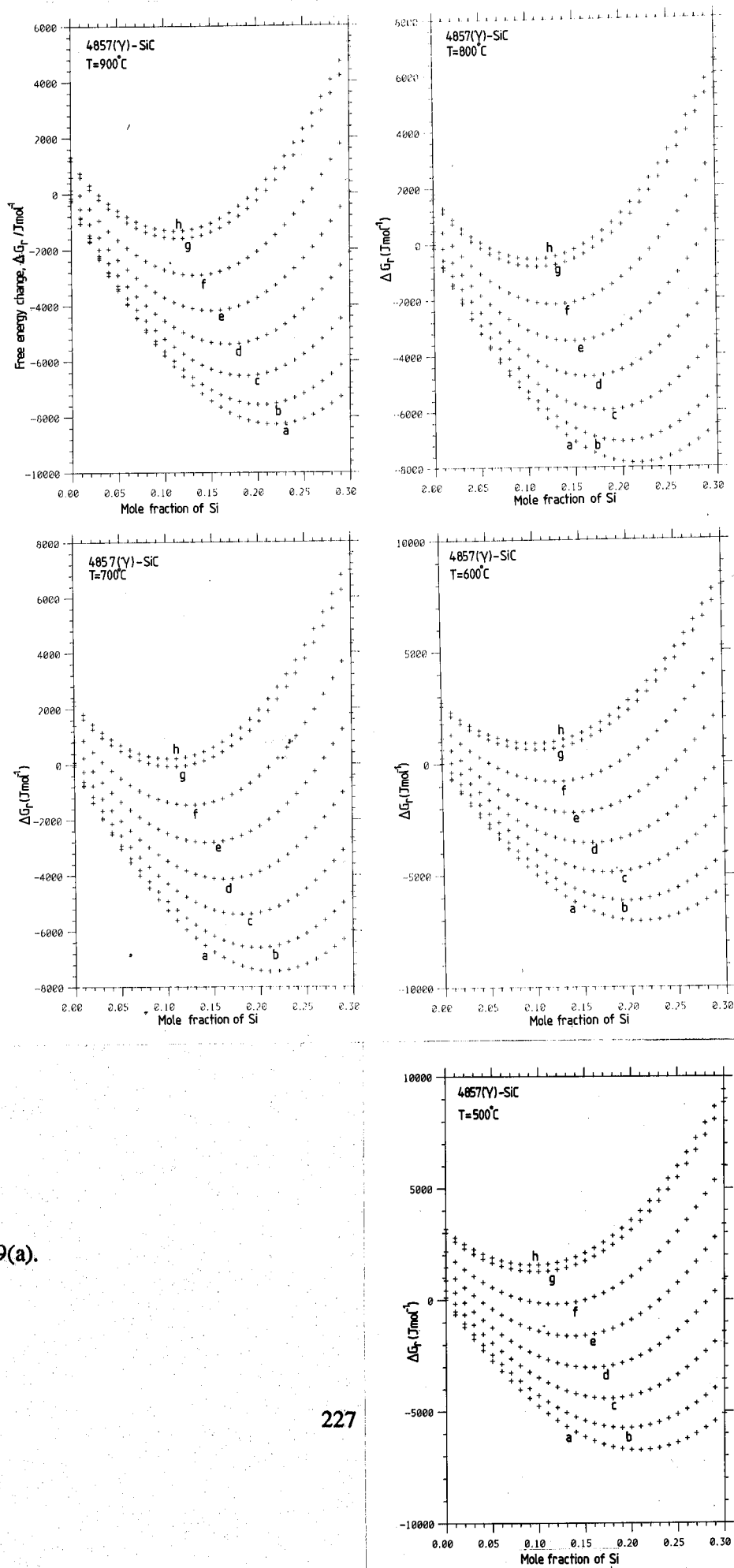


Figure 8.29(a).

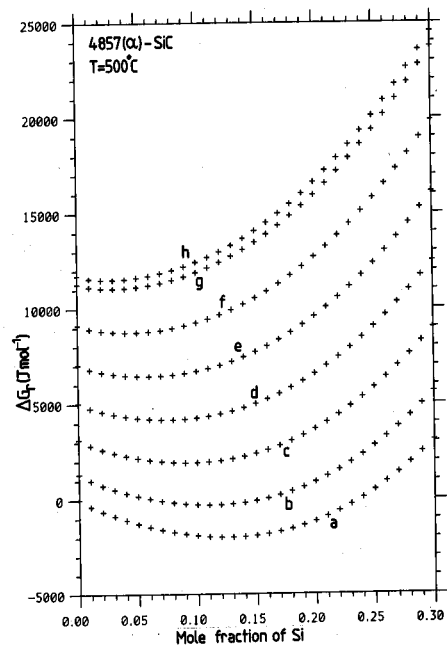
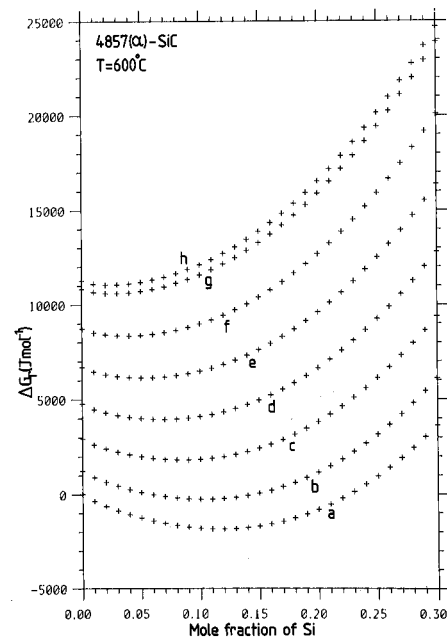
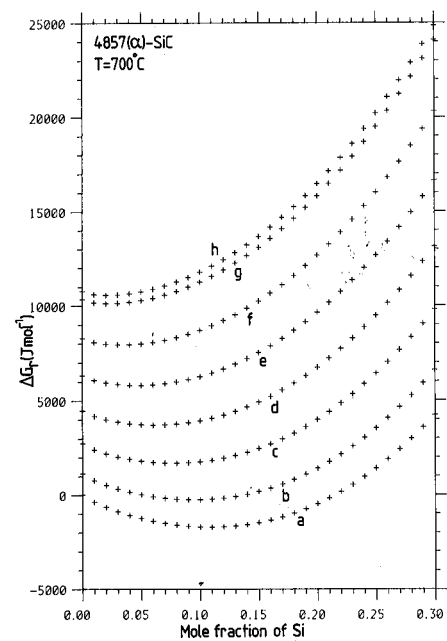
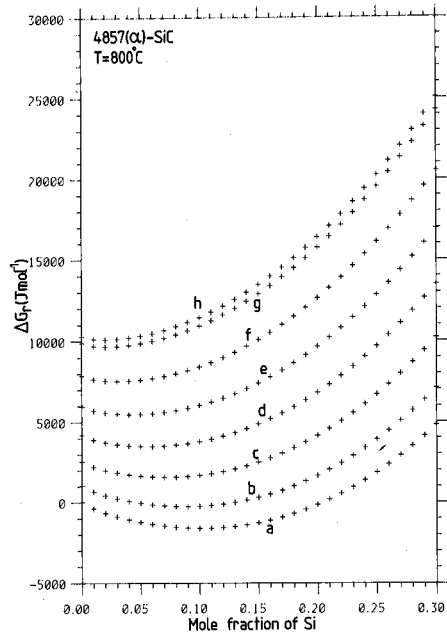
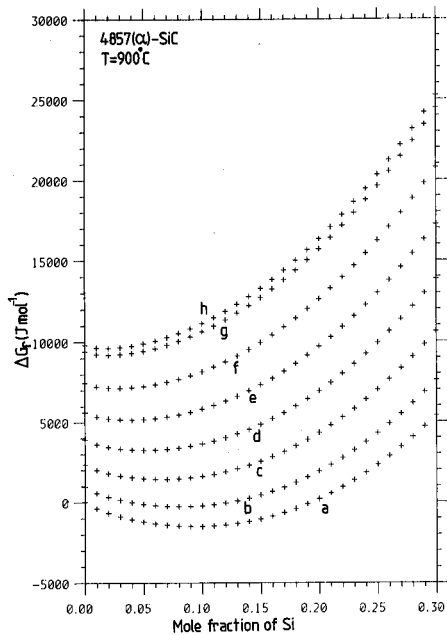


Figure 8.29(b).

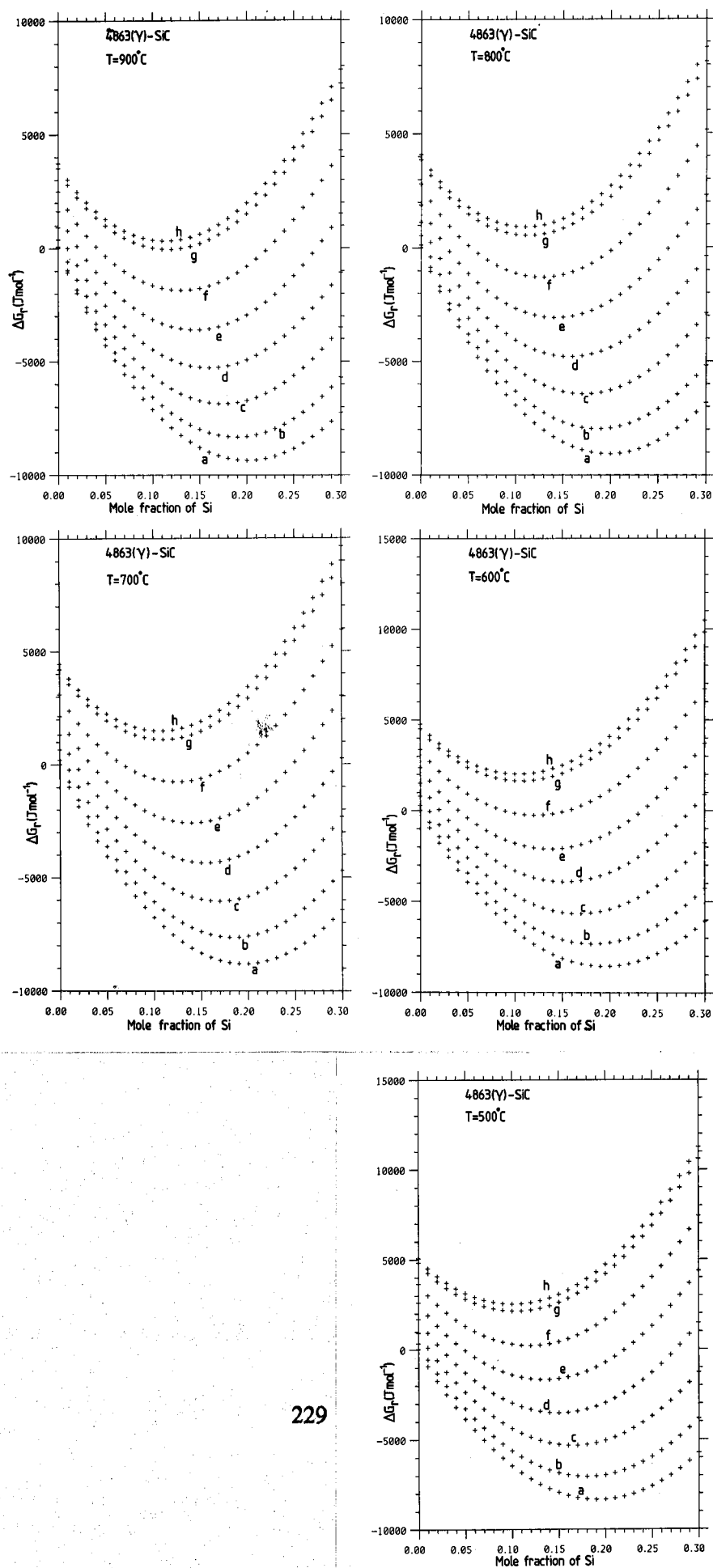


Figure 8.30.

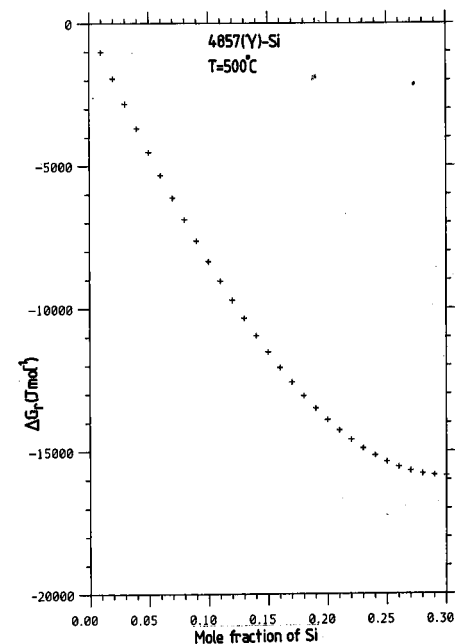
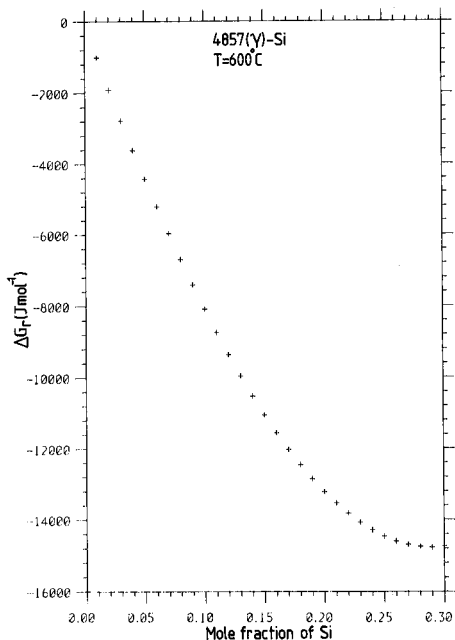
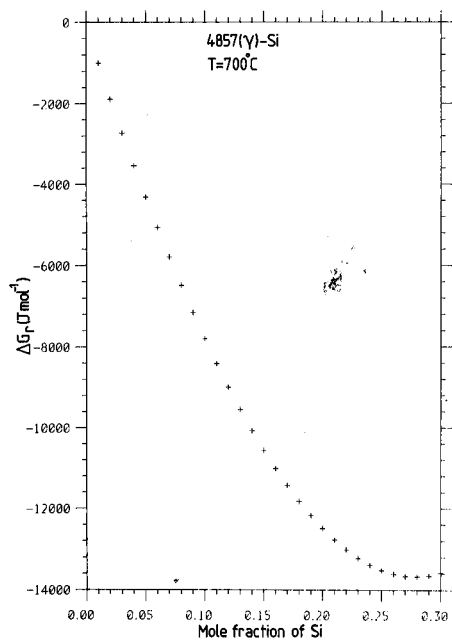
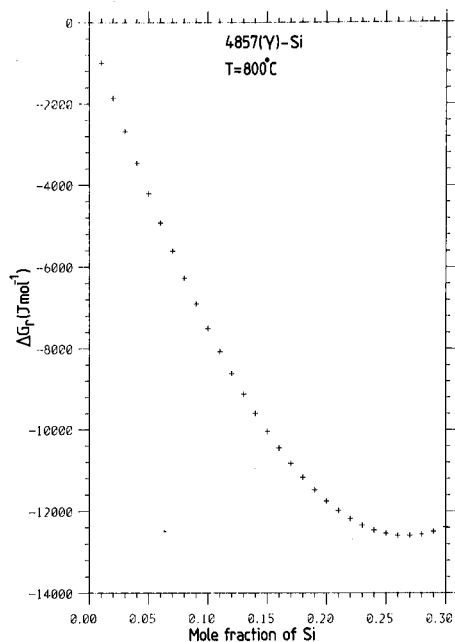
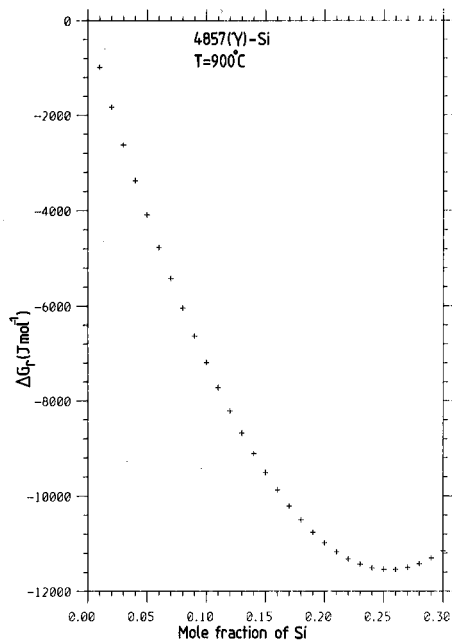


Figure 8.31(a).

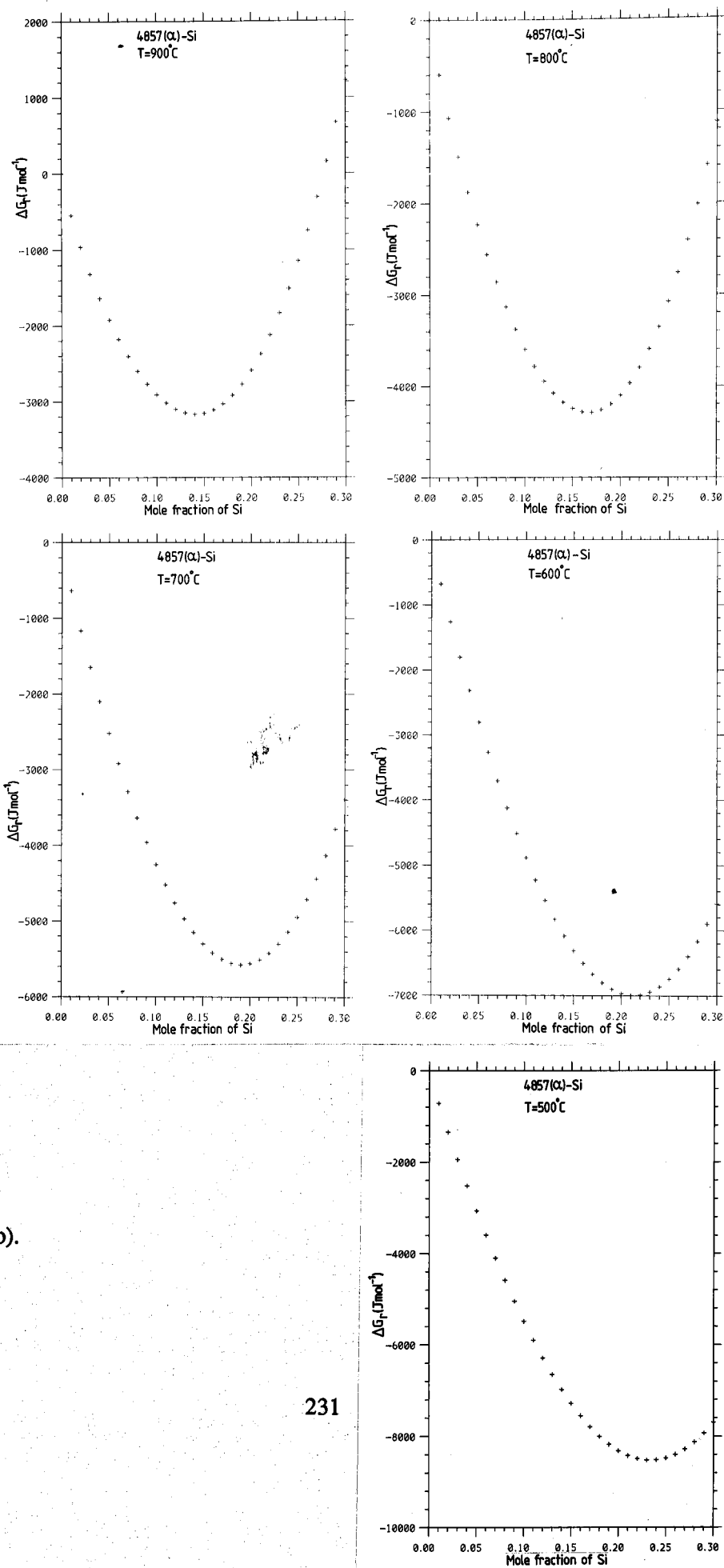


Figure 8.31(b).

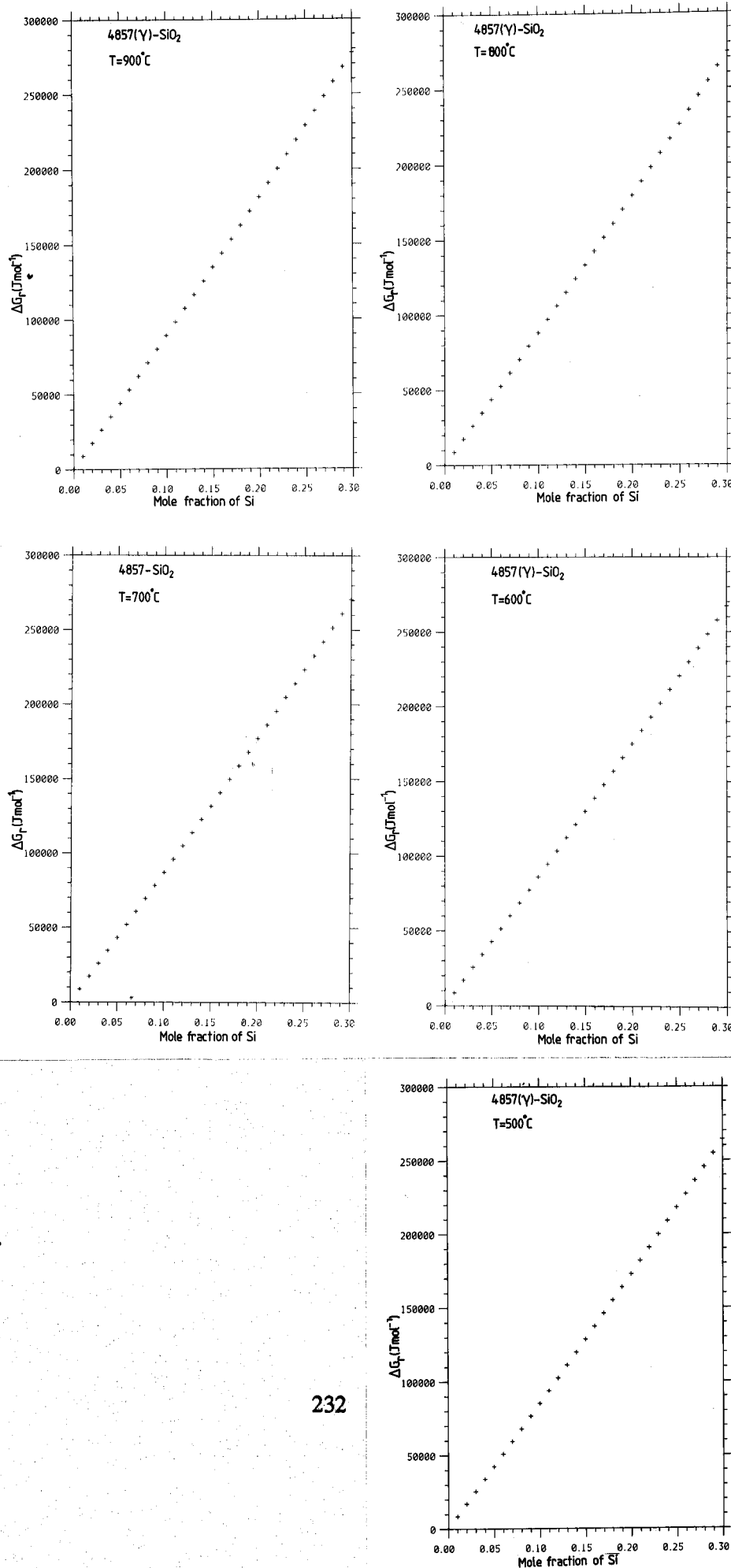


Figure 8.32.

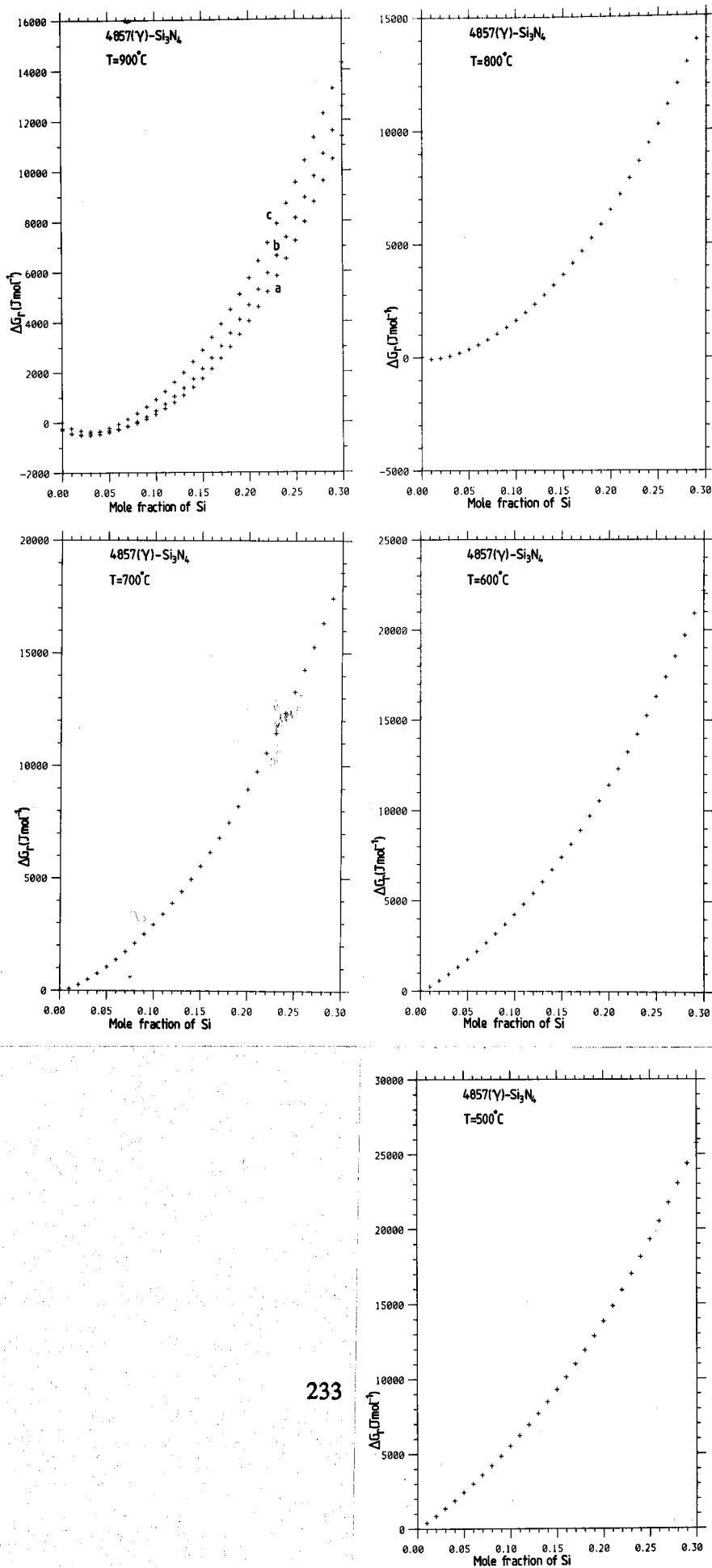


Figure 8.33.

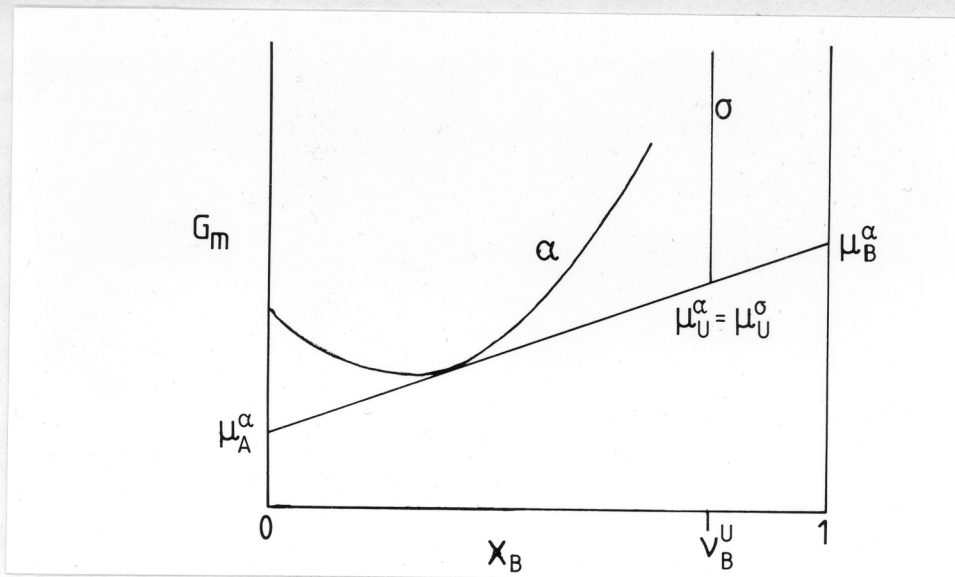


Figure 8.34. Equilibrium for a line compound.

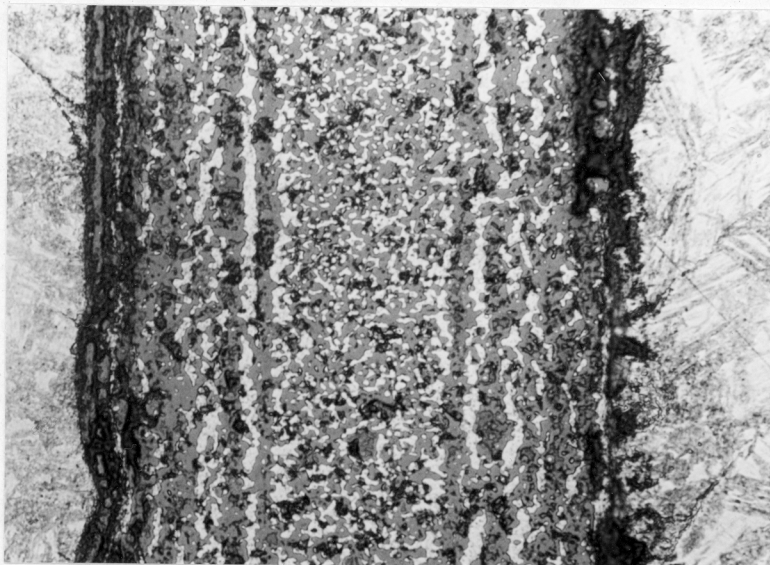


Figure 8.35. 20μm, 4857/CoO, 900°C/10mins-505°C/300s.

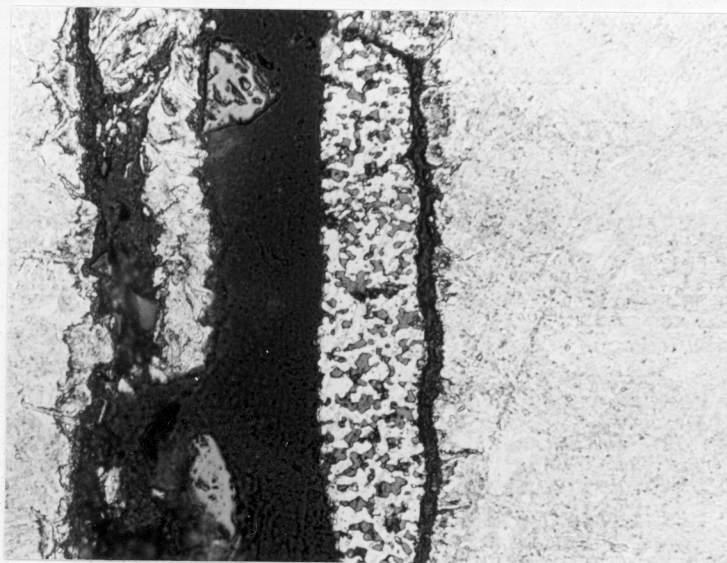
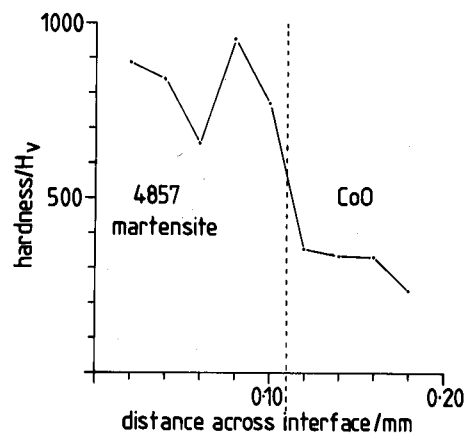
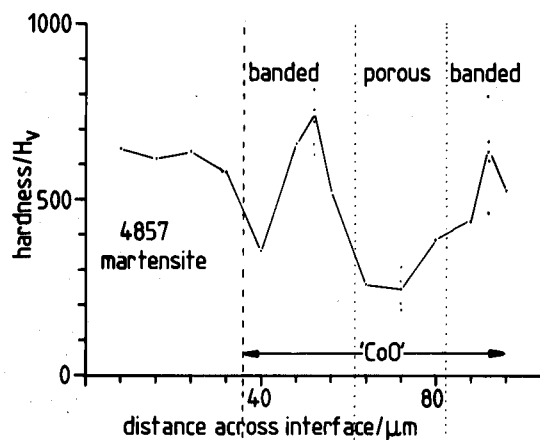


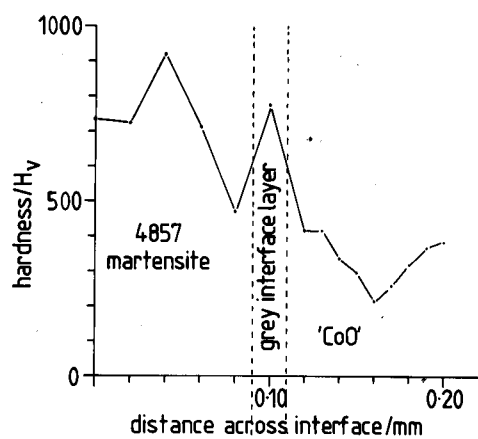
Figure 8.36. 25μm, 4857/CoO, 900°C/10mins-505°C/300s.



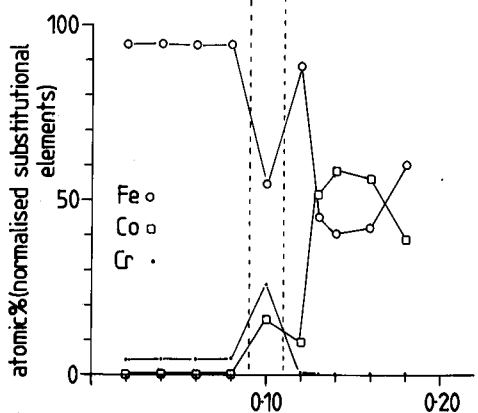
Continuously cooled from 900°C.

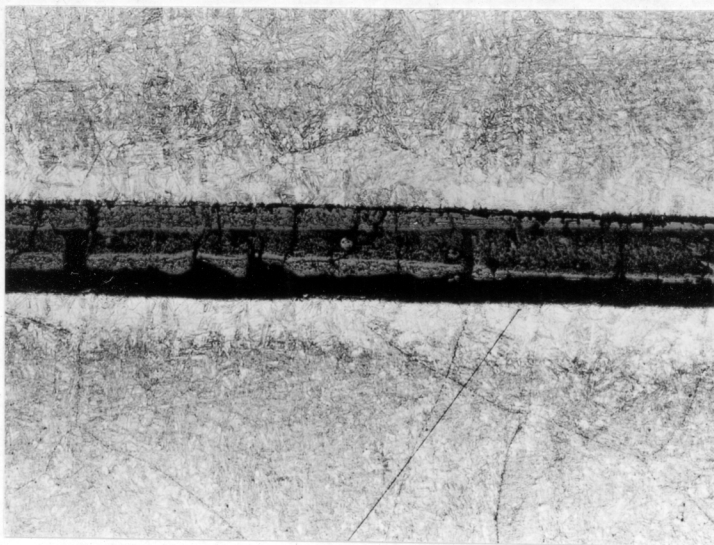
900°C/10 mins-505°C/300s.

Figure 8.37. Microhardness and microanalytical results for various heat treatments on 4857/CoO couples after re-austenitisation at 900°C for 10 minutes.



505°C/900s.






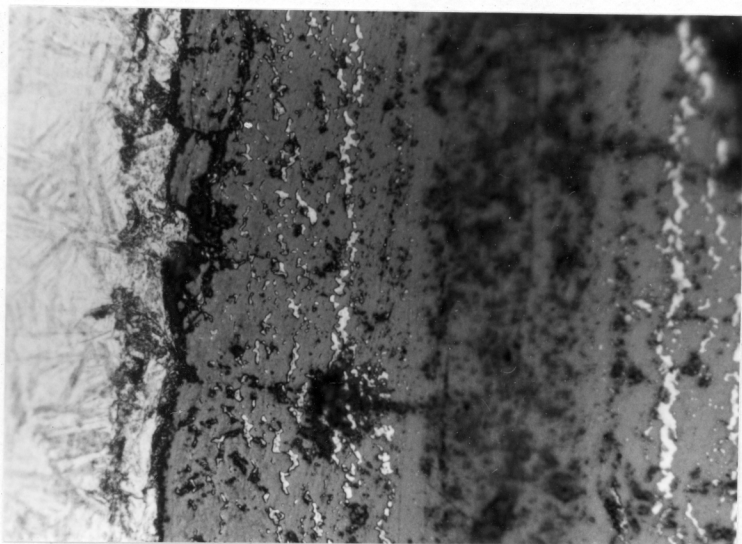
200 μ m 

Figure 8.38. Variation in steel microstructure away from interlayer.

Figure 8.39. Variation in CoO interlayer with heat treatment after reaustenitisation for 10 minutes at 900°C.

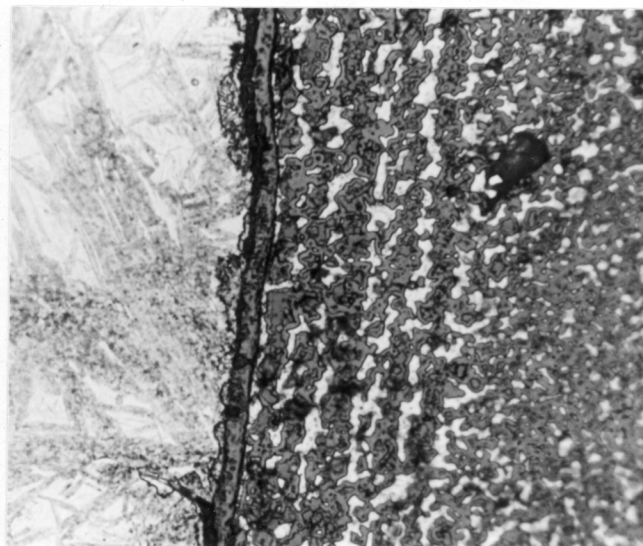


20 μ m 

(a) Continuously cooled

(c) 505°C/900s

15 μ m 



15 μ m 

(b) 505°C/300s

(d) 505°C/900s

7 μ m 

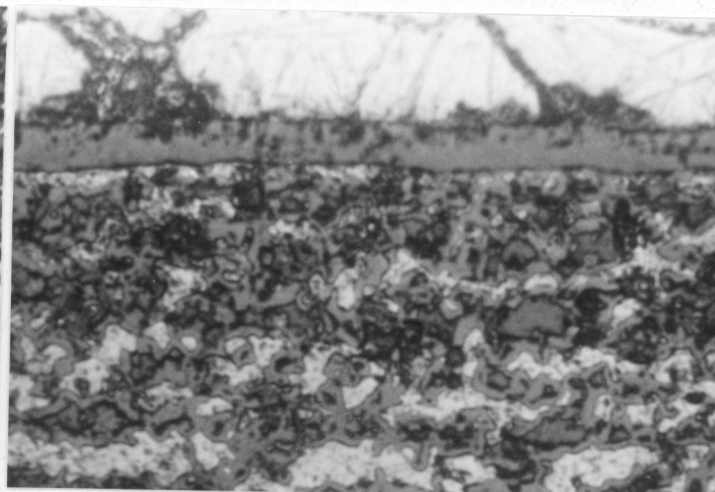
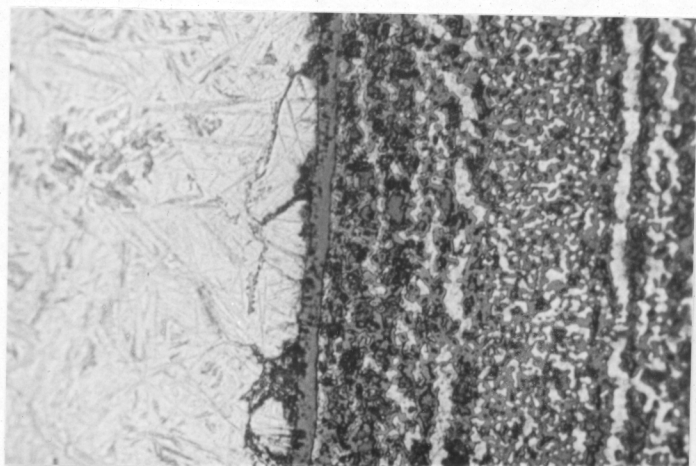
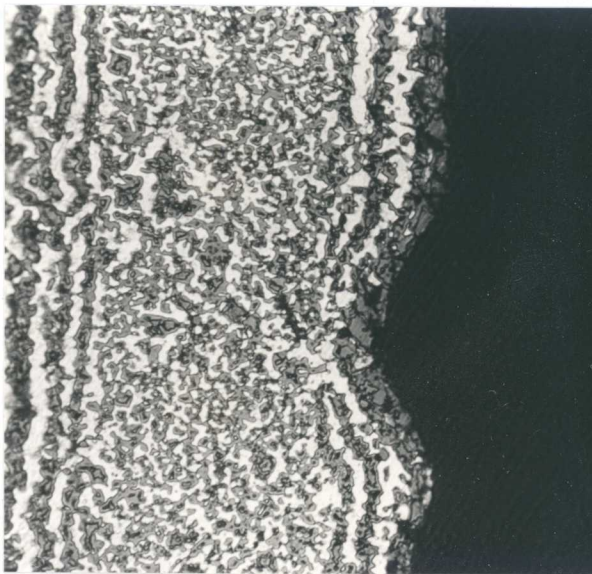


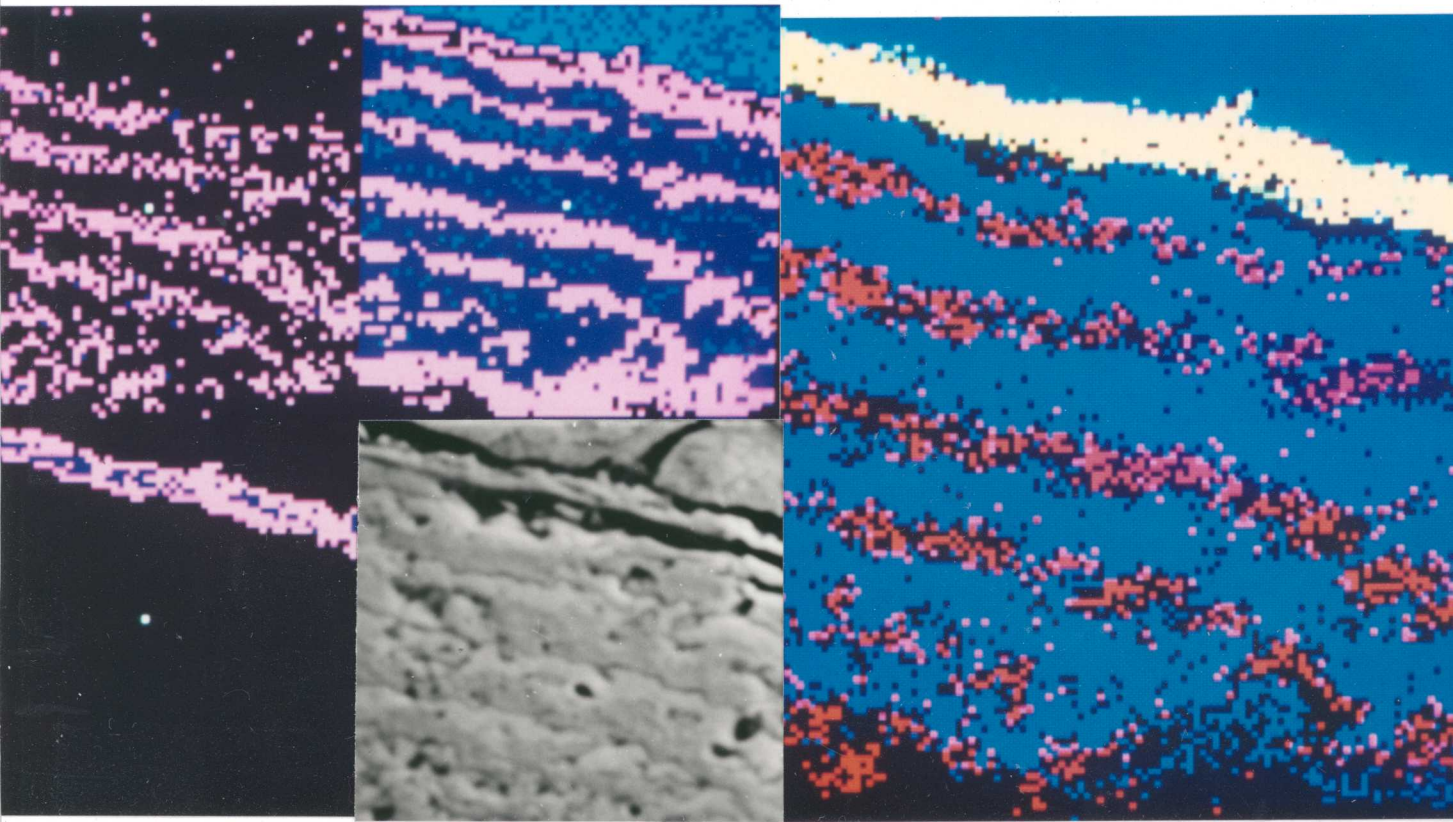
Figure 8.39 (contd).



20µm
(e) 505°C/45mins



20µm
(f) 450°C/300s



6µm
Figure 8.40. Digimap images $\frac{\text{Co}}{\text{Cr}} | \frac{\text{Fe}}{\text{Cr}}$

Figure 8.41. Multimapping of Fe (blue),
Co (red) and Cr (yellow).

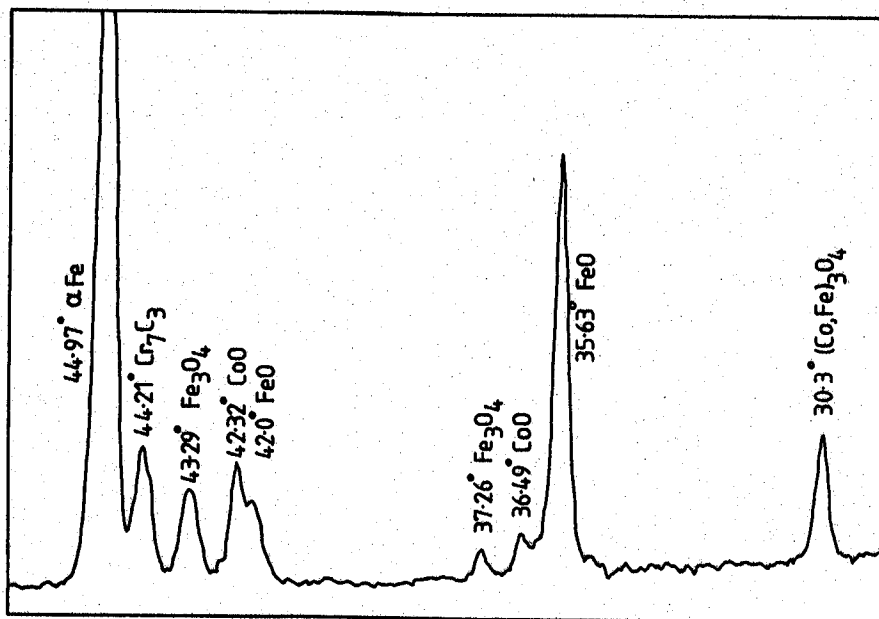


Figure 8.42. X-ray diffraction plot for 4857/CoO couple after heat treatment.

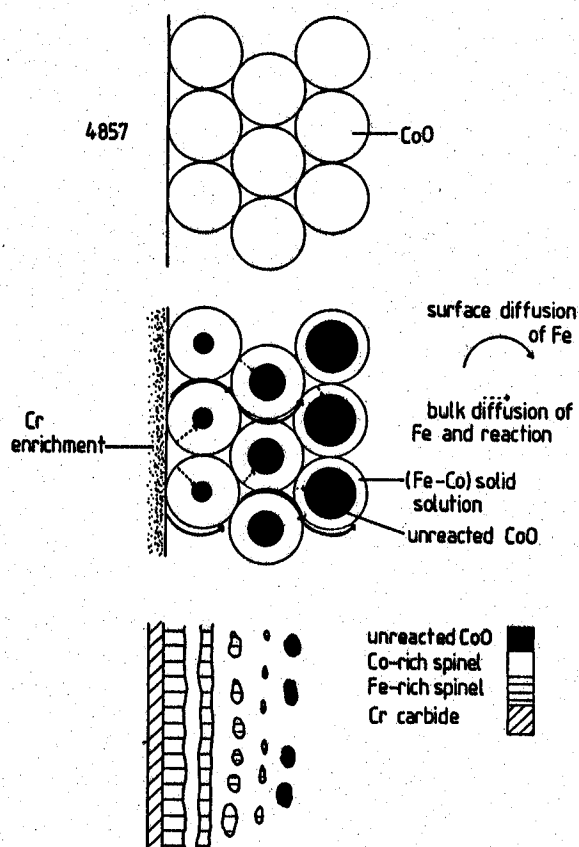
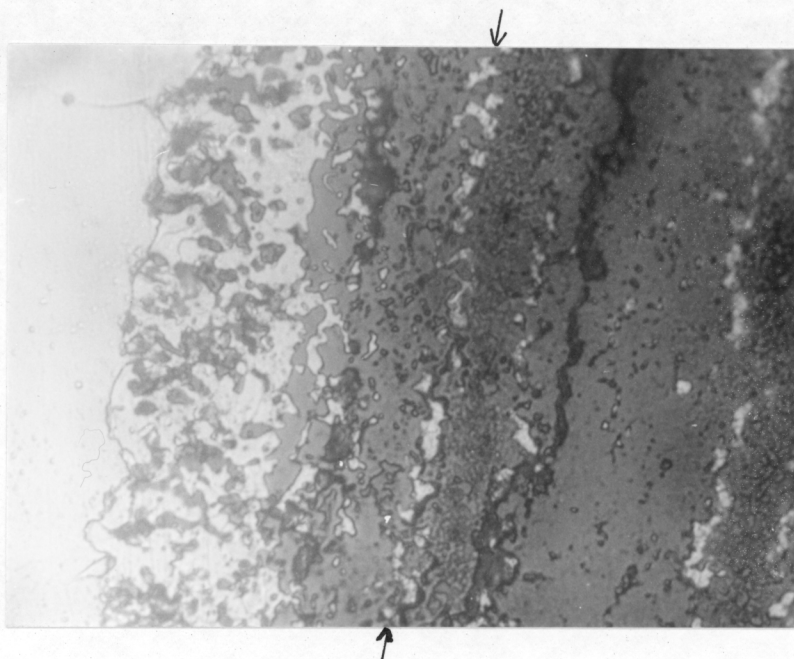


Figure 8.43. Proposed reaction process for 4857/CoO.



10 μ m

Figure 8.44. Interface for 4863/CoO. Original interface arrowed.